The Prototype Station for the IceCube Surface Array Enhancement

Zur Erlangung des akademischen Grades eines
Doktors der Naturwissenschaften
von der KIT-Fakultät für Physik
des Karlsruher Instituts für Technologie (KIT)

genehmigte
Dissertation

von Marie Johanna Oehler (M.Sc.)
aus Salem

Tag der mündlichen Prüfung: 22.10.2021
Referent: Prof. Dr. Ralph Engel
Korreferent: Prof. Dr. Marc Weber
Betreuer: Dr. Andreas Haungs

The prototype station for the IceCube Surface Array Enhancement

IceTop, the surface array of the IceCube Neutrino Observatory at the geographic South Pole, serves as both, a veto for the in-ice neutrino detection and a cosmic-ray detector. It consists of 162 ice-Cherenkov tanks, distributed over an area of $1\,\mathrm{km}^2$. Due to snow accumulation on top of the tanks, the resolution of IceTop decreases and the energy threshold increases.

The Surface Array Enhancement (SAE) will measure and mitigate the effects of the snow accumulation, enhance the veto capabilities and improve cosmic-ray measurements by increasing the detection sensitivity in the primary energy range of 100 TeV to 1 EeV. Additionally, it serves as R&D for the large-scale surface array of IceCube-Gen2, the planned next generation neutrino detector at the South Pole. 32 stations will be deployed within the current IceTop footprint. Each station comprises of eight elevated scintillation detectors with SiPM readout and three radio antennas, connected to a central DAQ.

In the frame of this thesis, the designs of two initial R&D stations have been merged and optimized for the SAE. A prototype station was built and deployed at the South Pole in January 2020. The characterization and calibration of the scintillation detectors show a high light yield for individual particles, which enables a low energy threshold. Temperature effects of the SiPM readout are evaluated and compensated in the data analysis.

First analyses of air-shower data of the prototype station are performed. A method to combine the data from the single detectors to air-shower events is established. The comparison of measured events with expectations from simulations shows agreement. Therefore, it can be concluded that the simulations are valid and that the scintillation detector effects are understood. For events, which are measured in coincidence with the scintillation detectors and IceTop, the comparison of the reconstruction results show that the angular resolution of a single station for events with coincident hits from eight scintillation detectors is competitive to the IceTop reconstruction. For triple coincidences, i. e. events measured in coincidence with the scintillation detectors, radio antennas and IceTop the reconstruction results of the zenith angle agree within 4°.

Based on these results, not only the design for the SAE is validated for the production of the 32 stations, but also several hints could be provided for improvements, in particular related to the firm- and software of the detector system. In addition, the design will be used as the baseline design for the future surface array of IceCube-Gen2. The experimental verification of the simulation confirms the simulation basis for IceCube-Gen2. These are important steps in the planning, optimization and realization of IceCube-Gen2.

DIE PROTOTYPSTATION FÜR DIE OBERFLÄCHEN-ERWEITERUNG VON ICECUBE

IceTop, das Oberflächenarray des IceCube Neutrino Observatoriums am geographischen Südpol, dient sowohl als Veto für die Neutrinodetektion im Eis als auch als Detektor der kosmischen Strahlung. Es besteht aus 162 Eis-Cherenkov-Tanks, die über eine Fläche von 1 km^2 installiert sind. Durch Schneeablagerungen auf den Tanks nimmt allerdings das Auflösungsvermögen des Arrays ab und die Energieschwelle zu.

Die Oberflächen-Erweiterung (SAE) wird die Effekte der Schneeablagerungen messen und korrigieren, das Vetovermögen erhöhen sowie die Luftschauermessungen verbessern durch die Erhöhung der Detektionssensitivität in dem Energiebereich der Primärteilchen zwischen 100 TeV und 1 EeV. Zusätzlich dient das SAE als F&E für das großskalige Oberflächenarray von IceCube-Gen2, dem geplanten Neutrinodetektor der nächsten Generation am Südpol. 32 Stationen werden innerhalb der IceTop-Grundfläche eingesetzt werden. Jede Station umfasst acht erhöht aufgebaute Szintillationsdetektoren und drei Radioantennen, die an eine zentrale Datenerfassung angeschlossen sind.

Im Rahmen dieser Arbeit wurden die Designs der beiden ursprünglichen F&E-Stationen für das SAE zusammengeführt und optimiert. Eine Prototypstation wurde gebaut und im Januar 2020 am Südpol aufgestellt. Die Charakterisierung und Kalibrierung der Szintillationsdetektoren zeigt eine hohe Lichtausbeute für individuelle Teilchen, wodurch eine niedrige Energieschwelle ermöglicht wird. Die Temperatureffekte des SiPM werden evaluiert und in der Datenanalyse kompensiert.

Erste Analysen der Luftschauerdaten der Prototypstation wurden durchgeführt. Eine Methode wurde erstellt, um die Daten der einzelnen Detektoren zu Luftschauerereignissen zusammen zu führen. Der Vergleich der gemessenen Daten mit den Erwartungen von Simulationen zeigt eine valide Übereinstimmung. Daraus kann geschlossen werden, dass die Simulationen gültig und dass die Effekte der Szinitillationsdetektoren verstanden sind. Für koinzidente Ereignisse von Szintillationsdetektoren und IceTop, zeigt der Vergleich der Rekonstruktionen, dass die Winkelauflösung einer einzelnen Station für Ereignisse mit acht koinzidenten Szintillatormessereignissen konkurrenzfähig ist zu der IceTop-Rekonstruktion. Für Tripelereignisse, d. h. koinzidente Ereignisse von Szintillationsdetektoren, Radioantennen und IceTop, stimmen die Rekonstruktionsergebnisse der Zenitwinkel innerhalb von 4° überein.

Durch die Ergebnisse dieser Arbeit wurde nicht nur das Design für das SAE validiert, wodurch die 32 Stationen gebaut werden können, sondern auch mehrere Hinweise für Verbesserungen, insbesondere in der Firm- und Software des Detektorsystems, gefunden. Zusätzlich wird das Design als Basis für das zukünftige Oberflächenarray von IceCube-Gen2 dienen. Die experimentelle Verifikation der Simulationen bestätigt die Simulationskette für IceCube-Gen2. Dies sind wichtige Schritte in der Planung, Optimierung und Realisierung von IceCube-Gen2.

Contents

---

1 INTRODUCTION 1

2 COSMIC RAYS AND AIR SHOWERS 3
  2.1 Cosmic rays 3
  2.2 Cosmic-ray air-showers 6
  2.3 Detection methods of cosmic-ray air-showers 9

3 ICECUBE NEUTRINO OBSERVATORY 13
  3.1 IceCube 13
  3.2 IceTop 16
  3.3 Surface Array Enhancement (SAE) 17
  3.4 IceCube Upgrade 19
  3.5 IceCube-Gen2 19

4 DETECTORS AND DAQ OF THE SAE PROTOTYPE 21
  4.1 Overview 21
  4.2 Scintillation detectors and Scintillator MicroDAQs v4.1 22
  4.3 Central DAQ 28
  4.4 Radio antennas 33
  4.5 Firm- and software 33

5 DEPLOYMENT OF THE SAE PROTOTYPE AT THE SOUTH POLE 37
  5.1 Tests before deployment 37
  5.2 Final layout of the deployed station 39
  5.3 Deployment of the central DAQ 39
  5.4 Deployment of the scintillation detectors 43
  5.5 Deployment of the radio antennas 45

6 COMMISSIONING 47
  6.1 Timing 47
  6.2 Scintillation detectors 47
    6.2.1 Communication 47
    6.2.2 Triggers 50
  6.3 Radio antennas 51

7 CHARACTERIZATION OF THE SCINTILLATION DETECTORS AND RADIO ANTENNAS 53
  7.1 Characterization of the scintillation detectors 53
    7.1.1 Characterization of settings of the Scintillator MicroDAQs 53
    7.1.2 Threshold scan of the scintillation detectors 56

        - 7.1.3 Influence of sunlight on the baseline during the austral summer 57
        - 7.1.4 Baseline stability during the austral winter 66
        - 7.1.5 Timing of the scintillation detectors 66
        - 7.1.6 Determination of the dead time 69
        - 7.1.7 Gain and MIP light yield from charge histograms 71
        - 7.1.8 Temperature compensation 76
        - 7.1.9 Saturation 76
    - 7.2 Radio electronics 79

- 8 RESULTS OF FIRST AIR-SHOWER DATA ANALYSIS 81
    - 8.1 Event rate as a function of multiplicity 82
    - 8.2 Environmental effects on the single detector hit rate 83
    - 8.3 Timing difference between scintillation detectors, IceTop and radio antennas 84
    - 8.4 Comparison with simulations 86
    - 8.5 Reconstruction of air showers 91
        - 8.5.1 Reconstruction of scintillator hitbuffer data 91
        - 8.5.2 Comparison of the reconstruction results of scintillators and IceTop 94
    - 8.6 Triple Coincidences 95

- 9 SUMMARY AND OUTLOOK 99

- APPENDIX 101
    - A Supplementary material about MicroDAQ 101
    - B Grounding of the SAE prototype 104
    - C Direction of the sunlight for peaks in baseline 105
    - D Cable delays of the SAE prototype 106
    - E Environmental effects on the single panel hit rate 107
    - F Distribution of the simulated air-showers 109
    - G Difference between the results of the scintillator reconstruction and Laputop 110
    - H Further photos of the deployment at South Pole 111

- ACRONYMS 112

- LIST OF FIGURES 115

- BIBLIOGRAPHY 119

1

Introduction

Cosmic rays are highly energetic charged particles hitting the Earth's atmosphere. They originate from galactic and extragalactic sources. The energy of cosmic rays covers many orders of magnitude, reaching energies of 10^{20} eV and above [GER16; BEH09; Gri10]. When a high-energy cosmic ray collides with an molecule in the atmosphere, new hadronic, muonic and electromagnetic particles are created which in turn interact with the atmosphere, creating an avalanche effect. These particles can be measured on Earth using air-shower experiments. Since the cosmic-ray flux decreases with energy, large detector arrays are needed to measure the high-energy cosmic rays the with the best possible statistics. Even though cosmic rays are studied since the beginning of the 20th century, their sources as well as the acceleration mechanisms and propagation effects are not fully understood. To constrain the models, measurements with the highest possible accuracy are required. Also, by combining the information from several particle types, like cosmic rays, photons and neutrinos, in a multi-messenger approach, a more complete picture of the Universe can be obtained [GER16; Gri10; BEH09; HK10; Aab+16; Gru20].

The IceCube Neutrino Observatory helps to solve these open questions, measuring both, neutrinos and cosmic rays. IceCube is a $1\,\mathrm{km}^3$ sized Cherenkov detector located in the ice at depth between 1450 m and 2450 m at the geographic South Pole [Aar+17c]. IceTop, the surface component consisting of 162 ice Cherenkov tanks, is used as a veto against atmospheric muons and as a $1\,\mathrm{km}^2$ air-shower detector. Due to snow accumulation on top of the IceTop tanks, IceTop's resolution decreases and the cosmic-ray energy threshold increases [Abb+13; Raw16].

To mitigate the effect of the snow a Surface Array Enhancement (SAE) is planned, within the IceTop footprint. Additionally, the SAE will lower the energy threshold and improve cosmic-ray measurements. It is also used as R&D for the surface array of the future IceCube-Gen2. The array will consist of 32 hybrid stations. Each station comprises eight scintillation detectors and three radio antennas, which are connected to a central data acquisition system (DAQ). Previously, two scintillator prototype stations have been deployed at the South Pole, one of which was upgraded with two radio antennas a year later. [Hub+17; Ice19c; IR19; Ice19a; Ice21c; Ice21d].

In this thesis, the designs of these previous prototype stations have been merged, combining the advantages of both systems. The capabilities of the new design are examined and the performance is compared to the requirement for the SAE. This shows whether it can be used for SAE and as a baseline design for future IceCube-Gen2 developments. First, an introduction into the physics of cosmic rays and air showers is given in chapter 2 and the IceCube Neutrino Observatory as well as the future plans are presented in chapter 3. The design of the station and the built hardware is described in chapter 4. The deployment of the station at the South Pole and the commissioning are can be found in chapters 5 and 6, respectively. The characterization and calibration of the scintillation detectors is presented in chapter 7. In chapter 8, the analysis of the first air-shower data is presented. The simulations of the scintillation detectors are validated by comparison with measured data and the first reconstruction of air-shower data is performed to benchmark the performance of the station.

2

COSMIC RAYS AND AIR SHOWERS

Cosmic rays are charged particles from space. Upon colliding with Earth's atmosphere, they create cascades, whose particles can be measured on earth by air-shower experiments [GER16; Gru20].

The study of cosmic rays is at the intersection of astrophysics, particle physics, astronomy and cosmology. Before human-built particle accelerators were available, these studies led, among others, to the discovery of the first known antiparticle and of muons [And33; SS37]. Cosmic rays with energies above 10^{20} eV have been observed, reaching energies not achieved by human-built accelerators. The study of particles at these highest energies is not only of interest for research on predictions of the Standard Model, but also when trying to understand the processes in the Universe shortly after the Big Bang [GER16; Gru20; HK10; Gri10].

Today, one of the main goals to study cosmic rays is to obtain astrophysical information. The particles are samples of matter outside our Solar System. The sources of cosmic rays are not understood well and the sources of the most energetic naturally occurring particles are unknown. Since multiple particles of different types are created in collisions close to the sources, the properties of these sources can be further investigated by combining the data from measurements of disparate particle types, making cosmic-rays part of multi-messenger astronomy [Gru20; GER16; SSB18].

In this chapter, first a summary of the knowledge of cosmic rays is given in section 2.1. Afterwards, in sections 2.2 and 2.3, air-showers and methods of their detection are explained.

2.1 Cosmic rays

Cosmic rays are mainly fully ionized atomic nuclei of cosmic origin. The energy of cosmic rays covers several orders of magnitude, from a few GeV to 10^{20} eV. While the cosmic-ray flux is $\approx 10\,\text{particles}/\text{m}^2/\text{ms}$ at low energies, it decreases to less than $1\,\text{particle}/\text{km}^2/\text{century}$ for high energies. The composition of cosmic rays is in a large energy range approximately as in the Solar System, differences can be explained by propagation effects. Most particles hitting Earth are protons and only a few particles have a higher atomic number than iron [Gru20; GER16; BEH09].

The current interpretation for energies up to PeV is that supernova remnants accelerate the particles. The accelerated protons interact with interstellar matter, producing neutral pions, which decay to high-energy gamma, indicating hadronic

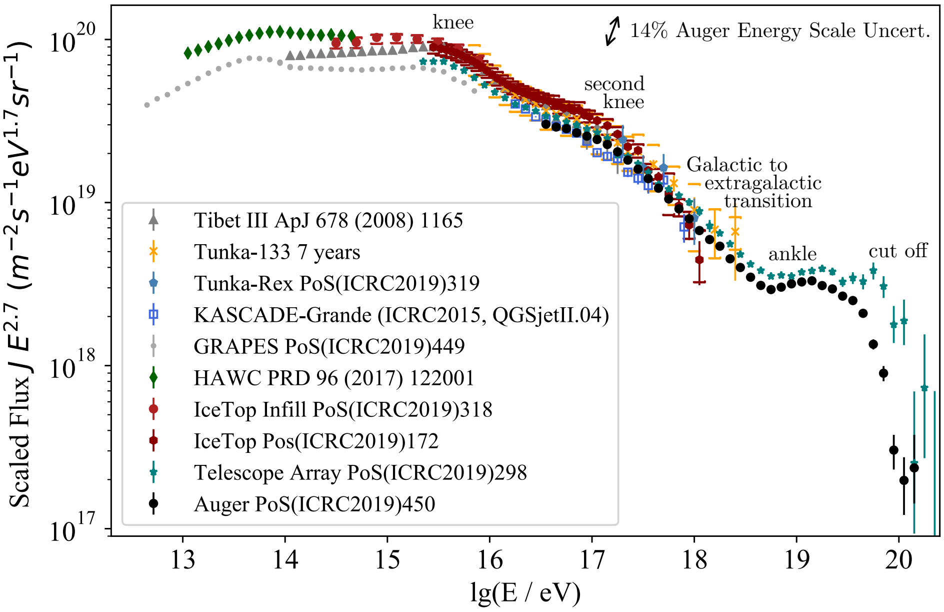

Figure 2.1: Energy spectrum of cosmic rays from ground-based measurements. The flux is scaled by a factor of $E^{2.7}$, so the marked spectral features are more visible. As an example, the effect on the spectrum by the uncertainty on the absolute energy scale of the Pierre Auger Observatory is indicated. Picture modified from [Sch19a].

processes in the source. Thus, the detection of high-energy gammas of a source is an indication that the source can accelerate cosmic rays. The Fermi Large Area Telescope detected such high-energy gammas from supernova remnants and there is evidence that supernova remnants are cosmic-ray sources. For the highest energies, the sources are still unknown [Ack+13; Gru20; Gri10; GER16].

Cosmic rays can be detected directly and indirectly [GER16]. In direct detection, the cosmic rays interact with the detector in a balloon or in Earth's orbit. Direct detection provides an accurate measurement of the energy and mass of the cosmic ray. However, due to the small aperture of the detectors and the decreasing cosmic-ray flux, direct detection is limited to the TeV range [Spa19]. For the measurement of higher energy cosmic rays, indirect detection via extensive air-showers is used. When a cosmic ray interacts with the Earth's atmosphere, secondary particles are produced in atmospheric cascades, which can be observed with detectors on the ground [KU12; GER16; Gru20; Gri10]. Details on this are given in the section 2.2 and 2.3.

The energy spectrum of cosmic rays is shown in figure 2.1. The shape of the energy spectrum can be described by a power law,

$$\frac{\mathrm{d}N}{\mathrm{d}E} \propto E^{-\gamma}. \tag{2.1}$$

with changes in γ due to the maximum energy of acceleration mechanisms, rigidity dependent propagation effects and/or changes in the source population [Tho+16]. These changes are visible features in the spectrum, called knee, second knee, ankle and cutoff. γ is ≈ 2.7 up to 3×10^{15} eV, above which a steepening of the spectrum is visible to $\gamma \approx 3.1$. This break in the spectral index is called the knee and a decrease of the contribution from the light elements is observed [Ant+05; GER16; Hau15]. A smooth feature is visible at 100 PeV to 200 PeV, called the second knee [Sch19a]. Here, a decrease of the heavy elements is measured and above the second knee, γ changes to ≈ 3.2. The interpretation of these measurements is that galactic cosmic accelerators like supernova remnants reach their maximum energy, with the maximum energy depending on the magnetic rigidity

$$R_c = \frac{pc}{Ze} \approx \frac{E}{Ze}. \tag{2.2}$$

This means that the spectrum for protons steepens at $E = R_c e$, for helium at $E = 2R_c e$ etc., leading to mass-dependent positions of spectral breaks. With this interpretation, the knees are the first observation of the Peters cycle [GER16; Dem+17; Pet61]. The next feature of the cosmic-ray energy spectrum is the ankle at $\approx 3 \times 10^{18}$ eV. Between the second knee and the ankle, most probably a transition between galactic and extragalactic sources takes place [Sch19a]. At the ankle, the cosmic-ray flux is proton dominated. The dominant process for protons to loose energy is electron-positron pair production on the cosmic microwave background (CMB), which leads to a pileup effect [BGG06]. Above the ankle, γ flattens to ≈ 2.6, due to cosmic rays from extragalactic sources [GER16]. Above 10^{19} eV, cosmic rays are no longer confined in our galaxy, which indicates their extragalactic origin, but they originate from our "cosmic neighborhood", with a maximum distance of $\approx$ 100 Mpc. The reasons for this is the interaction of protons and nuclei with the CMB, during which they loose energy. Additionally photo-disintegration of nuclei takes place. Above 4×10^{19} eV, a strong suppression of the cosmic-ray flux is visible. This suppression could be due to photo-disintegration of nuclei via the delta resonance with the CMB and photo-pion production of protons with the CMB. An alternative theory is that the maximum acceleration energy of the extragalactic sources is reached [Gri10; GER16; Gru20].

From the energy spectrum, constraints can be obtained about the sources of cosmic rays. Since cosmic rays are charged, they are deflected in magnetic fields, so they do not point back to their source. Only for the highest energies and low charge, the rigidity is so high that they start pointing back to the sources. But these highest-energy cosmic rays lose their energy fast, as described before, and no individual sources have been observed for these energies so far. In a first order approximation, the maximum energy is defined by the radius of the acceleration region and the magnetic field of the source and the charge of the particle. Thus, one attempt to find possible source types is to classify astrophysical objects by their size and magnetic field strength, referred to as Hillas plot [Gru20; Gri10; Hil84].

The composition of the differential cosmic-ray flux is shown in 2.2. In this data-driven approach, the position of the flux is estimated on a large data set by evaluating a global spline fit. Estimations of element groups for the whole energy range are given.

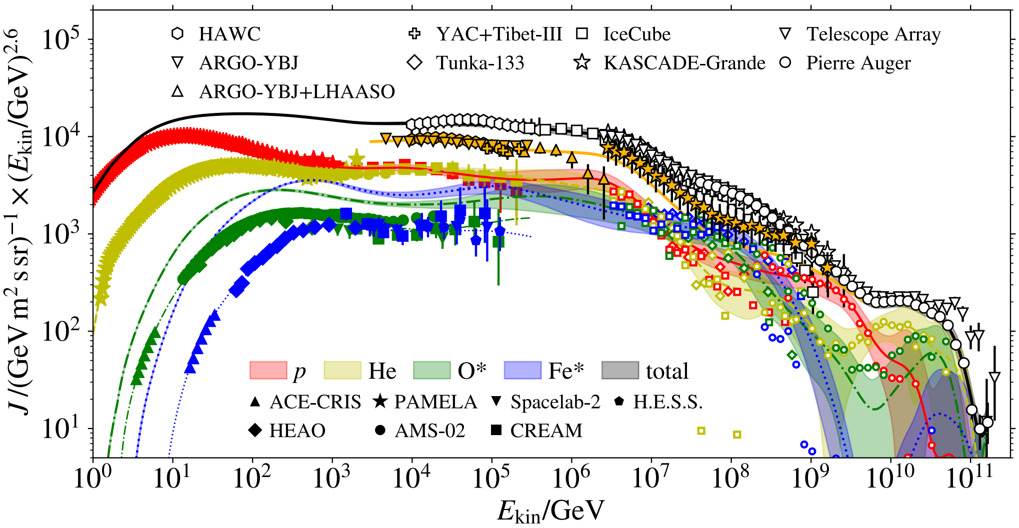

Figure 2.2: Composition of the all particle flux. The all-particle flux is shown in as the black solid line. The contributions of different primary masses, sorted into groups, are shown in the respective colors. The data points are scaled in energy, to combine all measurements [Sch19a].

This approach provides the most accurate estimation of the cosmic-ray flux at the moment and no theoretical assumptions are made [Dem+17]. From the composition, information about the sources, acceleration and propagation effects are gained [KU12].

2.2 Cosmic-ray air-showers

An extensive air shower is started most frequently, when a primary cosmic ray interacts hadronically with a nitrogen or oxygen molecule in the high atmosphere, producing pions and other hadrons. Repeatedly, the particles propagate and succeeding interactions create more particles, creating an avalanche effect [Gri10; Gru20; GER16].

The air showers have four components: the hadronic, electromagnetic, muonic and neutrino component, see figure 2.3. The high-energy hadronic particles are mainly in the core of the air shower, feeding the other components. Neutral and charged pions are created in the core. The neutral pions decay almost instantly to two photons with a mean lifetime of $\tau = 8.5 \times 10^{-17}$ s [Par+20]. These photons initiate electromagnetic subshowers with electron-positron pair production, bremsstrahlung and ionization in the atmosphere. The model of the development of electromagnetic showers follows later. A charged pion can either interact with molecules in the atmosphere, feeding the hadronic component or, with higher probability for lower energy, the charged pion decays to a muon and neutrino, contributing to the muonic component. The muons have a low energy loss and interact rarely. Thus, they travel long distances and can reach deep into the ground. The neutrinos produced in the air shower can have a high

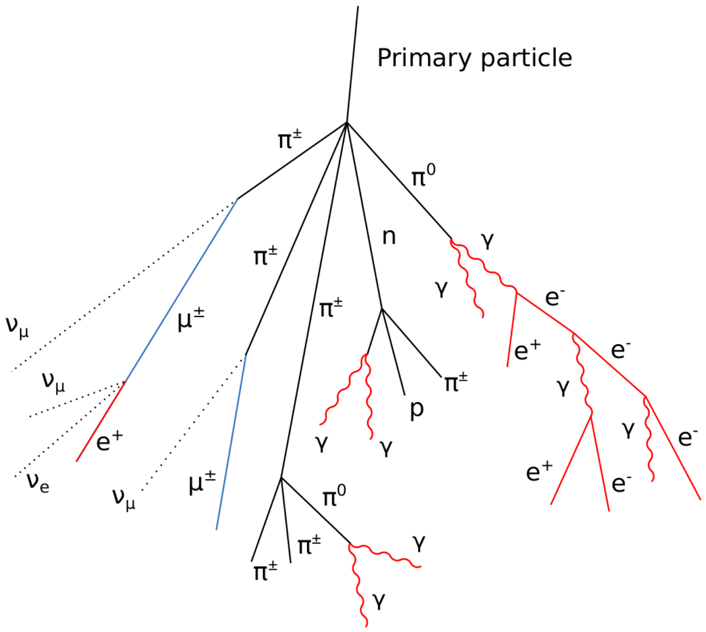

Figure 2.3: Schematic of the components of an air shower. The cosmic ray interacts with an air molecule, initializing a cascade with hadronic (black), muonic (blue), electromagnetic (red) and neutrino components (dotted lines) [Les21].

energy and carry a significant fraction of the energy of the air shower. The particle cascades continue, until the energy cannot sustain further production. This leads to the maximum development at the atmospheric depth $X_{\max}$, before the cascades die out. The electromagnetic component of the air shower decreases after $X_{\max}$, while the muonic component stops production, but travels further [Gri10; Gru20; GER16].

The development of electromagnetic showers is described by the Heitler model [Hei44]. When an electromagnetic particle with energy E_0 interacts after a mean free path λ, two secondary particles are produced, each with energy $E_0/2$. Hence, after n interactions, the particles posses the energy $E_0/2^n$, with $n = X/\lambda$ with atmospheric depth X. The process stops, when the energy of the particles cannot sustain further production. It can be concluded that the higher the initial energy E_0, the larger $X_{\max}$ and thus that the initial energy can be derived from $X_{\max}$ [KU12; Gri10; GER16].

The model was extended to hadronic interactions [Mat05]. At each interaction approximately ten pions are created, $2/3$ of which are charged and $1/3$ neutral. The energy at each interaction is distributed accordingly $E_0/3$ to the neutral pions and $2E_0/3$ to charged pions. The neutral pions decay quickly to electromagnetic subshowers and thus contribute to the electromagentic component and therefore to $X_{\max}$. The charged pions travel the distance λ and interact, producing new pions, until the energy is so low that it is more likely that the charged pions decay to muons, feeding the muonic component. In this model superposition is assumed: A primary cosmic ray consisting of a nucleus with A nucleons and the energy E_0, is taken as A individual nucleons, each

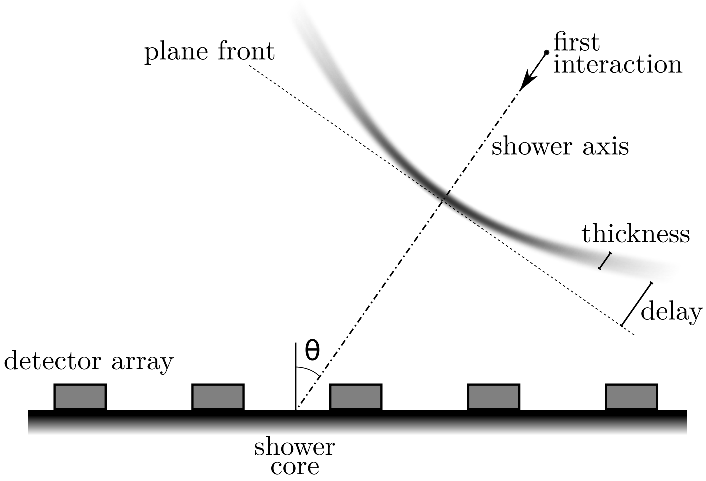

Figure 2.4: Schematic of an air shower with its basic parameters for description and reconstruction After the first interaction, the air shower follows the incident direction of the cosmic ray. As a first step, the curved disk of the air shower can be approximated by a plane front moving at the speed of light. The point, where the shower axis hits the ground, is the shower core position. Picture inspired by [Les21; GER16].

with the energy E_0/A, interacting independently. From this, it can be concluded that heavier primaries have more muons compared to a proton-induced air shower of the same energy $N_\mu^A = N_\mu^{\text{proton}} A^{0.15}$ and a lower $X_{\text{max}}^A = X_{\text{max}}^{\text{proton}} - \lambda \ln(A)$. In general, hadronic cascades have a lot of complex interactions. Many interactions happen at higher energies and in more forward direction than can currently be measured by particle accelerators, so the hadronic models have to be extrapolated. This makes them the one of the main uncertainties in high-energy comic-ray measurements [EHP11; KU12; Lip14].

To reconstruct cosmic-ray air-showers, as is described in chapter 8, their basic properties need to be known. The main air-shower properties are illustrated in figure 2.4. A primary cosmic ray interacts in the atmosphere. The direction of the primary particle is given in zenith and azimuth angles, like in a spherical coordinate system. The resulting atmospheric cascade propagates longitudinally along the primary direction. The impact point at ground is called shower core. It is the most dense region and a large fraction of the cascade is measured within a few nanoseconds close to the core. The lateral development of the air shower results from the traverse momentum from hadronic interaction to individual secondary particles and from Coulomb scattering of the electromagnetic component, resulting in big distances of particles to the shower core. The spread is the thickness of the shower front and the disk spread increases, when particles move away from the axis. The shower disk is curved, so particles at the edges of the disk are delayed by up to a few hundred nanoseconds compared to close the shower axis. However, especially for small detector arrays, a plane front approximation can be done. The lateral distribution function (LDF) describes the lateral particle density or signal distribution S as a function of distance perpendicular to the shower axis. It is one of the main tools to get information about the primary cosmic ray. Following the work of [Les21], in this work the double logarithmic parabola is used as LDF,

$$S_{\mathrm{DLP}}(r) = S_{\mathrm{ref}} \left(\frac{r}{R_{\mathrm{ref}}} \right)^{-\beta - \kappa \log\left(\frac{r}{R_{\mathrm{ref}}} \right)}, \tag{2.3}$$

with the distance to the axis r, the reference distance R_{ref} and the slope β. The spatial and temporal development of the air shower varies with the energy, direction and mass of the primary cosmic ray, leading to a different distribution measured at the ground [Gri10; GER16].

To measure cosmic-ray air-showers, the secondary particles and the radiation of the air shower are measured on the ground. The size of the air-shower footprint determines the scale of the instrumented area. To detect an air shower, one searches for time coincident signals of neighboring detectors. From the time delay of the shower front reaching the detectors, the arrival direction is determined. The shower core position is obtained by fitting the LDF and the energy of the primary cosmic ray from the size of the detector signals. However, there are large fluctuations due to different primary masses and from fluctuations in the shower development [GER16; Gri10].

2.3 Detection methods of cosmic-ray air-showers

The detection and measurement of cosmic-ray air-showers is possible via several channels: The fluorescence emission from excited nitrogen particles, the measurement of radio emission from the air-shower and the measurement of the energy deposit of particles at the surface, see figure 2.5. A description of the most deployed detector types follows.

Fluorescence telescopes When an air-shower propagates in Earth's atmosphere, nitrogen molecules are excited. The excitation energy is released by emission of fluorescence light, which is detected by fluorescence telescopes. This technique provides the most precise measurement of the longitudinal profile and thus X_{max}. The disadvantages are the necessity to understand the atmospheric profile and the low uptime, since the measurements are only possible in dark, moonless nights [GER16; Gri10].

Cherenkov detectors When relativistic particles pass through an optically transparent dielectric medium, like water or ice, with a speed faster than the speed of light in this medium, Cherenkov radiation is emitted and can be detected. When instrumenting large detector volumes, they can be used as telescopes. This method is very reliable and has a high uptime. An example of such a telescope is given in chapter 3.

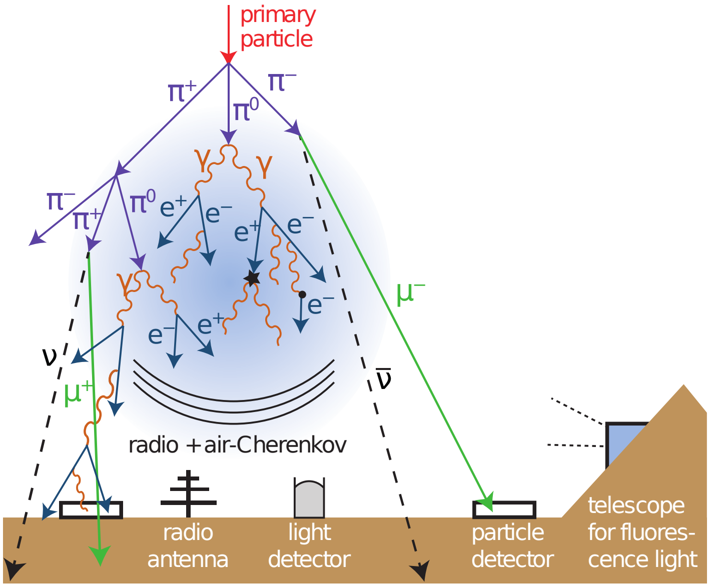

Figure 2.5: Air-shower detection techniques The cosmic ray interacts with an air molecule, initializing an air-shower with hadronic (purple), muonic (green), electromagnetic (orange/blue) and neutrino (black dashed) components. Particle detectors measure mainly the electromagnetic and muonic component. Radio antennas, air-Cherenkov and fluorescence telescopes are only sensitive to the electromagnetic component [Sch17].

Air-Cherenkov detectors The charged particles in an air-shower can have such high kinetic energy that Cherenkov radiation is produced. Since this method is sensitive to the electromagnetic component of the air-shower, a good determination of the primary energy is possible. Air-Cherenkov detectors have a low energy threshold on the order of 30 GeV. When using more than one telescope, the shape of the air-shower can be obtained and thus a photon-induced air-shower can be distinguished from hadronic showers. The limitation of the measurement time to clear, moonless nights results in a low uptime and it is necessary to have a good atmospheric density profile [GER16; Gri10].

Radio antennas Air-showers emit radiation in the radio frequency range. The two main effects creating the radio emission are the geomagnetic effect and the Askaryan effect. In the dominant geomagnetic effect, the electrons and positrons are spatially separated in Earth's magnetic field by the Lorentz force, creating an electric field. The number of electrons and positrons grows until X_{max} and drops afterwards, thus creating time varying net currents, which leads to radio emission. In the Askaryan effect, the ionization of the atmosphere during the development of an air-shower results in electrons in the shower front, while the heavier ions are left behind. The number of charge carriers grows and drops with the shower development, creating time varying net currents. Most experiments use signals in the 30 MHz to 400 MHz band region, because this provides the best signal-to noise ratio. Radio antennas are only sensitive to the electromagnetic component of the air-shower. Because they provide a good estimation of X_{max}, the energy and the mass composition can be obtained, especially when combining with other detectors. Compared to other detectors, radio antennas are cheap and have a high uptime [KL66; Ask62; Sch17; Bal19].

Scintillation detectors The particle detectors are made of scintillation material. When particles pass through the material, ionization takes place and creates light with a respective light yield. This light is collected and measured. The detectors mainly measure the electromagnetic and muonic component of the air-shower, especially the minimum ionizing particles (MIP). The light intensity gives the deposited energy in the material and the time of the signal the time of arrival of the MIP. It is a reliable detection method and independent of external conditions. By using different detectors, each reacting differently to the components of the air-shower, a discrimination of the mass of the primary cosmic ray is possible [Gri10; Gru20]. The scintillation detectors used in this thesis are organic plastic scintillators. The energy from the traversing charged particles is absorbed, leading to excited states of scintillator molecules. When transitioning to the ground state, photons are emitted. The de-excitation can happen fast via a fluorescence channel or delayed by up to milliseconds from the de-excitation of longer-lived states. Due to a small overlap between the emission and absorption spectra of the scintillator, they partially absorb their own light. By doping the scintillator material, scintillator light production is improved and additionally the light is shifted to the visible light range, which enables longer propagation distances of the light and makes it easier to detect [Kno00].

3

ICECUBE NEUTRINO OBSERVATORY

The IceCube Neutrino Observatory, hereafter IceCube, is a 1 km^3 neutrino telescope at the geographic South Pole [Ahr+01]. Its primary goals are to detect astrophysical neutrinos of all flavors in the energy range of $\mathcal{O}(\text{TeV}) - \mathcal{O}(\text{PeV})$ and to detect neutrino sources at cosmological distances [Aar+17c]. Among others, IceCube also studies the properties of neutrinos and searches for the sources of cosmic rays [Ahr+03; HK10]. To detect neutrinos, IceCube uses the Cherenkov effect with the transparent Antarctic ice as Cherenkov medium [Ahr+01].

Among IceCube's achievements are the discovery of high-energy extraterrestrial neutrinos and the identification of a source of the cosmic neutrino flux [Ice13; Aar+18c]. On 22 September 2017, IceCube measured a neutrino with ≈ 290 TeV, pointing back at a blazar. Since neutrinos interact weakly and are not deflected by magnetic fields, they point back at their source [Des06]. The real-time alert following this neutrino measurement, triggered follow-up observations by Fermi, MAGIC and other telescopes. Using this multi-messenger data, it is evident that blazars are sources of the cosmic neutrino flux and are therefore a source of cosmic rays [Aar+18c; Aar+18d], even though constraints show that they only make up up to ≈ 27 % of the observed astrophysical neutrino flux [Kow15; Aar+17b].

3.1 IceCube

A schematic of IceCube is shown in figure 3.1. The upper ≈ 1.5 km of the ice are used as natural shielding against background, like atmospheric muons produced by cosmic rays. Below, in a depth between 1450 m and 2450 m, the ice is instrumented with 5160 Digital Optical Modules (DOM), 60 of which are attached to each string, melted into the ice [Aar+13a]. Each DOM consists of a photomultiplier tube (PMT) with a data acquisition system (DAQ) to detect the Cherenkov light emitted by the charged particles generated by neutrino interactions, digitization electronics, a control and trigger system and light emitting diodes (LED) for calibration [Ach+06; HK10]. The local clocks in the sensors are calibrated with nanosecond precision, which enables the successful reconstruction of neutrino events.

DeepCore is an infill array in the center of IceCube, deployed in the clearest ice below 2100 m. It has a higher module density and uses PMTs with a higher quantum efficiency. DeepCore is a low-energy neutrino detector and by using the rest of IceCube as a veto, a threshold of ≈ 10 GeV is achieved [Abb+12]. This enables the observation

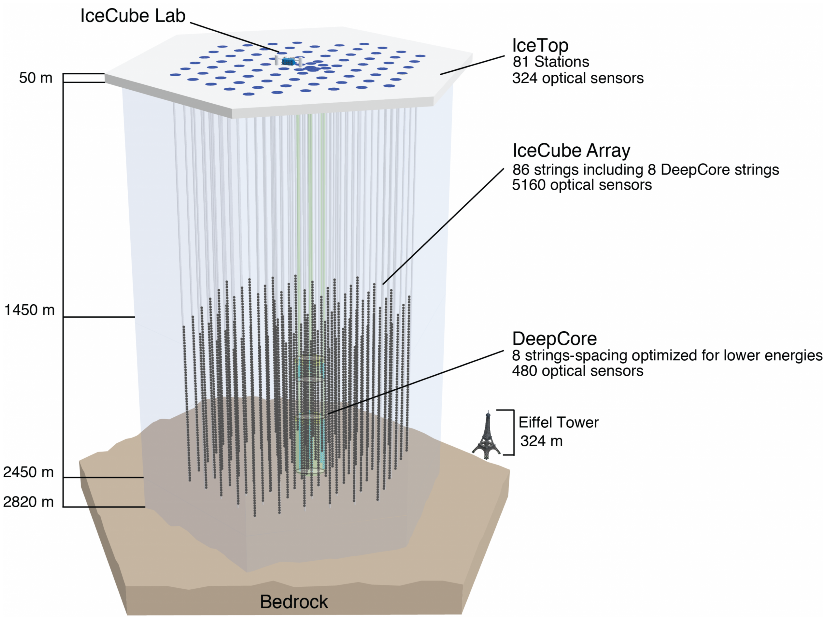

Figure 3.1: The IceCube Neutrino Observatory. The IceCube Neutrino Observatory uses ice-Cherenkov detectors to measure high-energetic neutrinos. Strings of Digital Optical Modules (DOM) are melted into the ice. On the surface two Cherenkov tanks at the top of each string form IceTop, which is used as an air-shower detector, a veto and for calibration [Ach+06]. Inside the IceCube Lab (ICL) is the server room with all data acquisition and online-filtering computers [Aar+17c]. Picture credit: IceCube collaboration.

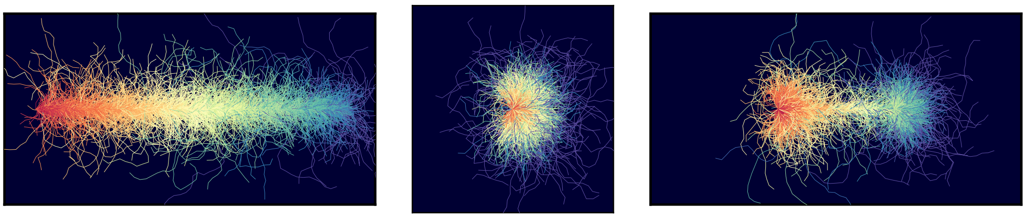

Figure 3.2: Shape of neutrino signals in the in-ice detector. The color indicates the arrival time, going from red first, to green last. The shape of the signal depends on the flavor of the neutrino. Muon neutrinos have track-like events (left), while electron neutrinos create "bangs" (middle), because the electrons interact strongly with the ice atoms and get reabsorbed. The decay of a tau neutrino results in the "double-bang" shape (right), one "bang" from the cascade of the target nucleus and the other from the decay of the tau [Aar+18b; HK10].

of GeV neutrino oscillations [Aar+18a].

The Cherenkov light used for the detection of the neutrinos is produced by particles, which are created by interactions of the neutrinos with the ice. When a neutrino interacts with a target nucleus in the ice via the charged current interaction, charged leptons are created. These are muons, electrons or taus, depending on the flavor of the neutrino.

$$\nu_\ell + \mathrm{N} \xrightarrow{\mathrm{W}^\pm} \ell + \mathrm{X}. \tag{3.1}$$

If the speed of the produced charged particle is higher than the phase velocity of light in the ice, i. e. faster than $\approx 75\,\%$ of the speed of light in vacuum, Cherenkov radiation in the blue, near UV-spectrum is emitted in a characteristic Cherenkov cone. Additionally, the neutrino transfers energy to the nucleus during the interaction, which creates a hadronic cascade. The secondary particles from this hadronic cascade also produce Cherenkov radiation. The Cherenkov light of both contributions is detected by the DOMs. The neutrinos can also interact via the neutral current interaction,

$$\nu_\ell + \mathrm{N} \xrightarrow{\mathrm{Z}^0} \nu_\ell + \mathrm{N}. \tag{3.2}$$

In this case, IceCube measures the hadronic cascade generated by the nucleus recoil [Aar+13a; HK10; AHH18]. From the pattern of the detected Cherenkov light, the direction of the neutrino, its energy and its flavor can be reconstructed [Ahr+01]. The direction is evaluated from the relative timing of when the DOMs detect Cherenkov light. The amount of detected light is proportional to the energy for contained events. The flavor of the neutrino is determined from the shape of the signal in the detector, see figure 3.2 [HK10; AHH18].

A recent result of IceCube is the detection of the Glashow resonance at 6.3 PeV. This detection indicates that electron antineutrinos are part of the astrophysical flux and confirms the prediction of the standard model of particle physics. The Glashow

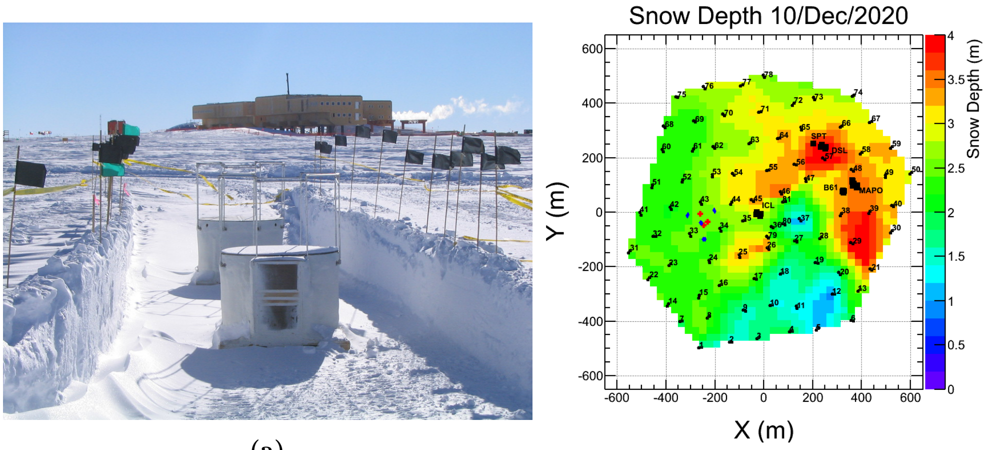

(a)

(b)

Figure 3.3: The surface array IceTop. The left picture shows an IceTop station during deployment at the South Pole. The two ice-Cherenkov tanks are 10 m apart. Today, all IceTop tanks are covered by snow. Picture credit: Tom Gaisser. On the right the snow coverage on top of the Icetop tanks in December 2020 is shown. The snow depth measurements are performed twice a year. Picture credit: IceCube collaboration.

resonance is the interaction of an electron antineutrino with an electron, forming a W^- boson,

$$\overline{\nu}_{\mathrm{e}} + \mathrm{e}^- \rightarrow \mathrm{W}^- . \tag{3.3}$$

The detected W^- decayed hadronically. In the DOMs closest to the interaction, the Cherenkov light of the secondary muons, created by meson decay in the hadronic cascade, is detected before the Cherenkov light of the electromagnetic component of the cascade, because the muons are faster than the speed of light in the ice [Ice21b].

3.2 IceTop

The main background for the neutrino observations of the IceCube Array are down-going muons from cosmic-ray air-showers [Aar+13a; HK10]. IceTop, the surface array of IceCube, is used to veto these cosmic-ray events [TP19]. It is also used for the calibration of the in-ice detector and to study cosmic-ray air-showers [Ahr+01].

81 stations are located in an area of 1 km^2, with each station close to an in-ice string. A station consists of two ice-Cherenkov tanks with an inner diameter of 1.82 m, which are separated by 10 m, see figure 3.3 a). Each tank is filled with clear ice and the walls are covered by a diffusely reflective layer made of zirconium dioxide or Tyvek [Abb+13]. Two DOMs are installed in each tank to detect the Cherenkov light. The DOMs operate at different gains, so the dynamic range is increased [Aar+13b; Ach+06; Ahr+01].

There are two types of hits for the IceTop stations: Soft local coincidences (SLC), when only one detector of a station has signal-over-threshold and hard local coincidences (HLC), when both detectors detect an event. For all SLC and HLC events the timestamp and the integrated charge is send to the ICL. For HLC events the waveform is send additionally [Abb+13]. To trigger the detection of an air-shower 6 HLC within 5 µs are necessary. On the servers in the ICL a global trigger decision is made and a preliminary analysis of the data is done. All events are stored on hard disks in the ICL and the hard disks are transfered to the North once a year. Interesting events are sent as soon as possible via satellite, with the IceCube collaboration deciding every year on what the filter criteria are [Aar+17c].

IceTop reaches its full efficiency for air showers of approximately 10^{15} eV to 10^{18} eV [Ahr+01; Aar+19]. Due to the high altitude of the array, the observation level is close to the shower maximum. This facilitates the accurate reconstruction of the primary particle [Les19]. The big advantage of IceTop for cosmic-ray physics is its location above the IceCube Array. High-energy muons that are produced in the air-shower, can be detected in the in-ice array, making IceCube a 3D detector. This also enables the measurement of the composition of air-showers: The highest energy muons, originating from the first interactions in the atmosphere, are correlated to the mass of the primary and can be measured in the in-ice detector. So if these muons are measured in coincidence with IceTop events, a separate measurement of the electromagnetic component by IceTop and the high-energy muonic component by the in-ice detector is done. Using this, it was confirmed that the cosmic-ray composition gets heavier at the second knee [Abb+13; Aar+19].

During the deployment, the IceTop tanks were buried in snow to minimize temperature variations and the accumulation of snow [Abb+13]. However, the snow height on top of tanks increases by $\approx 0.2\,\mathrm{m/year}$ on average and the accumulation is not uniform, see figure 3.3 b). The snow attenuates the electromagnetic component, which leads to increased uncertainties and a higher energy threshold of IceTop. Efforts have been made to understand and account for the attenuation [Raw16]. To further investigate these complex effects of the snow and to decrease the uncertainties, a Surface Array Enhancement is planned.

3.3 Surface Array Enhancement (SAE)

To mitigate and calibrate the effect of the snow accumulation on the IceTop tanks, a Surface Array Enhancement is planned. It consists of two detector types: scintillation detectors and radio antennas.

By increasing the active area with the scintillation detectors, the energy threshold for air-shower observations is lowered to $\approx 100\,\mathrm{TeV}$. This leads to an improved veto for the neutrino measurements of the IceCube Array. Also, the scintillation detectors have a different response to the air-showers than the IceTop tanks. Thus, the separation of

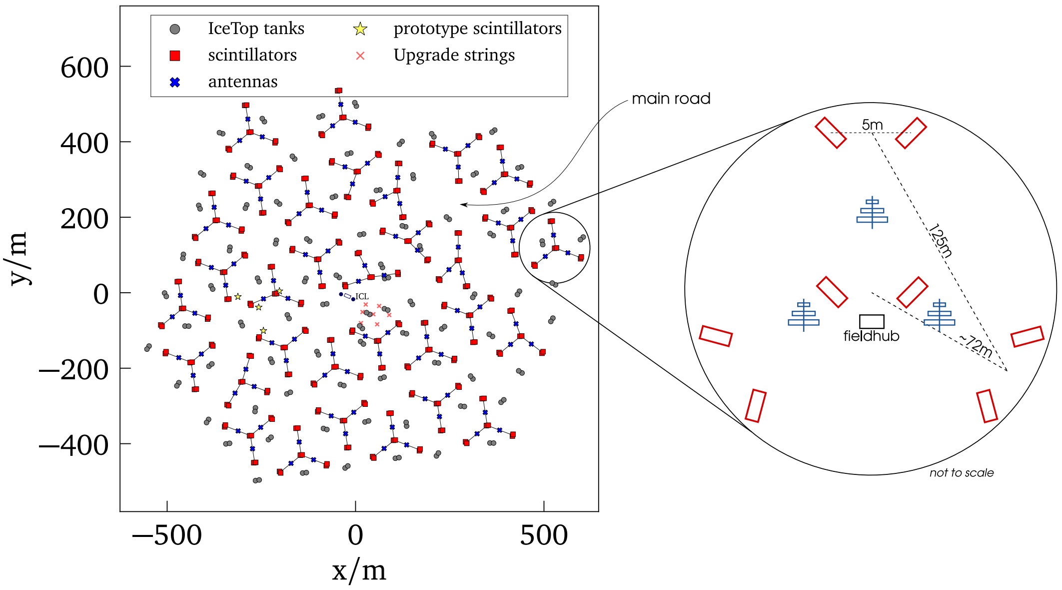

Figure 3.4: The layout of the Surface Array Enhancement takes on-site constraints, like roads and the IceCube Upgrade area, into account. Each station consists of 8 scintillation detectors and 3 radio antennas, each of which is cabled to the central DAQ in a FieldHub. The scintillation detectors are marked in red, the radio antennas in blue. Picture modified from [Les21].

the electromagnetic and the muonic component of the air showers is improved, which enables better composition studies [Les19; Les21]. Radio antennas also have a better sky coverage, going up to zenith angles of 70°. The X_{max} of an air shower can be obtained by analyzing the time structure of the radio signals, which will additionally improve composition studies [Ren20; Sch17; HSH19]. Both detector types have a high duty cycle. By combining the information gained from all detectors, scintillation detectors, radio antennas, IceTop and IceCube Array, it is possible to investigate the big questions like the origin of cosmic rays, in particular, for the transition galactic to extragalactic, the mass composition of cosmic rays and hadronic interaction models [Sch19b; Hau+19].

The layout is optimized to reduce the trenching while simultaneously achieving a uniform distribution between the IceTop tanks, see figure 3.4. 32 stations will be deployed in the current IceTop footprint [Les21; Les19; Ice19a]. Each hybrid station consists of eight scintillation detectors and three radio antennas, which are read out by a central DAQ. To avoid snow coverage, the hardware is elevated above the surface. The design allows an easy, cost-efficient deployment [Sch19b; Hau+19; Hub21; Ren20]. Further details about the hardware can be found in chapter 4.

Two prototype stations, consisting of seven scintillation detectors each, but using different DAQs, were deployed in the Antarctic Season 2017/2018 in the scope of the work of [Hub21]. Both stations worked and proved the design [Hub+17; Ice19c]. In the Antarctic season 2018/2019, one station was extended by two radio antennas in the scope of the work of [Ren20]. The final design combines the advantages of both systems and is the topic of this thesis. A prototype station, called the Surface Array Enhancement (SAE) prototype, was successfully deployed in January 2020 in the scope of this thesis, see chapter 5. The stations also serves as R&D and as the baseline design for IceCube-Gen2.

3.4 IceCube Upgrade

The IceCube Upgrade will improve the measurements of low-energy neutrino events in the GeV range and enhance the knowledge of both, the in-ice detector response and the Antarctic ice. Thus, it will open new measurements channels for neutrino astrophysics and multi-messenger observations [Ice19b].

The IceCube Upgrade is an extension near the bottom center of the existing IceCube Neutrino Observatory, consisting of seven strings with more than 700 newly developed optical sensors and calibration devices. Due to the denser spacing of the optical modules, the capability to detect neutrinos in the GeV range will be enhanced. The calibration devices like the camera system and the acoustic modules, will improve the understanding of the in-ice detector response and the optical properties of the glacial ice. The IceCube Upgrade is planned for the 2022/2023 deployment season, so the deployment will be in parallel to the Surface Array Enhancement and also serves as R&D for IceCube-Gen2 [Ice19b; IS21; Ice21e; Ice21a; Ice21f].

3.5 IceCube-Gen2

In order to measure the neutrino sky in the energy range of $\mathcal{O}(\text{TeV}) - \mathcal{O}(\text{EeV})$ and to investigate the acceleration and propagation of cosmic particles by multi-messenger observations, plans for expanding IceCube have been made. By increasing the detection volume to $7.9\,\text{km}^3$, the amount of detected high energy neutrinos and particles will be significantly increased. A better measurement of the spectral features in the high energy neutrino flux and an enhanced sensitivity for point source searches will be enabled. For this reason the next-generation observatory, IceCube-Gen2 is forseen [Aar+21; San18].

A schematic of IceCube-Gen2 is shown in figure 3.5. To instrument the ice, new DOMs are developed with an updated electronics system, while keeping the same structural elements as the IceCube DOMs. The new DOMs have a larger photocathode area, which leads to a larger photon collection efficiency. As a complementary detection channel for neutrino observations, radio antennas are deployed in shallow depths into the ice. The radio emission is generated through the Askaryan effect. This will increase the energy range for neutrino observations to EeV. Additionally, IceCube-Gen2 will have a lower uncertainty on the angular resolution of high-energy events. To veto atmospheric muons, the energy threshold will be three times higher than it is for the current IceCube, if only an in-ice veto is used [Aar+21; Aar+17a; San18].

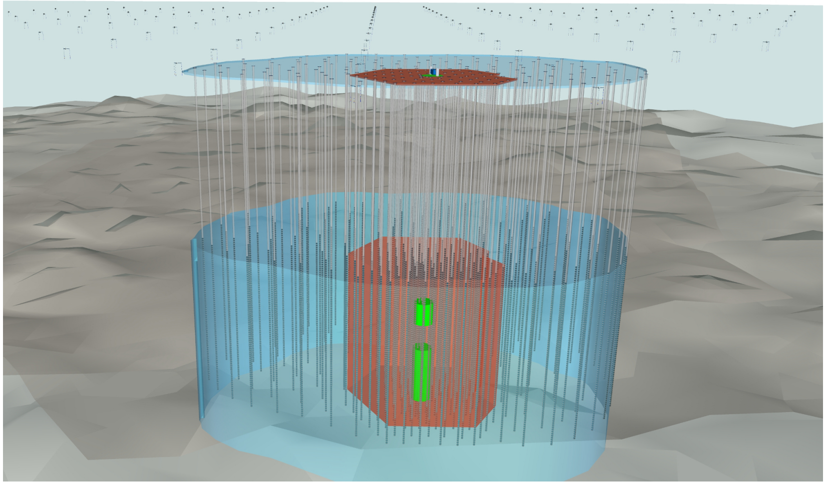

Figure 3.5: The planned IceCube-Gen2. IceCube-Gen2 consists of an expanded array of light-sensing modules in the ice with an extended surface array, shown in blue. An instrumented volume of 10 km^3 is foreseen. The currently operating IceCube Neutrino Observatory is shown in red and the densely instrumented DeepCore in green. The stations extending beyond the colored regions are the radio array [Aar+21].

It is planned that IceCube-Gen2 will also contain a surface air-shower array to extend the cosmic ray measurements and improve the veto capabilities for atmospheric muons. This will allow to reduce the energy threshold for neutrino searches in the southern sky. The surface array will consist of hybrid stations of scintillation detectors and radio antennas, similar to the stations used in the Surface Array Enhancement. A hybrid station is planned to be deployed near the top of each string. Besides acting as a veto, the surface air-shower array will be able to measure the spectrum and the composition of the primary particles of air-showers in the range 30 PeV to EeV [Aar+21; Aar+17a; San18; Hau+19; Sch19b].

4

Detectors and DAQ of the SAE prototype

In this chapter the detector system of the deployed station, the Surface Array Enhancement (SAE) prototype, will be explained. The focus will be on the scintillation detectors and the corresponding electronics, because they are the main topic of this thesis.

Two R&D scintillator stations with seven scintillation detectors each have been deployed in January 2018 [Hub+17; Ice19c; Hub21]. In January 2019, one of the stations was upgraded with two radio antennas [IR19; Ren20].

The SAE prototype was deployed in January 2020 and builds on the experiences made with these predecessors by merging and optimizing their designs. The design of the scintillation detectors was upgraded compared to the version deployed in 2018. The new electronics design allows to connect a third radio antenna to the station, which enables the direction reconstruction of the radio signals.

4.1 Overview

A station of the SAE will consist of eight scintillation detectors and three radio antennas, which are connected to a hybrid central DAQ, see figure 4.1. The central DAQ supplies power, communication and timing to the station. The signals of the scintillation detectors are digitized inside the panels by a custom electronic board, Scintillator MicroDAQ v4.1, and are then sent to the central DAQ. Also, the scintillation detectors trigger the readout of the analog radio signals inside the central DAQ. The hybrid central DAQ sends the scintillator and radio data to the surface DAQ in the ICL, using a White Rabbit layer. From the surface DAQ, the data is then transferred via a satellite link to the IceCube servers.

The power is passed on from the ICL to the central DAQ. From there the power is distributed to the scintillation detectors and the radio antennas, whereby the necessary voltages are generated by DC-DC converters inside the central DAQ.

For timing the White Rabbit (WR) system is used, providing sub-nanosecond accuracy [JPW13]. The WR switch is located in the ICL, the WR-LEN inside the central DAQ. From there, the timing is passed on to both, the scintillation detectors and the main board in the central DAQ, the TAXI board.

For communication, the surface DAQ in the ICL is connected via a 1 Gbit fiber link under a White Rabbit layer to central DAQ. The central DAQ in turn is linked with

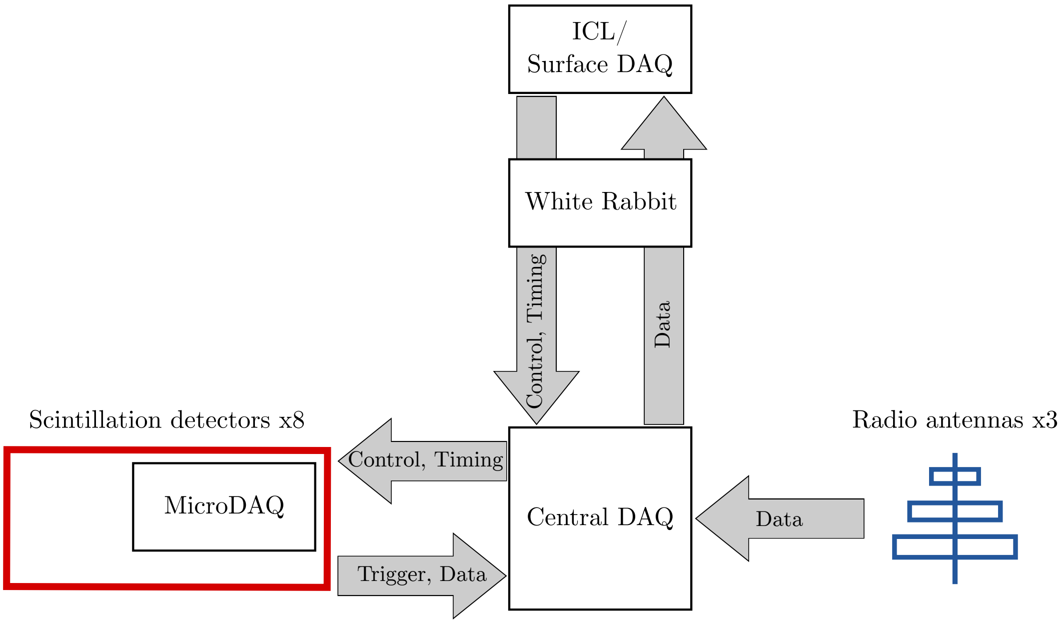

Figure 4.1: Overview of the DAQ of the SAE prototype. The scintillation detectors and the radio antennas are connected to a hybrid central DAQ. The central DAQ of the SAE prototype is deployed in the field and manages the control, timing, and data readout of both, scintillation detectors and radio antennas. It is linked to the surface DAQ, which supplies access to the SAE prototype and is used for data handling. The surface DAQ and the White Rabbit system used for timing are deployed in the ICL.

the scintillation detectors, using RS-485 [TIA98]. Further details can be found in the corresponding sections below.

4.2 Scintillation detectors and Scintillator MicroDAQs v4.1

In January 2018, two scintillation detector stations with different designs have been deployed at South Pole and performed well [Ice19c]. Based on these experiences, the designs have been merged and optimized. The design of the detectors is based on [Hub21] with a readout electronics based on the µDAQ design described in [Hub+17]. The resulting design is presented in this section.

When an ionizing particle crosses the scintillation detectors, the produced scintillation light is collected and guided via wavelength-shifting fibers to the Silicon Photomultiplier (SiPM). All fibers are connected to the same SiPM, so it measures the total scintillation light without positional information inside the detector. The SiPM signals are read out and digitized by Scintillator MicroDAQ v4.1 inside the panel. With this information it is possible to reconstruct the directions and the energies of cosmic-ray air-showers.

The scintillation detectors have $1.5\,\mathrm{m}^2$ total sensitive area, consisting of 16 extruded plastic scintillator bars, which are made of polystyrene with a doping of $1\,\%$ PPO and $0.03\,\%$ POPOP produced by the FNAL [Bez+04; PDBR03]. A $(0.25 \pm 0.13)\,\mathrm{mm}$

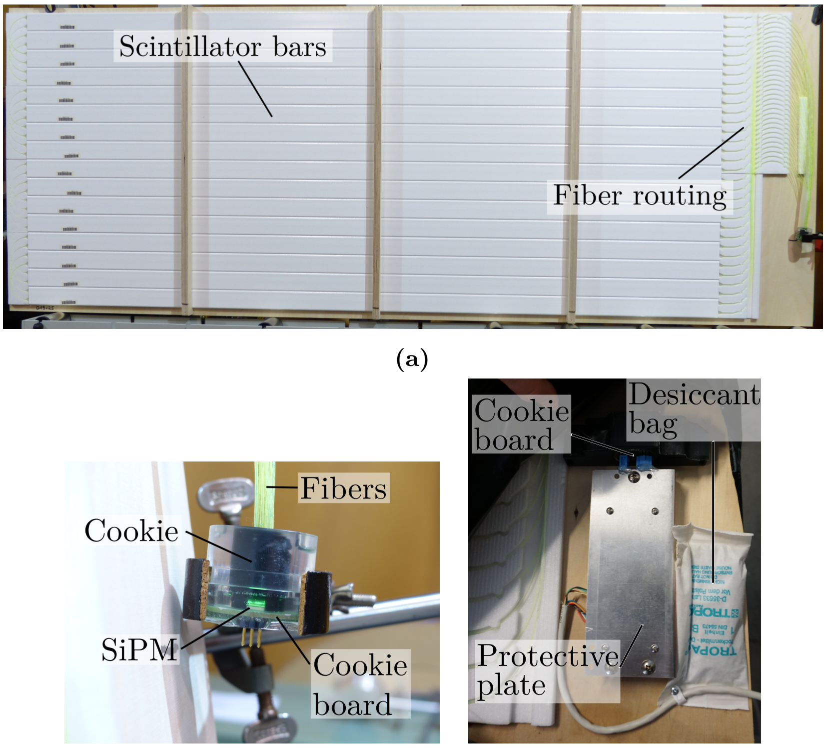

(a)

(b)

(c)

Figure 4.2: Inside view of the scintillation detectors. In a) the scintillator bars and the routing of the wavelength shifting fibers inside the detector are shown. To ensure the uniformity of the light guiding of the detector, all fibers have the same length. To avoid light losses, the minimum bending diameter of the fibers is taken into account. The fiber ends are glued to a SiPM with optical cement. b) shows a close-up of the glued cookie. The fibers are bundled in the PMMA coupler of the cookie and end approximately 1 mm above the surface of the SiPM. This avoids a loss of active area of the SiPM due to the space between the round fibers. The SiPM and the temperature sensor are connected to the MicroDAQ, which is under a protective plate, see c). To reduce the risk of moisture induced shortcuts, a desiccant bag is attached next to the electronics. Picture credit: a) and b) [Oeh18], c) photo by Michael Riegel.

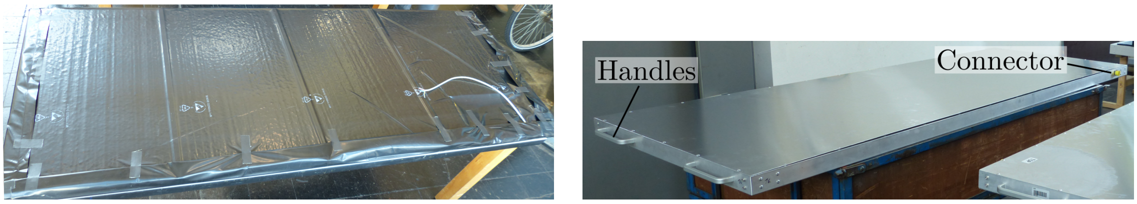

(a) **(b)**

Figure 4.3: Outside view of the scintillation detectors. a) To shield the interior of the detectors from external light, they are wrapped in light-tight foil. The edges of the foil are welded together and folded several times. The housing of the detector is shown in b). On the right side of the detector is the connector between detector electronics and the central DAQ. The handles are used for transporting and for elevating the detectors. The outer dimensions of each detector are $2.22\,\mathrm{m} \times 0.87\,\mathrm{m} \times 0.05\,\mathrm{m}$ and its weight is $\approx 43\,\mathrm{kg}$ [Hub21]. Pictures credit: [Oeh18].

thick TiO_2 coating of the bars serves as reflective layer. The dimensions of the bars are $0.05\,\mathrm{m} \times 0.01\,\mathrm{m} \times 1.875\,\mathrm{m}$ and they have two kidney shaped holes with a diameter of $(2.5 \pm 0.2)\,\mathrm{mm}$. Wavelength-shifting fibers Y-11(300) produced by Kuraray [KC] are routed through these holes. The 32 fiber ends are melted to smooth the surface to avoid light losses, are then bundled into a PMMA coupler and glued to a SiPM S13360-6025PE produced by Hamamatsu [HPDG16] with an effective photosensitive area of $6\,\mathrm{mm} \times 6\,\mathrm{mm}$, see figure 4.2. When a particle crosses the scintillators, UV light is generated, which is then shifted to blue via the dopants and then shifted to green via the wavelength-shifting fibers to increase the detection efficiency by the SiPM. A temperature sensor close to the SiPM measures the temperature of the SiPM. After the gluing process, styrofoam is placed on top of the scintillator bars and the routing to avoid a shifting of the bars and fibers. Then the detector is wrapped in opaque ESD material for light shielding and placed in an aluminum housing, see figure 4.3. The handles of the housing are used for transport and for the elevation of the scintillation detectors with poles as described in chapter 5.4. More details about the detector design can be found in [Hub21].

The Scintillator MicroDAQ v4.1 (MicroDAQ) is a microprocessor-based board placed inside the scintillation detector frames, which reads out and digitizes the SiPM signals before sending them to the central DAQ of the SAE prototype. The design is based on a previous board deployed in January 2018 [Hub+17; Ice19c] and is designed by Chris Wendt. Power, timing and communication is provided through the fanout board in the central DAQ. A photo of a MicroDAQ is shown in figure 4.4. All information about MicroDAQ is taken from [Wen; Wen17; Hub+17].

The layout of MicroDAQ is shown in figure 4.5. The temperature sensor measuring the SiPM temperature is read out and converted to Kelvin on MicroDAQ. The SiPM signal is amplified and then shaped by a linear RLC network. To increase the dynamic range, each MicroDAQ has three amplification channels. The linear RLC network creates a

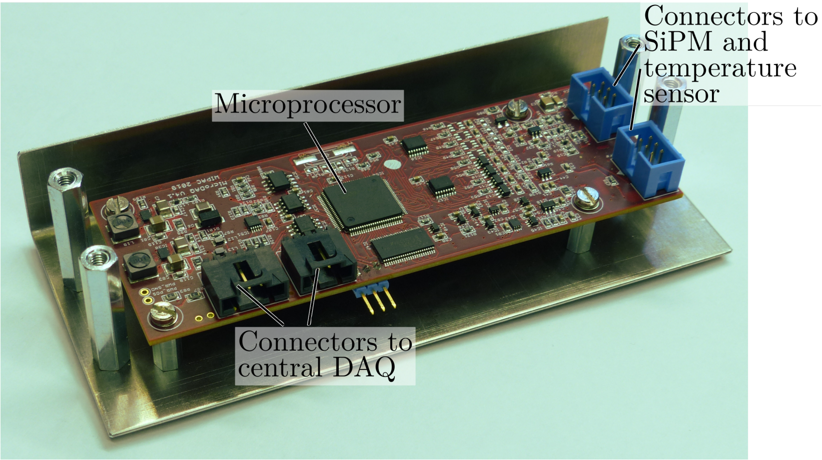

Figure 4.4: The Scintillator MicroDAQ v4.1 is the electronics inside the scintillation detectors. The analog SiPM signal and the temperature sensor are connected via the blue input connectors. The temperature is converted to Kelvin on the MicroDAQ and is sent in a digital format. The analog SiPM signal gets integrated and digitized by the three amplification channels simultaneously. The data is stored in the buffer of the microprocessor and is sent upon request to the central DAQ.

shaped signal V_{out}, which has a flat top for $\approx 100\,\text{ns}$ and which then returns to the baseline within $\approx 500\,\text{ns}$. The amplitude of the flat top is proportional to the number of single P.E.s measured by the SiPM. V_{out} is read out by 12-bit sample-and-hold ADCs and the result is saved as the charge of the measured hit. The time of the hit is evaluated using a discriminator. The timestamp corresponds to the moment when the signal surpasses the threshold. A sketch of how the pulses of the SiPM, the discriminator output and the shaped pulse correspond to each other is shown in figure 4.6.

In case a second MIP arrives, a second contribution to V_{out} is created. Like the one created by the first MIP, this second contribution itself has a flat top for $\approx 100\,\text{ns}$, before it decreases to the baseline within $\approx 500\,\text{ns}$. V_{out} is the superposition of both contributions. So the contribution created by the first MIP will start to decrease after $\approx 100\,\text{ns}$, while the one from the second is still approximately constant, resulting in an overall decrease of V_{out}. This means that the ADC sampling delay time should not exceed 100 ns in order not to underestimate the signal.

The threshold is set via a 12-bit DAC in the microprocessor of MicroDAQ. For the time capture, separate signals are generated by logic gates for the leading and trailing edges of the discriminator output to get t_{start} and t_{stop}. The time capture is done by a counter running with 180 MHz, which is synchronized to the WR signals, resulting in a time resolution of $\approx 5.5\,\text{ns}$. This is improved to $\approx 1\,\text{ns}$ by using the eight delay lines shown in figure 4.5. The signal is delayed by $\approx 1\,\text{ns}$ by each delay, resulting in an accuracy of $\approx 1\,\text{ns}$. Further details can be found in appendix A.

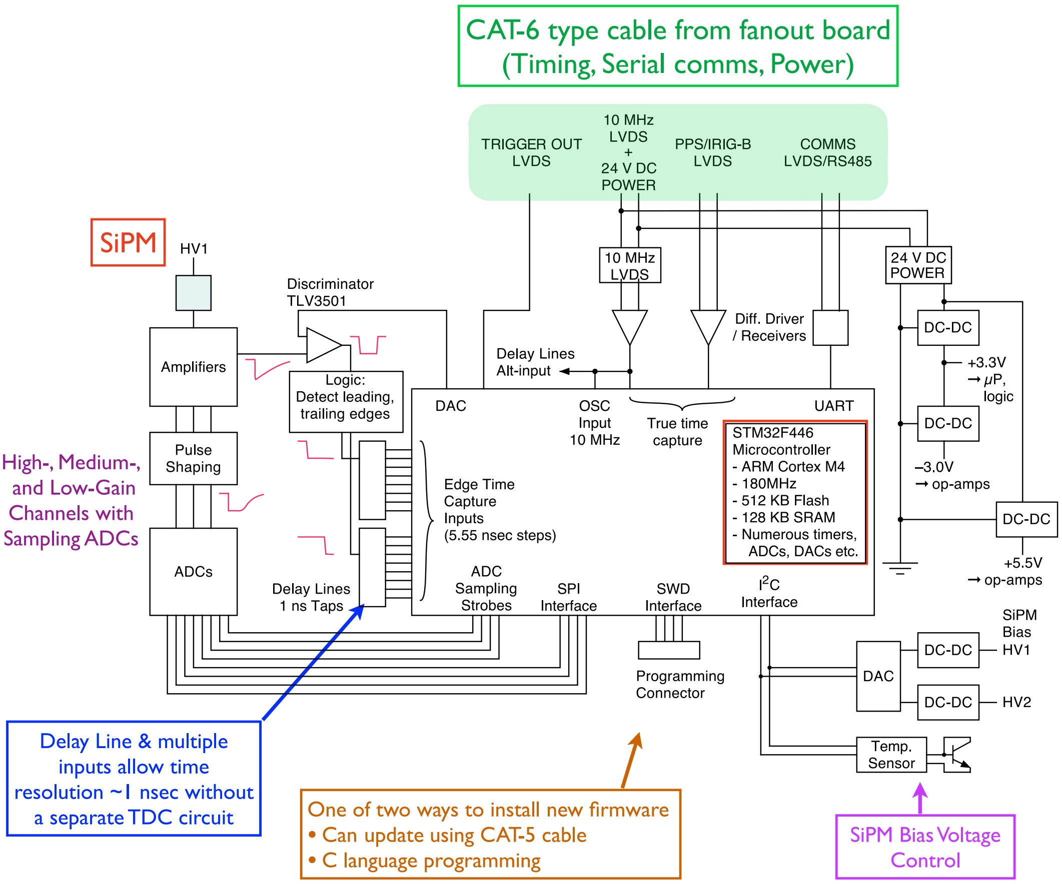

Figure 4.5: Layout of MicroDAQ. It is a microprocessor-based DAQ. The SiPM signals are amplified, shaped and then read out by ADCs. To increase the dynamic range, three amplification channels with different gains are used simultaneously. The starting and ending time of the pulse are evaluated from the discriminator output. By using the eight delay lines, the resolution can be improved to ≈ 1 ns. Picture modified from [Wen17].

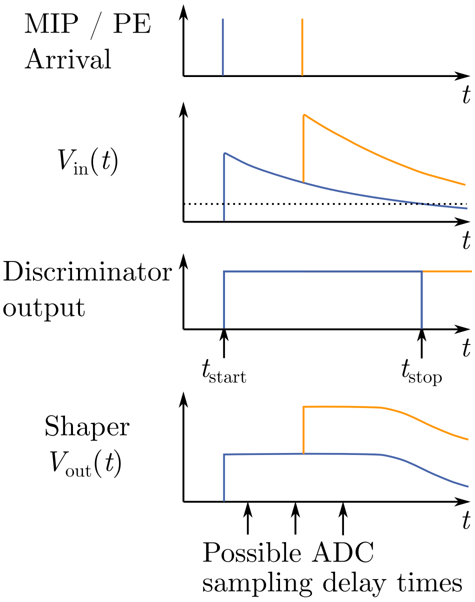

Figure 4.6: Schematic of the pulses. When a MIP passes the detectors, the resulting SiPM pulse, V_{in}, is fed into MicroDAQ. The threshold is marked as dotted line in V_{in}. When V_{in} crosses the discriminator threshold, the discriminator output changes levels and the start and stop time, t_{start} and t_{stop} are measured. In the schematic, t_{stop} is indicated for the case of a single MIP (blue curve). Simultaneously, V_{in} is amplified and fed into the shaping network. The resulting V_{out} is proportional to the charge of the SiPM pulse for $\approx 100\,\text{ns}$. Several possible ADC sampling delay times are indicated. The case of another MIP arriving shortly after the first is described in the main text. Picture modified from [Wen17].

When the signal crosses the threshold, a trigger signal is sent from MicroDAQ to the central DAQ to trigger the readout of the radio antennas. This trigger signal is coupled to the discriminator output of MicroDAQ. The length of the trigger signal sets the coincidence window for the triggering of the radio antennas and can be changed in software. For the data presented in this thesis, 1 µs is used.

MicroDAQ has two measuring modes with different data output, which are used in this thesis:

- hitbuffer data:

  For each hit the following information is saved: The time of the hit, the charge of the pulse for all three amplifications, a flag whether the hit was CPU-triggered or signal over threshold, the time over threshold. Once a second a soft-triggered (CPU-triggered) hit is saved, which can be used to evaluate the baseline. All this information is stored in the buffer of the microprocessor. When the buffer is full, the subsequent hits are not saved.

- histogram data:

  The charge of the pulses is saved as a histogram in the buffer of the microprocessor, so this charge histogram is already built on MicroDAQ. Therefore neither timing information is saved, nor whether it was a CPU-triggered hit or not. The advantage of this mode is that especially for low thresholds, longer measurement times are possible without buffer overflow.

The data is sent upon request to the central DAQ.

4.3 Central DAQ

The central DAQ of the station consists of the TAXI board, the fanout board, the radioTads and the WR-LEN, see figure 4.7. The fully assembled central DAQ with the housing open can be seen in figure 4.8.

The main board of the central DAQ is the Transportable Array for eXtremely large area Instrumentation studies (TAXI) board, whose original version was designed by Karl-Heinz Sulanke [Kar+14]. The TAXI used in this thesis is the board TAXI v3, a version modified by Alexander Menshikov. In this thesis, TAXI always refers to this board TAXI v3, which can be seen in figure 4.9. TAXI's key components are an ARM MCU (*Stamp9G45*, ARM) [tas11], running a Linux environment, which is connected via a 3 MBd connection to a FPGA Xilinx Spartan 6 (*XC6SLX45*) [XIL11] and DRS4 sampling chips [Pau16]. Details about the TAXI board can be found in [Kar+14; Hub21].

The MicroDAQ Fanout v5.0 (fanout) board connects the TAXI boards and the scintillation detectors and was designed by Chris Wendt. It is connected to the FPGA of the TAXI board via the two-pin headers, see figure 4.10. The timing, PPS and 10 MHz coming from the WR-LEN, is split on the fanout board and transferred to

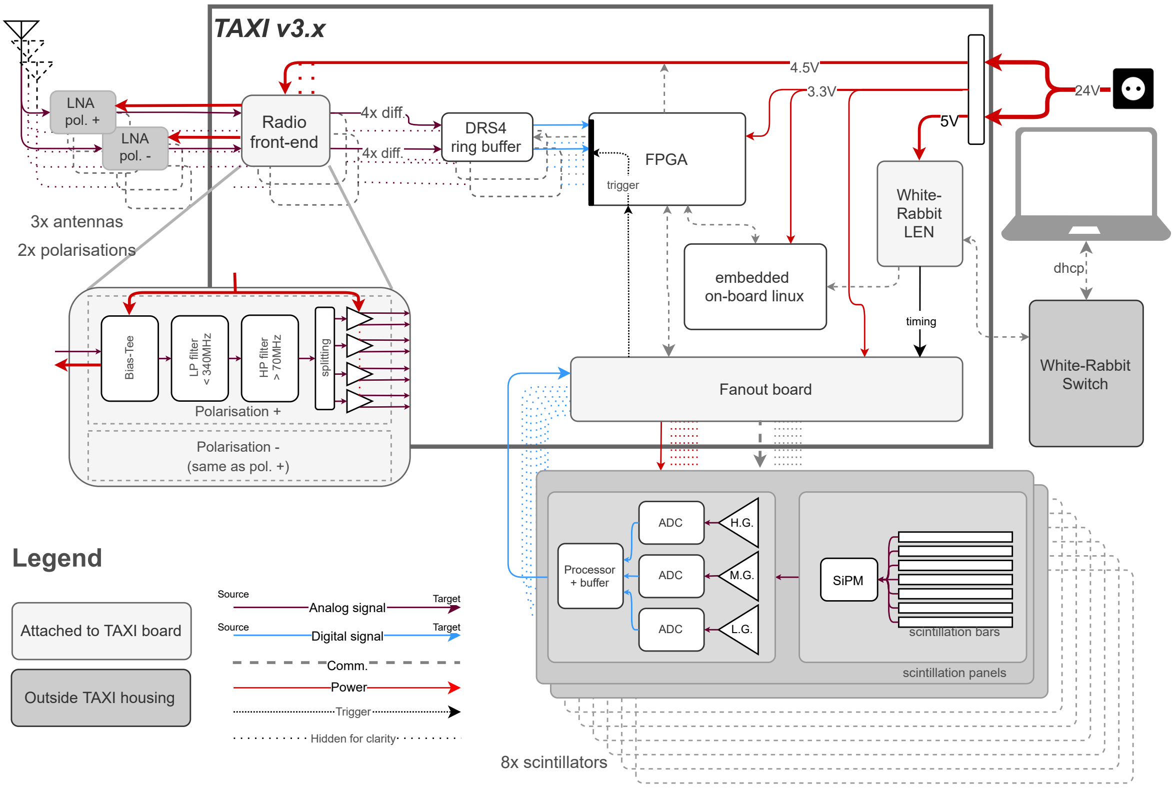

Figure 4.7: Simplified blockdiagram of the electronics of the SAE prototype. It consists of the TAXI board, the WR system, the radioTads, the fanout board, the MicroDAQs and the LNAs [Ice21c].

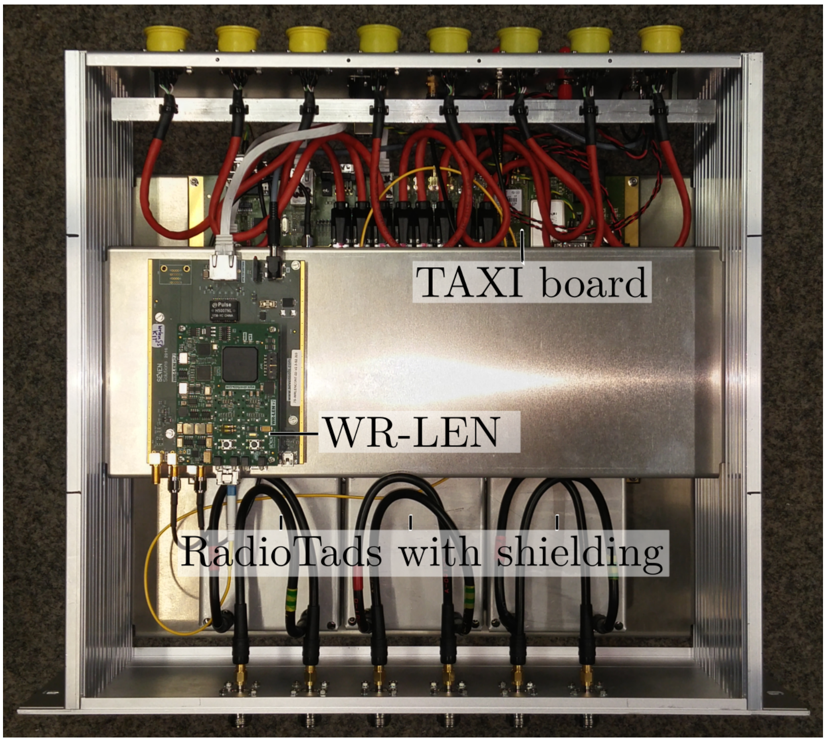

Figure 4.8: The inside of TAXI v3 no. 04 fully assembled. The WR-LEN is used for the timing and connects the central DAQ to the network of the ICL via the fiber. The fanout board for the scintillation detectors is beneath the mounting plate. The radioTads are shielded to reduce the Radio-Frequency Interference (RFI). Photo by Bernd Hoffmann.

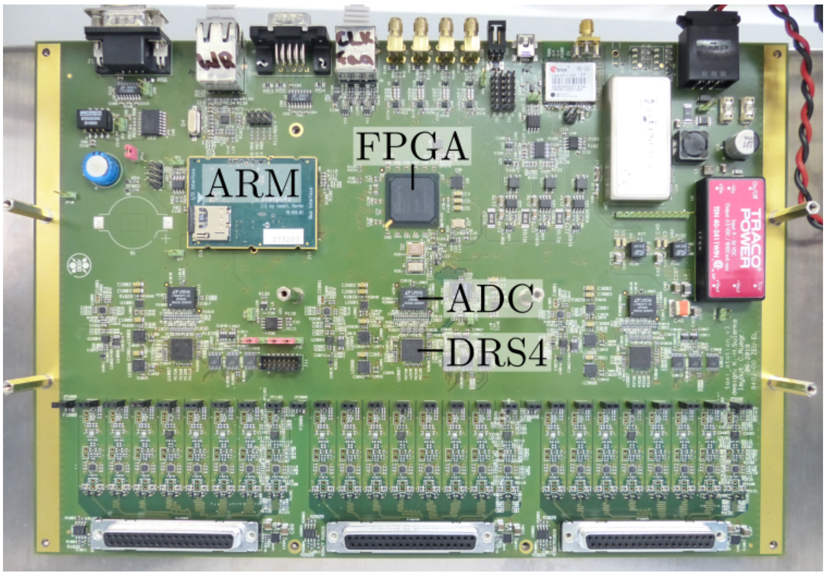

Figure 4.9: The TAXI v3 board. The Linux environment runs on the ARM, which has a 3 MBd connection to the FPGA. The analog radio signals are fed into the 37-pin connectors at the bottom of the board. Then, the signals are sampled by the DRS4s and afterwards digitized by the ADCs. The fanout board for the scintillation detectors is connected to the row of two-pin headers.

both, the TAXI board and the scintillation detectors. Via I2Cs the power of individual scintillator panels can be switched on and off. The fanout board enables communication with the scintillator panels using RS-485. All communication goes from the ARM on the TAXI board through FIFOs on the FPGA, through the fanout board to the panels and back. The scintillator data is saved to file on the TAXI board.

The scintillation detectors give the trigger signal for the readout of the radio signals with TAXI. When the scintillation detectors have a signal over threshold, they send a trigger signal through the fanout board to the FPGA on the TAXI board, where they are evaluated. The trigger condition that x_{coinc} detectors have signal over threshold within a coincident time window t_{coinc}. If it is met, the analog waveforms of the radio antennas are read out. The time interval t_{coinc} is set on MicroDAQ, by changing the length of the trigger out signal of MicroDAQ. The number of triggered detectors x_{coinc} is set on the FPGA on the TAXI board: the FPGA checks if x_{coinc} detectors have a high trigger signal at the same time. So when the trigger signal of the x^{th} detector goes up, the radio waveforms are read out and the timestamp of this moment is assigned to the radio event. x_{coinc} can be varied between 1 and 8.

The single-ended analog signals from the radio antennas, see section 4.4, are fed into the radio front-end electronics, called radioTads, see figure 4.11. These boards, based on the radioTads used in [Ren20; IR19] and redesigned by Roxanne Turcotte-Tardif, convert the signals to filtered differential analog signals, which are then transferred to the TAXI board via 37-pin D-sub connectors. As can be seen on the left side in

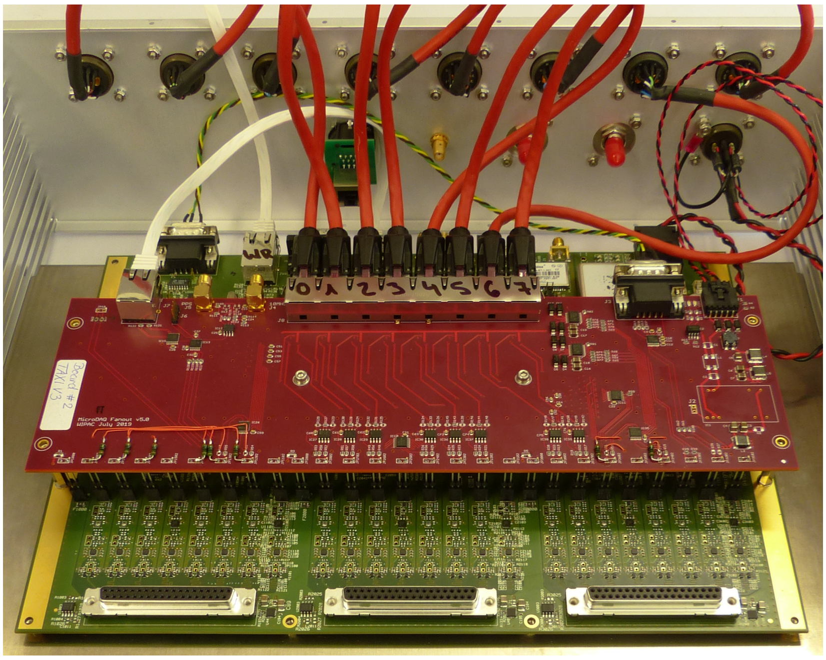

Figure 4.10: The TAXI v3 no. 04 with fanout board. The red fanout board is connected to the FPGA via the two-pin headers on the TAXI board. With the ICs on the fanout board the power of each scintillation detector can be switched and the reprogramming of one detector can be enabled. The digitized detector signals are sent through the fanout board and the FPGA to the ARM, where they are saved to file.

figure 4.7, a bias-tee is used to power the Low-Noise Amplifier (LNA) mounted directly on the antenna, while receiving the radio signal in the same cable. A low-pass filter and a high-pass filter result in a passband of 70 MHz to 350 MHz. Higher frequencies are not used, because of the air-traffic communications at 360.2 MHz at the South Pole [Uni; Rad]. Afterwards, the signal is fanned-out into four parallel amplifiers, which amplify the signals by 2 dB to 3 dB and converted them to differential pairs [Ice21c].

These differential analog signals are fed into the TAXI board. The waveforms are sampled with DRS4 sampling chips [Pau16], which are ring buffers used with a sampling frequency of 1.0 GHz. Each DRS4 has 8+1 input channels with 1024 sampling cells each. Since the radio signals are fanned-out on the radioTads, the DRS4 channels can be cascaded, thus enabling trace lengths of 1024 ns, 2048 ns or 4096 ns. When the readout of the radio waveforms is triggered by the scintillation detectors, all DRS4 channels are read out by 8-channel, 14-bit ADCs and stored into FIFOs on the FPGA. The radio data is then forwarded from "in memory" of the FPGA FIFO, through the AMR, to the surface DAQ in the ICL via TCP/IP and saved to disk there.

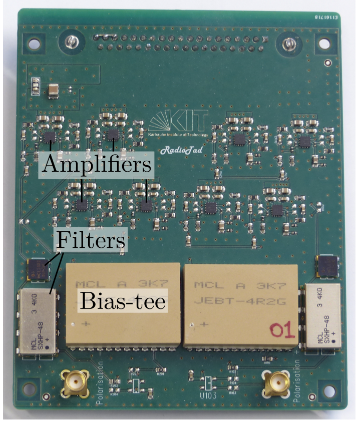

Figure 4.11: The radioTad transforms the single-ended signals to differential analog signals. The two polarisations of an antenna are fed into the same radioTad. The filters set the passband to 70 MHz to 350 MHz.

4.4 Radio antennas

Three dual polarisation Log-Periodic Dipole Array (LPDA) antennas, SKALA-2, developed by the SKA collaboration [LAFV16], are connected to the central DAQ of a station. The antennas cover a range of 50 MHz to 650 MHz [LA+15a], including the region of interest, 70 MHz to 350 MHz. A picture of a deployed antenna is shown in figure 5.7b). Each polarisation of each antenna has a LNA mounted directly at the top of the antenna, which pre-amplifies the signals with a gain of 40 dB. The noise is ≈ 40 K, which is below the Galactic and thermal noise, as desired. Measurements confirm this low noise [Ice21c].

4.5 Firm- and software

The firm- and software used for the SAE prototype builds on code from the previous stations [Hub+17; Ice19c; Hub21; Ren20]. A schematic of the TAXI software is shown in figure 4.12. All userspace applications run in the Linux environment on the ARM. These are mainly C programs and bash scripts. The majority of the data used in this thesis was acquired using programs written by Andreas Weindl. The Linux environment also serves as the networking interface to the ICL. Drivers and libraries are used to interface with the FPGA. To include the MicroDAQs, the FPGA firmware was updated during this thesis by Markus Imm.

All applications to configure and control the radio system run on the ARM. The Event Sender is a C program that forwards the radio data to the surface DAQ in the ICL via TCP/IP. The radio data is saved to disk there. Once a day the data is compressed and transferred to the IceCube data warehouses.

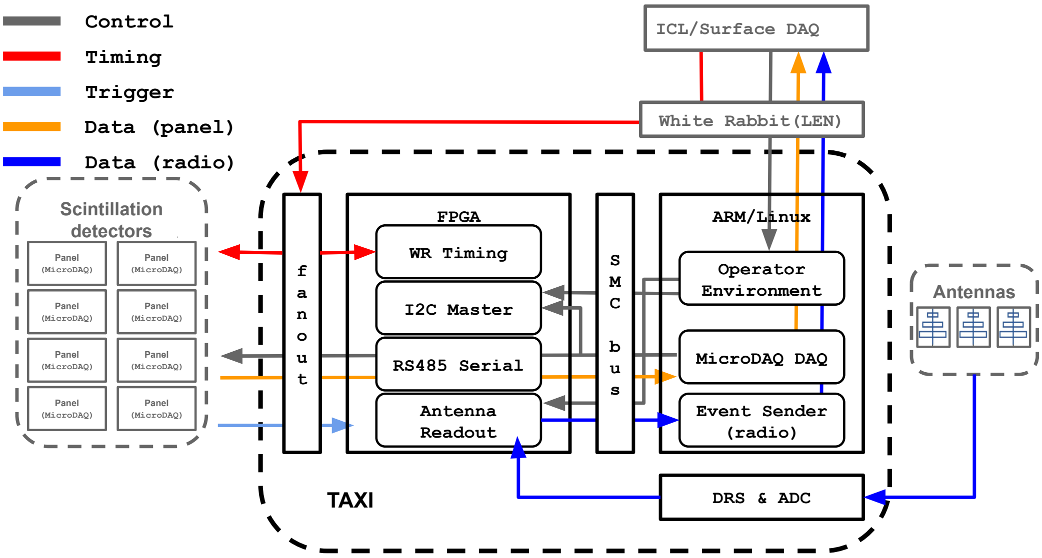

Figure 4.12: Schematic of the TAXI software. The ARM/Linux is the environment for drivers and userspace applications. The SMC bus provides an interface to the FPGA. On the FPGA low level system are running, like the RS-485 serial communication to the scintillation detectors and the I2C master for the fanout board. Also, the FPGA checks if the trigger condition is met for reading out the radio antennas. The fanout board provides links for power, timing and communication to all scintillation detectors. Picture modified from [Ben21].

The MicroDAQ DAQ are scripts and programs used to control the MicroDAQs and to acquire data from the scintillation detectors. All signals to and from the MicroDAQs go through the FPGA. This includes the RS-485 serial communications, the I2C bus for controlling the power of each scintillation as well as the I2C bus for changing communication modes between data taking and reprogramming. For the reprogramming of MicroDAQ a full-duplex communication is needed, using stm32flash. Therefore, the line, which transports the PPS signal in data taking mode, is replaced with the programming TXD line to achieve the full duplex connection in reprogramming mode.

The MicroDAQ firmware is developed by Tim Bendfelt, Chris Wendt et al. It runs on the microprocessor and is written in C. Several different MicroDAQ firmwares have been used during this thesis, see section 6.2.1. The data analyzed in chapter 8 was measured using uDAQv4.0-chw-tjb-3sec-to-20200619.bin. With all tested firmware, MicroDAQ has a data-taking mode and a data-sending mode, so it is not possible to measure while simultaneously sending the data to the central DAQ.

To obtain measurement data from the scintillators, they first need to be configured. For this the configuration commands are sent from the central DAQ to MicroDAQ. The configuration includes among others the setting of the threshold, the ADC sampling delay times and SiPM bias voltage. Then the following command structure is sent to MicroDAQ in a loop:

- Command to start data taking.
- Command to stop data taking.
- Command to send the data to the central DAQ.

The measurement time, i. e. the time between the start and stop data taking commands, is set in a program running on TAXI.

The measurement data from the scintillation detectors is sent in a digitized format to the central DAQ. It is stored in FIFOs in the FPGA, which are read out and then the data is saved to file on the ARM. The size of the FIFOs is considerably smaller than the size of the buffer on MicroDAQ, so the data is split up into frames by MicroDAQ and sent frame by frame. The frame needs to be read out of the FIFO before the next one arrives. Otherwise a FIFO overflow occurs, which leads to corrupted data. Since no handshake protocols were used during the creation of this thesis, the timing had to be optimized to minimize these FIFO overflows and transmission errors can also lead to corrupted data. Once a day the data is transferred to the surface DAQ in the ICL, is compressed and integrated into the IceCube data stream to the IceCube data warehouses. The radio and scintillator data are merged offline, after arriving in the data warehouses.

To enable continuous data taking with the scintillation detectors, it is intended to soon upgrade to new software that is currently being written. This also includes a new MicroDAQ firmware, in which the buffer on MicroDAQ is split up into 1 kB pages. As soon as a page is full, it can be read out and sent to the central DAQ. Afterwards, it is available to be written into again. Then it is possible to simultaneously write data into one page, while sending another.

5

Deployment of the SAE prototype at the South Pole

The SAE prototype was deployed at the South Pole in January 2020, replacing the previous stations. Before deployment, tests were performed to ensure the functionality of the components of the station, see chapter 5.1. Then, the deployment itself is described. The final layout can be found in chapter 5.2. The deployment of the central DAQ, the scintillation detectors and the radio antennas is described in chapters 5.3, 5.4 and 5.5, respectively.

5.1 Tests before deployment

The environmental conditions at the South Pole are harsh with temperatures dropping below $-70\,^{\circ}\mathrm{C}$. To ensure the functionality of the installed components, all were previously tested in the laboratory.

Scintillation detectors After the scintillation detectors were build in 2017, they were tested in a hodoscope, the muon tower at KIT, using different, analog detector electronics. By measuring the trajectory of muons crossing the hodoscope, the detection efficiency can be calculated as the ratio of hits in scintillation detectors and muon tower. With this, broken fibers or non-uniformity in the detection efficiency of the sensitive area can be detected. All detectors showed good results. The detector efficiency was close to 100 percent [Hub21]. Further results and details from the muon tower measurements can be found in [Hub21].

The electronics inside the scintillation detectors, MicroDAQ, was redesigned by Chris Wendt, see chapter 4.2. Before refurbishing the scintillation detectors with the new electronics, the MicroDAQs were tested by Chris Wendt. The tests included

- reprogramming the microprocessor on MicroDAQ,
- a scan of the discriminator threshold to generate hits when the discriminator threshold passes the baseline and afterwards checking these recorded hits,
- verification of the trigger signal sent by MicroDAQ for the triggering of the radio antennas,
- checking the White Rabbit timing function by requesting a timestamp and
- checking the SiPM supply voltage.

The MicroDAQs used in the scintillation detectors all passed these tests.

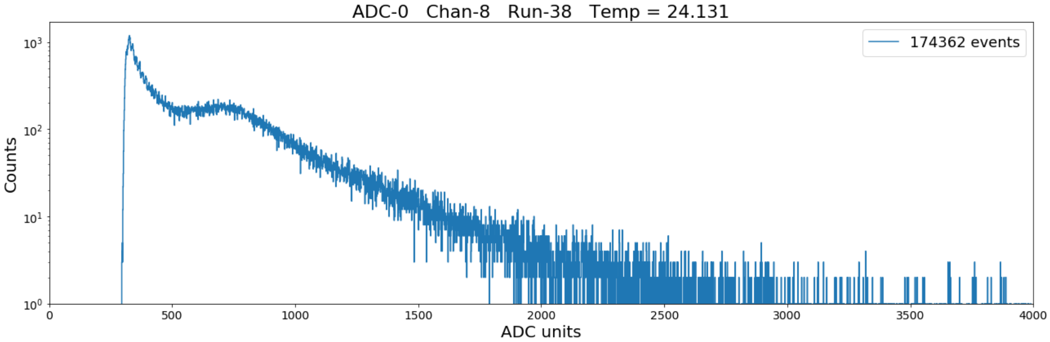

Figure 5.1: Example of a charge histogram after refurbishing the detector with the new electronics. The measurement was performed at ≈ 24.1 °C. Above the pedestal at ≈ 300 ADC units, the exponential dark noise component is apparent. The MIP peak is clearly visible at ≈ 800 ADC units. Picture credit: Matt Kauer.

After the refurbishment of the scintillation detectors with the new electronics, charge histograms were measured at room temperature and at $\approx -40\,^\circ$C to check the functionality of the detectors. The scintillation detectors were connected via a fanout board to a BeagleBone for these measurements, because the software for the central DAQ to communicate with the MicroDAQs was not written at this point. An example of a charge histogram is shown in figure 5.1. Afterwards, the panels were transported to the South Pole.

Central DAQ Before transporting the central DAQ to South Pole, it passed the following functionality tests. The central DAQ was connected to a power supply, a WR-switch, eight MicroDAQs and a function generator at the analog radio inputs. A laptop was used for controlling the setup. For easier access and to avoid thermal insulation during these tests, the housing of the central DAQ was open. First, a system test was performed at room temperature. This encompassed

- a basic functionality test, so a check if the central DAQ boots and if the communication with the central DAQ works,
- for each scintillation detector channel
  - check, if the reprogramming of the microprocessor on the MicroDAQ works,
  - verification that the central DAQ receives the trigger signals from the MicroDAQs, using the firmware uDAQv4.0-chw-trigout1Hz-20190821.bin,
  - check the communications between the central DAQ and the MicroDAQ, using the firmware udaq-raw-ascii-sept_11_2019.bin,
  - check that the timing is forwarded correctly to the MicroDAQs by requesting a timestamp,
- for each radio channel, using a sine-wave from the function generator as input signal, a check if the analog signal is digitized and saved correctly and

- a test of the temperature sensors on the TAXI board.

Then, the central DAQ was temperature cycled twice in steps of $5\,^{\circ}\mathrm{C}$ between $30\,^{\circ}\mathrm{C}$ to $-70\,^{\circ}\mathrm{C}$ and tested at each step using the test procedure described above. During one temperature cycle, the central DAQ was running continuously. While at the other temperature cycle, the central DAQ was turned off at each step for at least ≈ 30 minutes, before a cold start of the central DAQ was performed. Afterwards, the housing of the central DAQ was closed and the central DAQ was tested again at room temperature. All tests were passed successfully.

5.2 Final layout of the deployed station

We deployed the SAE prototype at the South Pole between January 10, 2020 and January 30, 2020, replacing the previous stations deployed in 2018 and 2019. We deployed a new central DAQ, eight new scintillation detectors, one additional radio antenna and replaced one old antenna mount with a new version. The buried cables from the previous stations were reused, as were the two deployed radio antennas. The scintillation detectors from the previous stations had already been disassembled, when we arrived. Also, the fiber link between the ICL and the station, which had been accidentally cut earlier in the season, had been fixed via fiber fusion splicing already.

The layout of the SAE prototype is as planned for the Surface Array Enhancement described in chapter 3.3 within the available accuracy. The positions from a GPS survey are shown in figure 5.2. To increase the visibility of both, the relative rotation and the relative position of the components of the SAE prototype, the station layout is shown in figure 5.3 with enlarged sizes. The color code used for the channels of the scintillation detectors is used throughout this thesis.

Figure 5.4 shows the central components after the deployment: the FieldHub, two scintillation detectors and a radio antenna. The deployment of the single components is described in the following chapters. Further photos of the deployment can be found in appendix H.

5.3 Deployment of the central DAQ

The first step of the deployment of the central DAQ was to retrieve the old DAQs. Due to snow drifts, the old DAQs were buried under $\approx 1.5\,\mathrm{m}$ of snow and had to be dug out. All cables were disconnected from the old DAQ, labeled with driller's tape [Cor20] and raised to ground level, since the cables were reused for the SAE prototype. During the digging of the FieldHub pit, the shielding of the fiber link broke in three places, but no measurable fiber damage was done. The shielding was fixed with driller's tape and five fibers were tested and shown to work. After retrieving the old DAQs, the pit was refilled again.

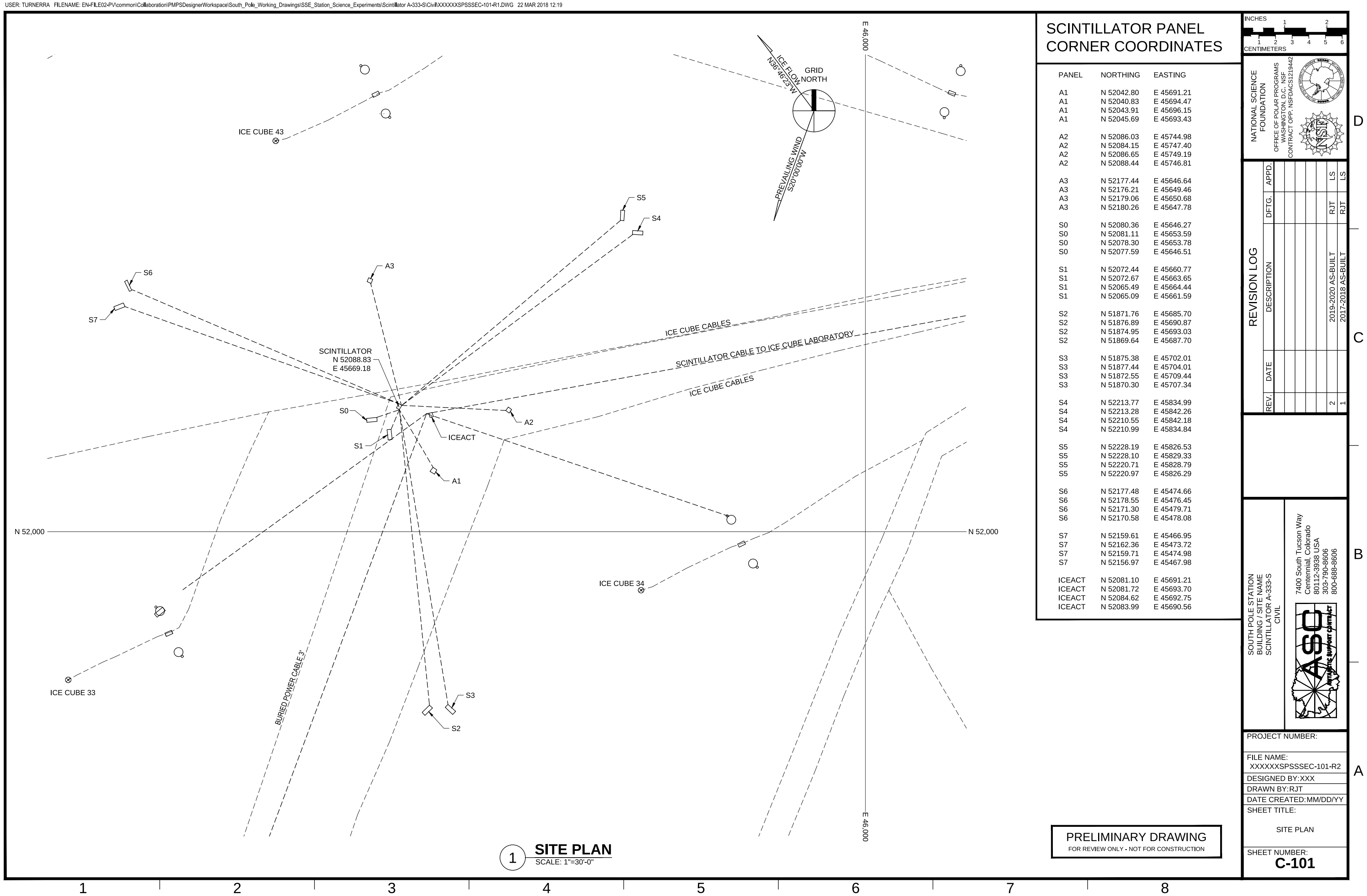

SCINTILLATOR PANEL CORNER COORDINATES

PANEL	NORTHING	EASTING
A1	N 52042.80	E 45691.21
A1	N 52040.83	E 45694.47
A1	N 52043.91	E 45696.15
A1	N 52045.69	E 45693.43
A2	N 52086.03	E 45744.98
A2	N 52084.15	E 45747.40
A2	N 52086.65	E 45749.19
A2	N 52088.44	E 45746.81
A3	N 52177.44	E 45646.64
A3	N 52176.21	E 45649.46
A3	N 52179.06	E 45650.68
A3	N 52180.26	E 45647.78
S0	N 52080.36	E 45646.27
S0	N 52081.11	E 45653.59
S0	N 52078.30	E 45653.78
S0	N 52077.59	E 45646.51
S1	N 52072.44	E 45660.77
S1	N 52072.67	E 45663.65
S1	N 52065.49	E 45664.44
S1	N 52065.09	E 45661.59
S2	N 51871.76	E 45685.70
S2	N 51876.89	E 45690.87
S2	N 51874.95	E 45693.03
S2	N 51869.64	E 45687.70
S3	N 51875.38	E 45702.01
S3	N 51877.44	E 45704.01
S3	N 51872.55	E 45709.44
S3	N 51870.30	E 45707.34
S4	N 52213.77	E 45834.99
S4	N 52213.28	E 45842.26
S4	N 52210.55	E 45842.18
S4	N 52210.99	E 45834.84
S5	N 52228.19	E 45826.53
S5	N 52228.10	E 45829.33
S5	N 52220.71	E 45828.79
S5	N 52220.97	E 45826.29
S6	N 52177.48	E 45474.66
S6	N 52178.55	E 45476.45
S6	N 52171.30	E 45479.71
S6	N 52170.58	E 45478.08
S7	N 52159.61	E 45466.95
S7	N 52162.36	E 45473.72
S7	N 52159.71	E 45474.98
S7	N 52156.97	E 45467.98
ICEACT	N 52081.10	E 45691.21
ICEACT	N 52081.72	E 45693.70
ICEACT	N 52084.62	E 45692.75
ICEACT	N 52083.99	E 45690.56

Figure 5.2: Map of the SAE prototype and the cable trenches, measured by a GPS survey of the United States Antarctic Program after the deployment. For the scintillation detectors, the positions of the four corners were measured. The position of the radio antennas was determined by the position of the baseplate.

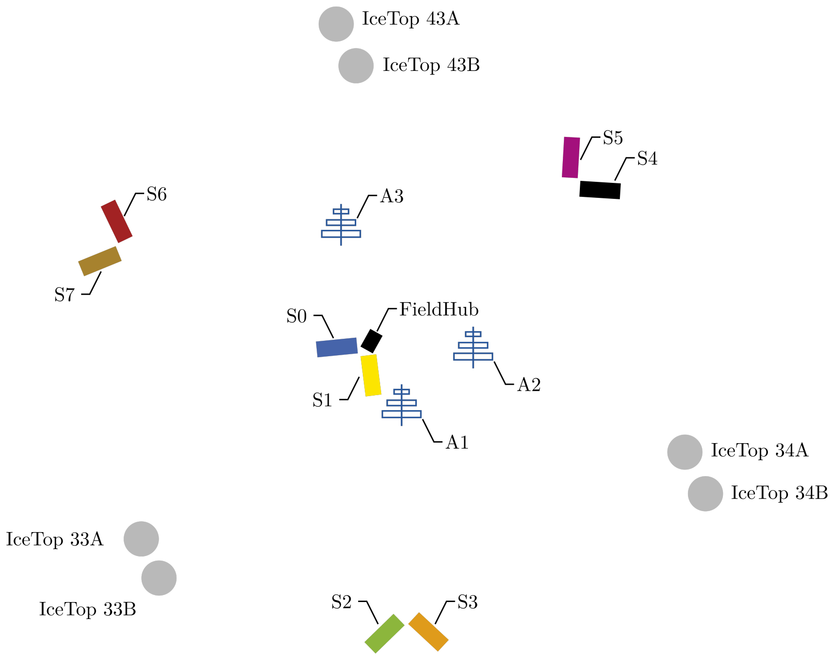

Figure 5.3: Layout of the prototype station. To increase the visibility, the sizes of the detectors and antennas are enlarged. The grey circles indicate the nearby IceTop tanks. IceTop is used as a reference detector array in chapter 7 and 8. The color code of the scintillation detectors is used also in the further chapters of this thesis.

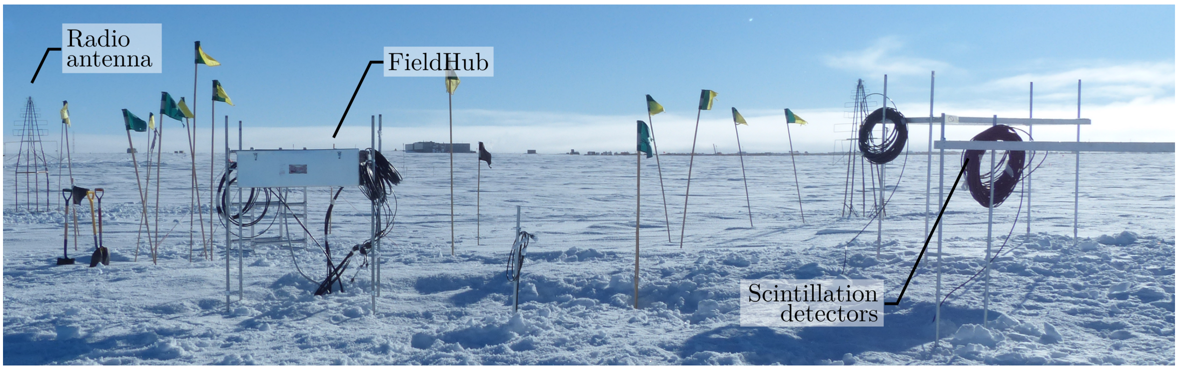

Figure 5.4: Photo of the center of the SAE prototype. The central DAQ is in the elevated FieldHub. The two central scintillation detectors (channel 0 and channel 1) can be seen on the right side. On the left side in the background, antenna A2 elevated on a new mount is visible. Picture credit: Marie Oehler, IceCube/NSF.

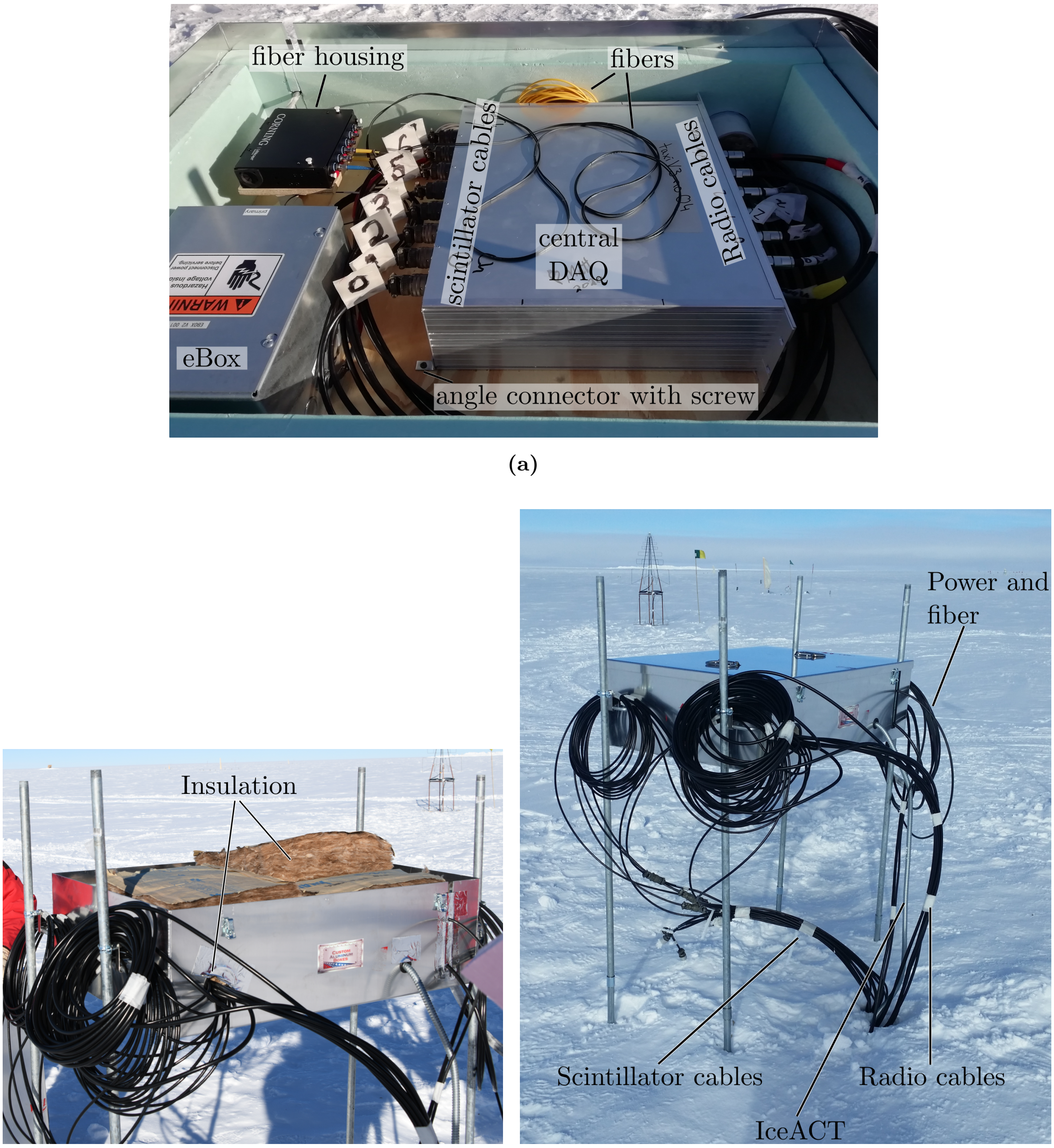

(a)

(b)

(c)

Figure 5.5: Deployment of the FieldHub and the central DAQ. The space inside the FieldHub is limited, especially due to the stiffness of the cables. To fasten the electronics, everything is screwed to the wooden plate located at the bottom of the FieldHub, see a). For the central DAQ, angle connectors are used for the fastening. The eBox provides the power for the SAE prototype and the nearby IceACT telescope. The communication with the central DAQ and the timing signal for the SAE prototype is done via a fiber link to the ICL via the fiber housing. Since the electronics are not buried, larger temperature variations of the central DAQ are expected than for the previous stations. To stabilize the temperature for the electronics and to keep the operation temperature of the electronics as warm as possible, a lot of insulation is used, see b). This includes extruded polystyrene foam on the inner walls of the FieldHub, fiberglass batting on top of the electronics and polyethylene foam to seal the feed throughs. The FieldHub is elevated to avoid snow coverage, see c). The cable slack is rolled up and hanging from the poles. Picture credit: Marie Oehler, IceCube/NSF.

Before the deployment in the field, the central DAQ of the SAE prototype was tested in the ICL to ensure that it was not damaged during transport. An optical inspection was followed by a check of the power, establishing an ssh connection and a check of the communications with the central DAQ. Then the central DAQ of the SAE prototype was deployed in the elevated FieldHub designed by John Kelley, see figure 5.5. The FieldHub serves as R&D for the FieldHubs of the future IceCube-Gen2. Due to the elevation, the electronics are easily accessible in coming seasons without digging. The power for the central DAQ is provided and can be switched on and off remotely via the eBox. Communication and timing is done via a fiber link to the ICL using a WR-layer.

Since the space inside the FieldHub is limited and the cables are stiff, first the cables had to be connected to the central DAQ, before it could be screwed to the wooden baseplate, so this had to be done in the field. After receiving IP addresses for the TAXI and the WR-LEN inside the central DAQ, the deployed central DAQ was tested. Ping and logging into TAXI via ssh worked, as did taking radio test data and rebooting the system.

5.4 Deployment of the scintillation detectors

The scintillation detectors of the SAE prototype reuse the buried cables from the previous stations. To be able to elevate the scintillation detectors, extension cables with a length of 25 ft each were attached to both ends of the cables, amounting to a total cable length of 85.24 m. The scintillation detectors were transported to their destination on a snow mobile. According to the station layout of the Surface Array Enhancement, the two neighboring detectors are at 45° angle to the radial axis of the center of the SAE prototype and the centers of the detectors are 5 m apart. To achieve this layout, a square box and poles were used, see figure 5.6a).

The scintillation detectors are elevated on poles with hooks ≈ 1.2 m above the surface to ensure that the scintillation detectors are not covered by snow drifts. Different types of poles and hooks were used to benchmark the types against each other. So far no difference in the performance could be observed, but the poles using threaded connectors were easier to deploy. To increase the stability, two posts are screwed together, so that more than 1.5 m of each pole is below the surface. The snow has a layered structure with different densities. Therefore, some poles sank into the snow very easily, which leads to a reduced height of the scintillation detectors above the ground, while others had to be driven in by force using a pile driver. Then the scintillation detectors are hooked in using the handles, see figure 5.6b). All poles are extendable by attaching another post, so the scintillation detectors can be elevated further, when snow drifts make it necessary. Two fully deployed scintillation detectors are shown in figure 5.6c).

The channel numbers of the scintillation detectors are marked by labels on a pole made of driller's tape. To confirm the assignment of the scintillation detectors to the

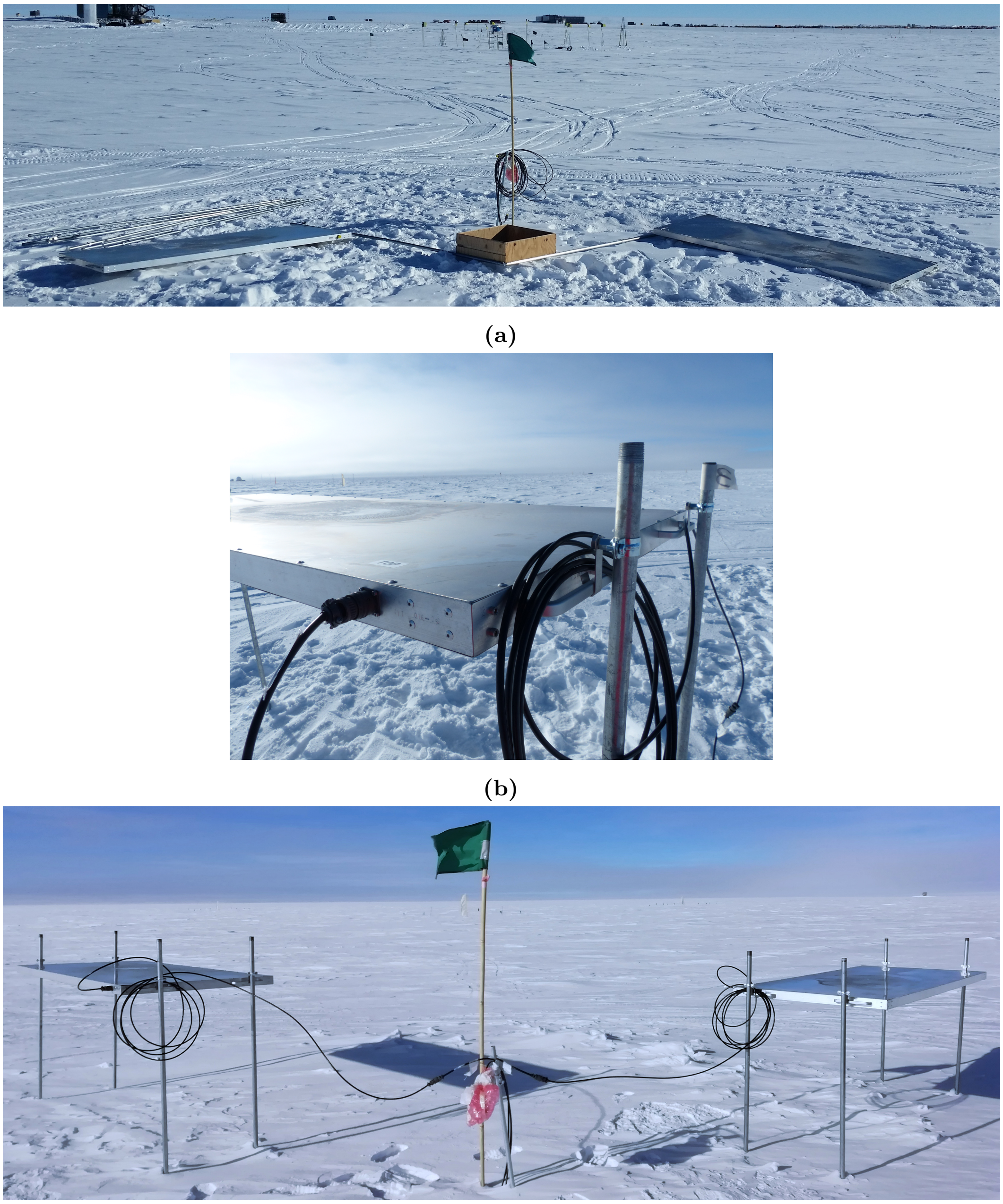
(a)

(b)

(c)

Figure 5.6: Deployment of the scintillation detectors. a) shows how the alignment of the panels was performed. First, a corner of a square box was aligned towards the center of the station. Then, by using two poles as extensions, the angle and the distance between the neighboring detectors was set. To avoid snow coverage, the detectors are elevated above the ground using four poles. For this the handles of the scintillation detectors are suspended into hooks, each fastened to a pole, see b). The cable slack, which is necessary to elevate the panels further in ≈ 5 years, is hanging from one of the poles. c) shows two neighboring scintillation detectors after deployment. They are at a 90° angle to each other and their centers are 5 m apart. Photo credit of a): Matt Kauer, IceCube/NSF, b) and c) Marie Oehler, IceCube/NSF.

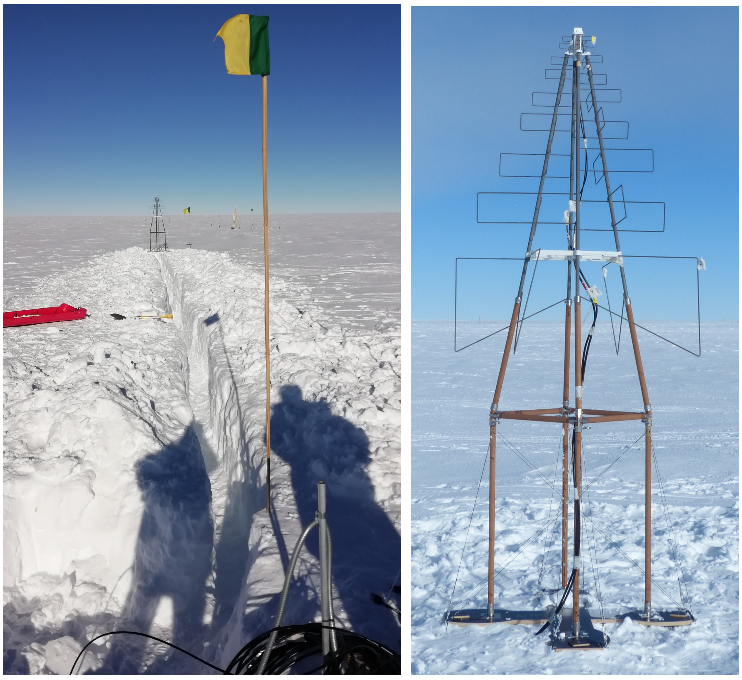

(a) (b)

Figure 5.7: Deployment of the radio antennas. For the deployment of the third antenna, the $\approx 30\,\mathrm{m}$ cable trench had to be trenched by hand, see a). b) shows a fully deployed radio antenna. The mahogany mount elevates the antenna above the surface. Both mounts can be extended by attaching extension poles on top of the four vertical poles. Picture credit: Marie Oehler, IceCube/NSF.

channels of the central DAQ, a test measurement was made with only the even channels connected. Since at the time of deployment the firm- and software of the central DAQ was not fully programmed, the communication, the trigger lines from MicroDAQ to the central DAQ and the reprogramming of the microprocessor on MicroDAQ was tested using special MicroDAQ firmwares and TAXI scripts.

5.5 Deployment of the radio antennas

In January 2019 two radio antennas were deployed, extending the scintillator station. These two antennas and the corresponding cables were reused for the SAE prototype, elevating one of these antennas above the ground by changing the antenna mount to a new version. The other radio antenna was already elevated $> 1\,\mathrm{m}$ above the ground. Additionally, a third radio antenna was deployed, also elevated by a new antenna mount.

The new mount for the radio antennas was designed by Roxanne Turcotte-Tardif and can be seen in figure 5.7b). It consists of sapele mahogany. A baseplate on the ground is fixed with 1 m long wooden snow spikes. Four 1 m dowels are connected to a square brace, to which the radio antenna is fastened. By adding extension dowels below the brace, the mount is raisable [Ice21c].

To deploy the third radio antenna, a new cable trench had to be dug by hand with a length of $\approx 28\,\mathrm{m}$ and a depth of $\approx 1\,\mathrm{m}$, see figure 5.7a). After putting in the cable, it was secured using magnetic band $\approx 30\,\mathrm{cm}$ above the cable to ensure that it can be found and retrieved again, before refilling it with snow. The radio antenna was assembled inside the ICL and then transported together with the mount to the deployment site with a snow mobile. The ground was slightly leveled, before placing the base plate. The deployment of both, the mount and the antenna was successful. Fixing the baseplate with the snow spikes worked well; the spikes did not break when we hammered them into the ground. The lower support bracket broke, but could be fixed with driller's tape. Washers were used for leveling the radio antenna, to ensure that the axis is perpendicular to the ground. A fully deployed radio antenna with a new mount is shown in figure 5.7b).

Background radio data was measured during the deployment to test the radio antennas and the part of the central DAQ, which records the radio data. The recorded radio waveforms look reasonable, so recording of radio waveforms functions as anticipated. Additionally, DRS4 baseline calibration runs were performed successfully.

6

COMMISSIONING

After the deployment, the commissioning had to be done, before data could be measured and read out from the SAE prototype. This chapter describes the commissioning steps for the timing of the SAE prototype in chapter 6.1, the scintillation detectors in chapter 6.2 and the radio antennas in chapter 6.3.

6.1 Timing

After the deployment, it was found that the SAE prototype is not receiving timing information from the WR system. This was caused by a misconfiguration in the WR-LEN init script, which sets a static IP address, which is not served by the DHCP network. Thus, the WR-LEN was not reachable from the network, so the IP address could not be changed and the SAE prototype did not receive valid timestamps. To reconfigure the WR-LEN, a separate DHCP network was created, which assigns the static IP address to the WR-LEN. With this, it was possible to log into the WR-LEN and configure it. Since then, the timing of the SAE prototype works.

6.2 Scintillation detectors

The commissioning steps for the scintillation detectors comprise the communication between the central DAQ and the MiroDAQ and the trigger signals for the readout of the radio antennas.

6.2.1 Communication

At the time of deployment, the firm- and software for the SAE prototype was not fully programmed. Therefore only checks of the communication and trigger lines could be performed.

Extra 0xFF During the development of the software, it was found that for commands sent from the central DAQ to a MicroDAQ, several undesired 0xFF are received by the central DAQ. This is due to a flank and the following high baseline, which is created by a chip on the fanout board, when switching between transmitting and receiving in the communication. Since these 0xFF occur at predictable places in the data stream, they are filtered out offline during the data processing.

Corrupted data The full firm- and software was tested during the writing process. For the scintillation detectors, the data is split up into frames, each containing a 16-bit Fletcher checksum [Fle82] and being encoded using Consistent Overhead Byte Stuffing

(COBS) [CB99] with the delimiter zero. However, the data received from the scintillation detectors in the test measurements was always corrupted, so either the COBS-decoding or the verification of the checksum failed. This indicated that the communication did not work properly. Therefore, the communication was checked for transmission errors.

Looking at the communication lines with an oscilloscope on a clone located at the Campus North of KIT consisting of the central DAQ connected to eight MicroDAQs, did not show any transmission errors. An echo test was written, in which data packets are sent to MicroDAQ, which mirrors the message using the firmware udaq-echo-aug_6_2019.bin. Then the answers were verified offline, showing only negligible differences. For example, in one run with 150000 data packets, each containing 1000 bytes, only 23 data packets showed differences. All differences were missing parts of a data packet, but no change in the pattern.

In parallel, many firmware versions were written for MicroDAQ by Tim Bendfelt and tested in combination with various versions of firm- and software of the central DAQ. A list of all tested MicroDAQ firmwares can be found in appendix A.4. Some of these mirrored all communication to the debug output of MicroDAQ to check if it matches the communication with the central DAQ. These showed that MicroDAQ receives the commands correctly, but showed discrepancies between the frames sent by MicroDAQ and the ones received by the central DAQ. This and the results from the echo tests indicate a problem related to the timing of transmitting and receiving.

Therefore, Andreas Weindl wrote C-programs for the central DAQ with different timings. Finally, a combination of firm- and software for the MicroDAQs and the central DAQ was found with stable communication on the clone setup at KIT. For the SAE prototype deployed at South Pole, further optimization of the communication delays and a power cycle on November 27, 2020 were necessary to ensure a stable communication. Now, the corruption rate of the files is below 15 %, see figure 6.1

Dead time As described in chapter 4.5, the firm- and software used in this thesis does not allow the scintillation detectors to measure while simultaneously sending the data. Therefore, the commands to start measuring, to stop measuring data and to send the data are sent to all MicroDAQ in a loop. This leads to a firm- and software-induced dead time in addition to the dead time of the scintillation detectors, which is evaluated in chapter 7.1.6. For measurements with all eight scintillation detectors measuring simultaneously, the following dead times are obtained for the two different measurement modes.

- Hitbuffer data: A typical measurement time m, before the buffer of MicroDAQ is full, is $m \approx 35\,\mathrm{s}$ for the highest possible threshold (DAC 4095) and $m \approx 6.5\,\mathrm{s}$ for a threshold of $\approx 0.5\,\mathrm{MIP}$. A typical file size is 65 kB. The communication speed is 3 MBd.
    - Theoretical limit: This leads to a readout time of a single MicroDAQ r of 0.2 s. Since the detectors are read out sequentially that gives a total dead

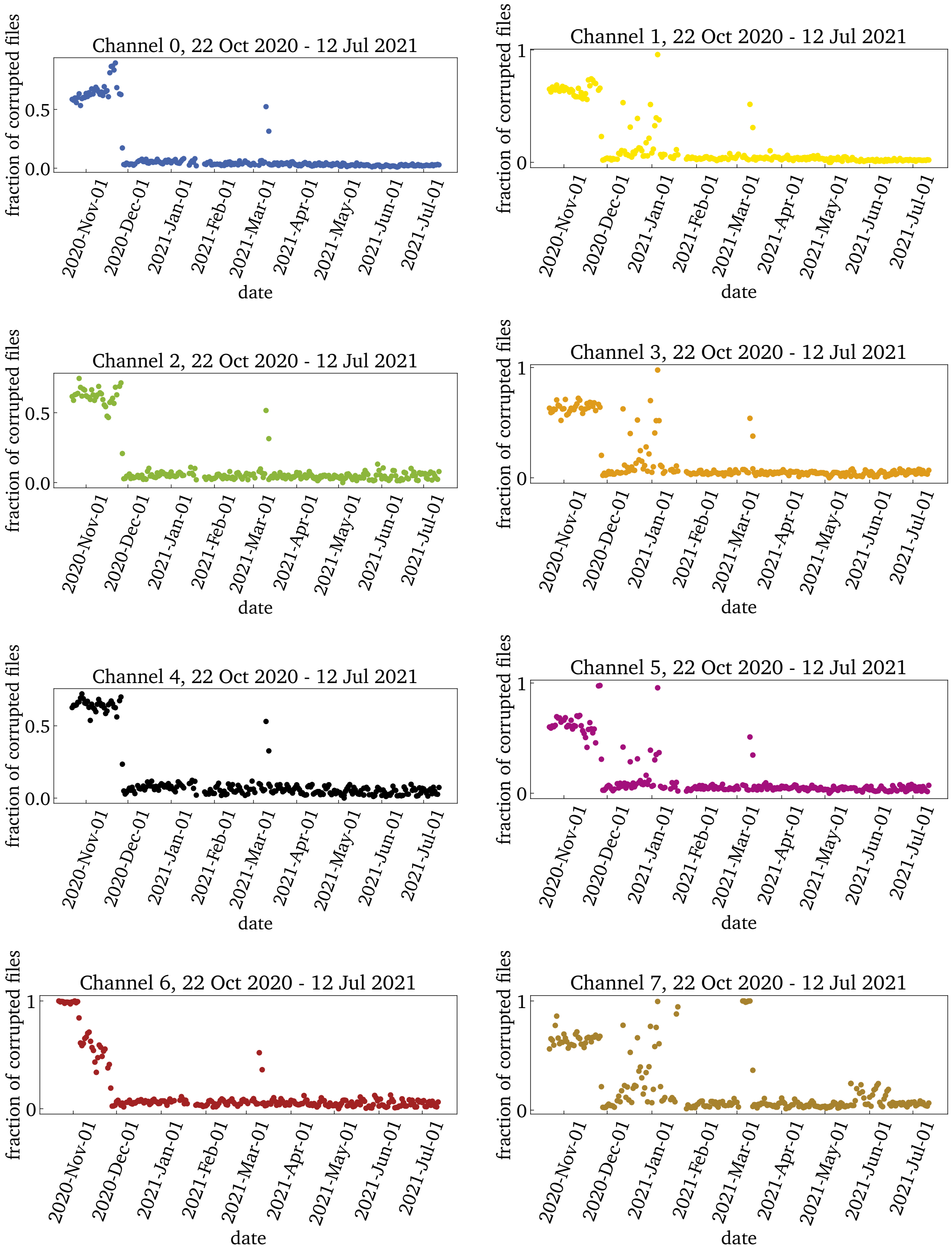

Figure 6.1: Fraction of corrupted files of total number of files per channel and day from October 22, 2020 until July 12, 2021. After improving the soft- and firmware, especially with regard to the timing of the communication, and a power cycle on November 27, 2020, the fraction of corrupted files dropped. Since then, the higher number of corrupted files on single days can be explained by special runs or a not valid timestamp of the detector. The higher corruption rate of channel 7 from end of May until beginning of June is still under investigation.

    time of $\tau_{\text{DAC }4095} = \frac{8r}{8r+m} \approx 4.4\,\%$ for the highest possible threshold and $\tau_{0.5\,\text{MIP}} \approx 19.8\,\%$ for a threshold of ≈ 0.5 MIP.

  - Reality without parallel radio data taking: Since the FIFO depth on the FPGA is smaller than the buffer size of MicroDAQ, the data needs to be split up and sent in frames. A frame write delay of 300 µs is set on MicroDAQ to give the central DAQ the time needed to read out the FIFO. This leads to a readout time of $r \approx 1.4$ s and consequently a dead time of $\tau_{\text{DAC }4095} \approx 24.2\,\%$ and $\tau_{0.5\,\text{MIP}} \approx 63.3\,\%$.
  - Reality with parallel radio data taking: Additionally to the limited size of the FIFO, problems were found when multiple processes use the FPGA at the same time, leading to a higher rate of corrupted scintillation detector data files and a slower readout. This gives a readout time of $r \approx 7.5$ s and hence a dead time of $\tau_{\text{DAC }4095} \approx 63.2\,\%$ and $\tau_{0.5\,\text{MIP}} \approx 90.2\,\%$ respectively.
- Histogram data: A typical file size for a histogram is 13 kB, which are sent with 3 MBd.
  - Theoretical limit: This leads to a readout time r of a single MicroDAQ of 0.04 s and a total dead time of $\tau_{\text{histog}} \approx 0.2\,\%$.
  - Reality with parallel radio data taking: The data is sent in frames with a frame write delay of 300 µs to account for the limited FIFO depth. For histogram data, the frames are shorter, consisting only of one bin of the histogram, which leads to an increased readout time of $r \approx 30$ s due to the frame write delay. Therefore, the dead time τ_{histog} is $\approx 61.5\,\%$.

However, as mentioned in chapter 4.5, a new firm- and software for the SAE prototype to reduce the dead time will soon be ready for deployment. This new firm- and software will allow the MicroDAQs to simultaneously measure and send the data to the central DAQ, as well as optimized communication between the MicroDAQs and the central DAQ. Thus, the dead time due to the current firm- and software will be eliminated.

6.2.2 Triggers

In the measuring mode, the MicroDAQs send out a trigger signal when they record a hit with signal-over-threshold. These triggers were observed in the central DAQ and were used for triggering the radio antennas. If six scintillation detectors observe a hit within 1 µs, the waveforms of the radio antennas are read out. This was possible, even when the data from the scintillation detectors were corrupted, see chapter 6.2. An analysis of one day of radio data by Serap Tilav showed that approximately 75 % of the events triggered by the scintillation detectors with a maximum threshold have corresponding IceTop events [Til20]. This proves that the scintillation detectors work and measure cosmic-ray air-showers.

Since November 24, 2020 no more triggers were received from channel 5, but communication and data taking with the scintillation detector still work. The reason for this is unknown. Neither reprogramming and reconfiguring the MicroDAQ fixed it, nor a power cycle. To check if the cause is inside the scintillation detector or in the central DAQ, the cables of the neighboring scintillation detectors on channel 4 and 5 were swapped by the winterovers, the on-site IceCube operators, on January 18, 2021, so that the scintillation detector previously connected to channel 5 is now connected to channel 4. Still no triggers were received on channel 5. This shows that the MicroDAQ itself is still working. Possible reasons for not receiving triggers are the cabling of the central DAQ, the connector or throughput at the central DAQ, the routing on the fanout board or the TAXI board or the FPGA intput. On January 24, 202 the cables were swapped back to the original layout.

6.3 Radio antennas

Since the deployment, the radio antennas measure software-triggered background events. Further details on the background data can be found in chapter 7.2. Since the scintillation detectors could be configured and put into measuring mode, scintillator-triggered events are recorded additionally. For events measured in coincidence with scintillation detectors, radio antennas and IceTop, see chapter 8.6.

The operating parameters cascading and SerDes delay were optimized. As described in chapter 4.3, the trace length of the sampled radio waveforms can be set to 1024 ns, 2048 ns or 4096 ns by cascading the DRS4 channels. The advantage of a short trace length of 1024 ns is that the analog radio waveform is sampled in four DRS4 channels in parallel. Therefore, noise spikes, which occur in individual traces and could be misinterpreted as radio air-shower signals, can be filtered out by taking the median of the four traces. The advantage of the long trace length of 4096 ns is a better signal-to-noise ratio due to the relative lengths of the air-shower signal and background signal. The relative timing between the trigger signal and the readout of the radio waveform is set via the SerDes delay, using the Serializer Deserializer (SerDes) blocks in the FPGA. Thus, the interesting region, containing the air-shower event, can be shifted in the sampled trace. Since April 23, 2021, the SAE prototype samples radio waveforms with a trace length of 4096 ns and a SerDes delay of 256.

7

CHARACTERIZATION OF THE SCINTILLATION DETECTORS AND RADIO ANTENNAS

In this chapter the characterization of the scintillation detectors and the radio antennas is described in 7.1 and 7.2, respectively, with the main focus on the scintillation detectors. The characterization is necessary to understand and correctly interpret the data obtained from the detectors. The characteristics of the entire SAE prototype, so for example the angular resolution of the SAE prototype, is evaluated from air-shower measurements and can be found in chapter 8.

7.1 Characterization of the scintillation detectors

The characterization of the scintillation detectors includes the calibration of the MicroDAQ settings, like the SiPM supply voltage and the threshold, as well as the temperature sensor in chapter7.1.1. The hit rate as a function of the threshold is presented in chapter 7.1.2. Additionally, the stability of the baseline is assessed in chapters 7.1.3 and 7.1.4. The timing and the dead time are evaluated in chapters 7.1.5 and 7.1.6, respectively. The calibration of the scintillation detectors with respect to MIP is done using the measured charge histograms. For this, the gain and the MIP light yield is evaluated in chapter 7.1.7. The temperature compensation is explained in chapter 7.1.8 and the saturation of the scintillation detectors is determined in chapter 7.1.9.

7.1.1 Characterization of settings of the Scintillator MicroDAQs

To operate the scintillation detectors and interpret the data correctly, a characterization of the main scintillation detector settings is necessary. This includes the temperature sensor, the SiPM supply voltage and the threshold.

Temperature sensor Since the SiPM is a semiconductor device, it has a temperature dependent behavior. Therefore, it is necessary to monitor the temperature of the SiPM. For this, a temperature sensor is soldered close to the SiPM and is read out by MicroDAQ. The temperature is converted to Kelvin on MicroDAQ and sent digitally to the central DAQ upon request.

To convert the raw values from the temperature sensor to Kelvin, MicroDAQ uses an extrapolated fit. All raw values given in the data sheet in the range $0\,^{\circ}\mathrm{C}$ to $-50\,^{\circ}\mathrm{C}$ are fit with a linear fit and then this fit was extrapolated down to $-70\,^{\circ}\mathrm{C}$. In order to verify the validity of the extrapolation used in the current firmware, the temperature sensor was connected to a MicroDAQ and both put into a temperature chamber. The temperature of the temperature chamber was compared with the temperature measured

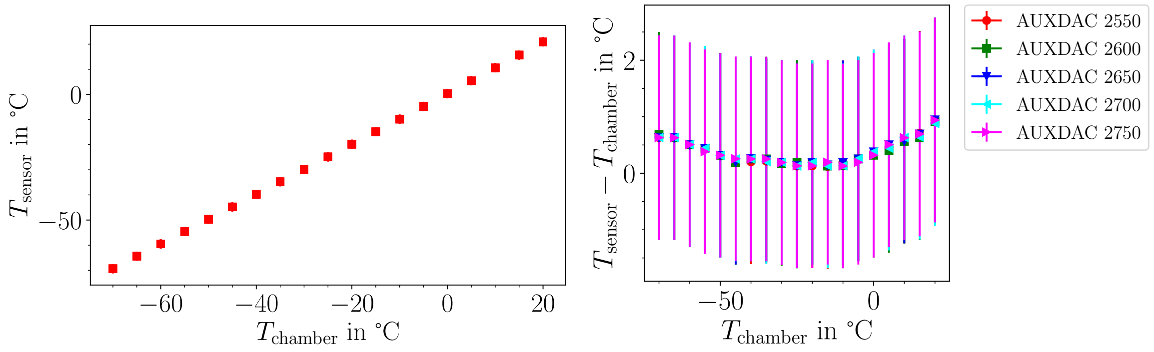

(a) **(b)**

Figure 7.1: Calibration of the temperature sensor close to the SiPM. In a) the temperature measured by the temperature sensor is plotted as a function of the temperature of the temperature chamber. The differences are shown in b) for different SiPM supply voltages (AUXDAC). The temperatures agree within the uncertainty of the temperature sensor of ±1.8 °C. Pictures modified from [Nuh21].

by the temperature sensor and converted to Kelvin by MicroDAQ in the range of 20 °C to −70 °C in 5 °C steps. The measurement was done in the scope of the Bachelor's thesis of Ömer Nuhoğlu [Nuh21] and the results are shown in figure 7.1. According to the data sheet, the temperature sensor has an uncertainty of ±1.8 °C [Tex13] and the temperatures agree within this uncertainty. However, as can be seen in figure 7.1, this is a conservative limit from the manufacturer and the measured values agree with higher precision. It can be concluded that the temperature sensor, its readout and the conversion to Kelvin work and can be taken as reference temperature of the SIPM, especially for measurements at the South Pole.

SiPM supply voltage The SiPM supply voltage is set using the command AUXDAC. The parameter range is 0-4095, since a 12-bit DAC is used internally. The mapping of the AUXDAC command to the SiPM supply voltage is shown in figure 7.2a). According to the producer Hamamatsu, the recommended SiPM supply voltage is at 5 V overvoltage, so at ≈ 58 V. Hence, the AUXDAC command has a linear behavior in the voltage range, in which the SiPM is operated. Only for very low and high values of AUXDAC, divergences from the linear behavior can be observed. These are due to the characteristics of the used DAC.

To check, if the SiPM supply voltage has a temperature dependency, the AUXDAC range used for measurements at the South Pole, AUXDAC 2550 to AUXDAC 2750, was measured at different temperatures. In case of a temperature dependency, this dependency would show up in the further analyses, e. g. figure 7.17 and would therefore need to be included in the interpretation of the data. To cover both, measurement in the laboratory and at South Pole, a temperature range of 20 °C to −70 °C was chosen. The temperature dependent measurements were performed by Ömer Nuhoğlu [Nuh21]. The result is shown in figure 7.2b). The SiPM supply voltage is mostly independent

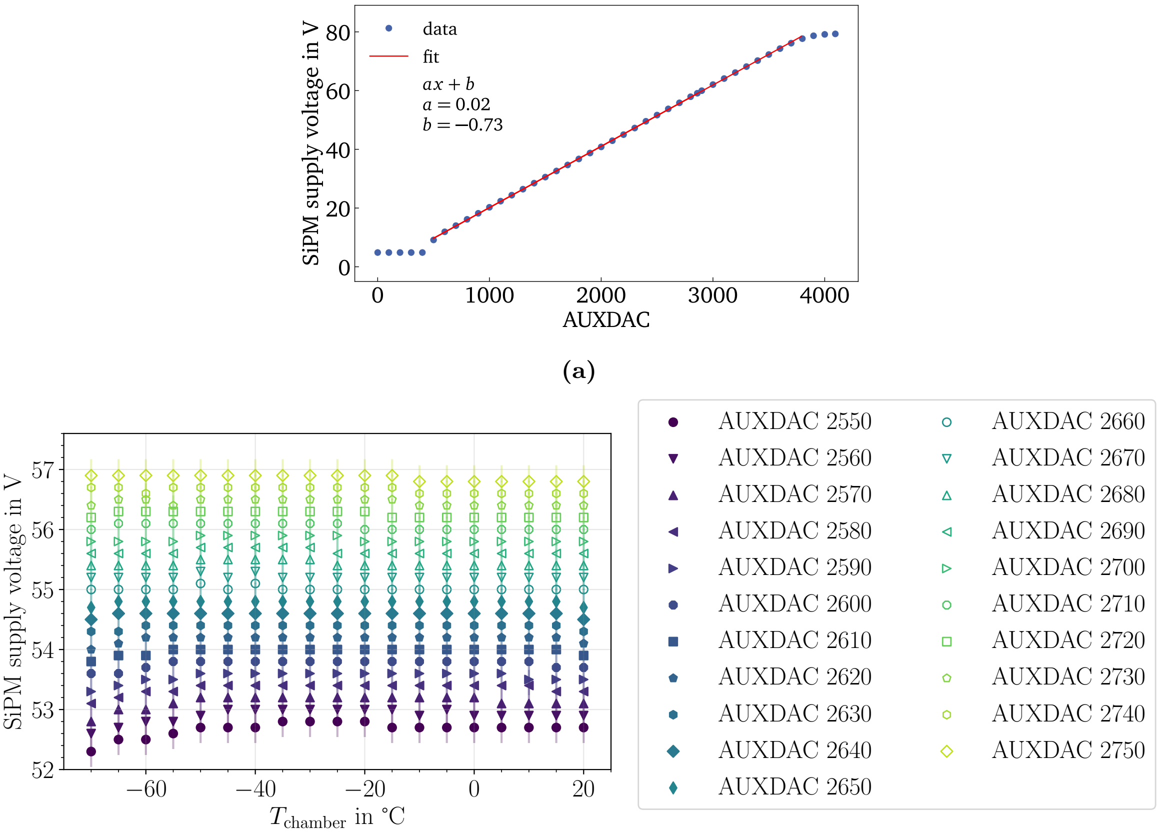

(a)

(b)

Figure 7.2: The mapping of the AUXDAC command to the SiPM supply voltage is shown in a). The non-linearity for very low and high AUXDAC values is expected due to the DAC. b) shows that the SiPM voltage as a function of the AUXDAC setting is almost independent of temperature for the AUXDAC region used for measurements at the South Pole. b) modified from [Nuh21].

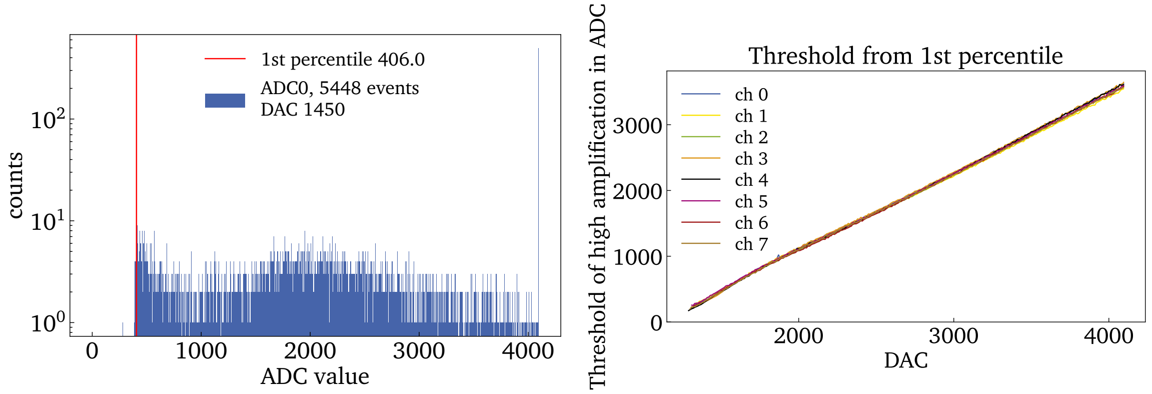

(a) **(b)**

Figure 7.3: Mapping of the DAC command to the threshold given in units of ADC for the high amplification. In a) a histogram of all measured hits of the measurement with DAC 1450 are shown. The value in ADC units, which corresponds to the setting DAC 1450, is evaluated from the 1st percentile of the measured hits and is marked in red. The data is from the threshold scan done on March 24, 2021. b) shows that the mapping of the DAC command to the threshold is almost identical for all scintillation detectors.

of the temperature. Only for temperatures below $\approx -50\,^\circ$C and for voltages below $\approx 54\,$V a slight deviation is visible. Since voltages above 54 V are used for hitbuffer measurements, no deviation is expected in the further analyses, which would need to be corrected.

Threshold The threshold for triggering the readout of hits is set on MicroDAQ using the command DAC. The parameter range is 0-4095, since a 12-bit DAC is used. To set the threshold correctly, it is necessary to know which value of the DAC parameter corresponds to which value in ADC units, because the measurement data is recorded in ADC units.

To map the parameters of the DAC command to a trigger threshold in ADC units, the data from the threshold scan performed on March 24, 2021 is used, cf. chapter 7.1.2. The threshold in ADC units is evaluated from the 1st percentile of the measured hits, see figure 7.3a). The result is shown in figure 7.3b). A linear behavior is observed and all channels show almost identical results. The threshold can be set between approximately 245 ADC and 3560 ADC of the high amplification. This means that the trigger threshold can be set in the range of very roughly 0 MIP to 2.5 MIP, depending on temperature and SiPM supply voltage.

7.1.2 Threshold scan of the scintillation detectors

A threshold scan of the scintillation detectors at South Pole was performed on March 24, 2021. A trigger threshold was set on MicroDAQ and then a hitbuffer measurement

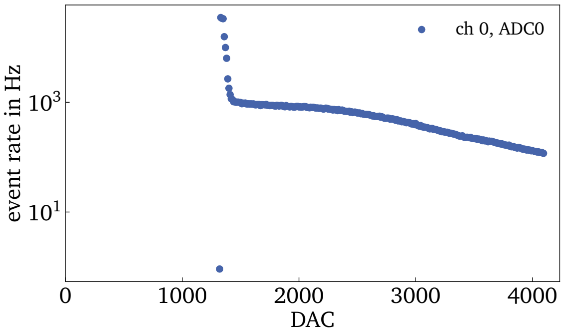

(a)

Figure 7.4: Hit rate as a function of the threshold DAC from the threshold scan on March 24, 2021. No hits are measured when the threshold is below the baseline, because the signals do not cross the baseline. When the threshold is in or slightly above the baseline, the readout is triggered almost constantly and is mainly limited by the dead time. In this case, noise can also trigger the readout. When the threshold is far above the baseline, the hit rate decreases as expected, because the higher the threshold, the higher needs to be the amplitude of the SiPM signal to trigger the readout, which only happens for MIP hits.

was performed with a runtime of 110 s. From the hitbuffer files, the hit rate is evaluated. This was repeated for the entire threshold range and for all scintillation detectors. The hit rate as a function of the threshold is shown in figure 7.4. No hits are recorded, when the trigger threshold is below the baseline, because the trigger threshold is not crossed. The readout of hits is triggered almost constantly, when the trigger threshold is in or slightly above the baseline of the SiPM. This leads to very high hit rates at approximately DAC 1300, which are primarily triggered by noise and are mainly limited by the dead time. When the trigger threshold is set above the noise-level, only MIP hits trigger the readout and the rate stabilizes at ≈ 1000 Hz. This agrees with the expected rate from the MIP flux at the South Pole and the sensitive area of the scintillation detectors [Hub21]. For higher thresholds, fewer events deposit enough charge to trigger the readout, so the rate decreases. For the shown scintillation detectors, channel 0 and channel 4, the spread of the baseline decreased below 10 ADC on March 19, 2021, so these measurements were already taken in darkness, cf. chapter 7.1.3 and 7.1.4. The results for the shown detectors are almost identical, which shows the uniformity of the detectors. Also, the results are in good agreement with the measurements from the previous station [Hub21].

7.1.3 Influence of sunlight on the baseline during the austral summer

Knowing the baseline is necessary for choosing the correct measurement settings, e. g. the threshold, and for converting the measured hits from units of ADC to MIP. The baseline is evaluated from the CPU-triggered hits, so from software-triggered readouts approximately once per second. These CPU-triggered hits are saved together with the signal-over-threshold triggered hits into the hitbuffer file, flagging which data is CPU-triggered.

For the following plots, the hitbuffer file of each run with a runtime of 110 s is taken, then the CPU-triggered hits are selected and the mean and standard deviation of the CPU-triggered hits are calculated. The mean of the run is plotted as the marker, the standard deviation as the error bar. It was expected that the baselines are stable within a few ADC units. However, while channel 1 and channel 7 show the expected baseline stability, drifts of the baseline spanning more than 1000 ADC units were observed for other channels, see figure 7.5.

After ruling out all other possible causes, which are described below, it was finally concluded that the baseline drifts are caused by light leaks in the scintillation detectors. For many days, the peaks in the baseline show a periodicity of one day. Once a day, when the sunlight hits exactly the leak, the sunlight leaks into the scintillation detector. This additional constant stream of photons gets transported to the SiPM and is read out, which leads to an overall elevated signal amplitude. So the CPU-triggered hits do not measure the baseline at zero photons, but instead at this increased amount of photons, which are constantly coming from the sun. When the sun moves across the horizon, the sunlight does not hit the leak exactly anymore, less photons leak into the scintillation detector and therefore the baseline decreases again. The argument for light leaks is further strengthened by the fact that the baselines are stable during the austral winter, see chapter 7.1.4.

To find the position of the light leaks in the scintillation detectors, the baseline drifts were further analyzed. The peaks in the baselines do not appear at the same time. For example the peaks of channel 2 and channel 3, which are neighboring scintillation detectors and thus at a 90° angle, have an offset of approx 6 h, see figure 7.6a). Correlating the peaks in the baseline with the direction of the sunlight shows that the peaks in the baseline always occur, when the sunlight hits the long side of the detector opposite to where the connector is. This is shown in the example of the neighboring detectors on channels 2 and 3 in figure 7.6b). For all detectors, see appendix C.

During the refurbishment of the scintillation detectors with the MicroDAQs, holes were found in the black foil, which is the light shielding of the detectors, see figure 7.7a). The holes were always at the edges of the wooden clamps, which fix the position of the scintillation bars. From the position and the state of the holes, it was concluded that the holes are probably torn in the foil, when the inner part of the detector is pushed into the housing. The found holes were fixed with additional foil and tape during the refurbishment, see figures 7.7b) and c). Concluding from the drifting baselines, the holes were either not fixed well enough, the fixed parts broke again or new holes were created during the refurbishment, transport or deployment of the scintillation detectors. To avoid the issue of light leaks in future detectors, the construction of the detectors was adjusted. The aluminum housing of the scintillation detectors, the wooden clamps

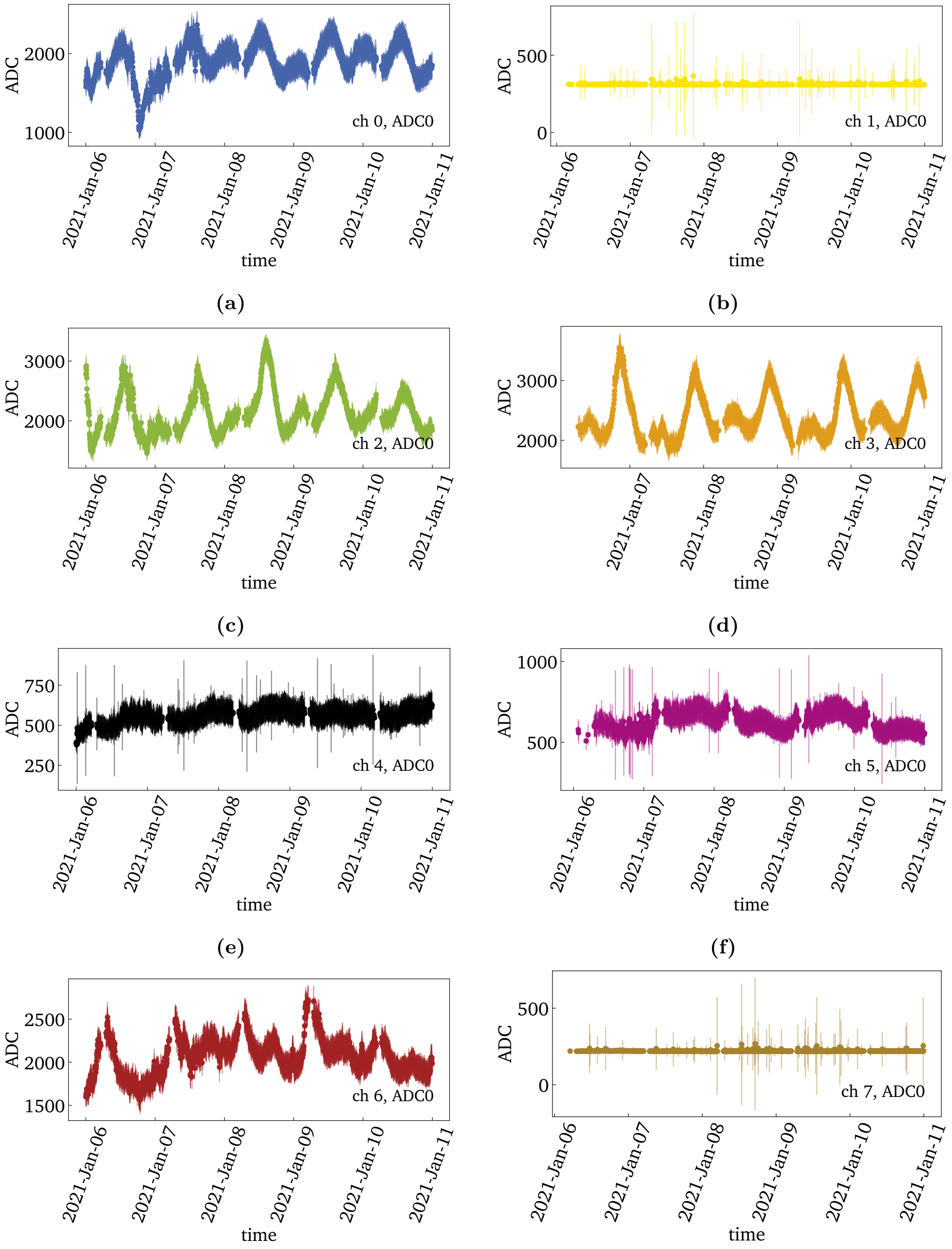

(a) **(b)**

(c) **(d)**

(e) **(f)**

(g) **(h)**

Figure 7.5: Baselines of scintillation detectors from January 6, 2021 until January 10, 2021. The marker is the mean of the CPU triggered hits of the high amplification of a run, the error bar is its standard deviation. The baselines of channel 1 and 7 show the expected constant baseline. The baselines of channels 0, 2, 3 and 6 drift drastically, channel 4 and 5 drift a bit. A daily pattern is visible.

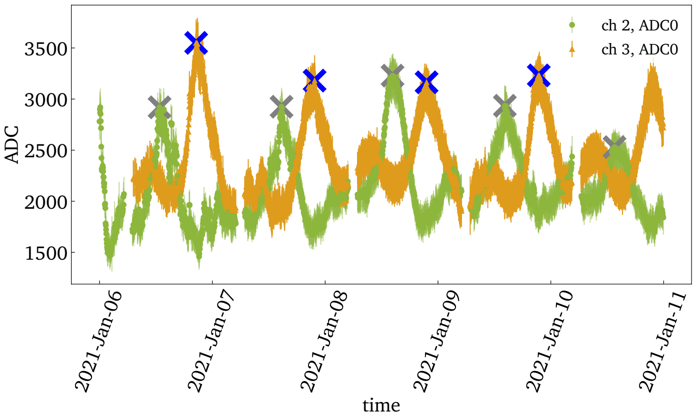

(a)

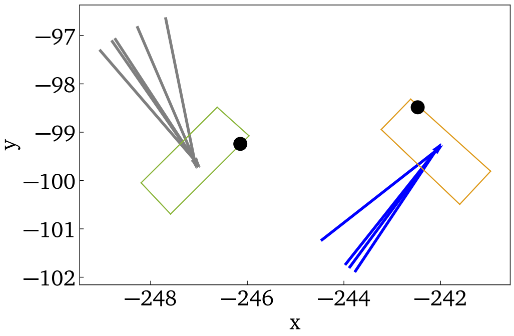

(b)

Figure 7.6: The comparison of the baselines of channel 2 and 3 is shown in a). The peaks of the baselines, marked as crosses, have an offset of $\approx 6\,\mathrm{h}$. The position of the sun at the point of the peaks is calculated. b) shows the position of the scintillation detectors as obtained from the GPS survey. The position of the connector is marked as a black circle. The direction of the sunlight, as calculated from the peaks in a), is indicated by the arrows pointing at the center of the respective scintillation detector. It is concluded that the peaks in the baseline appear, when the sunlight shines on the long side opposite the connector of the scintillation detector.

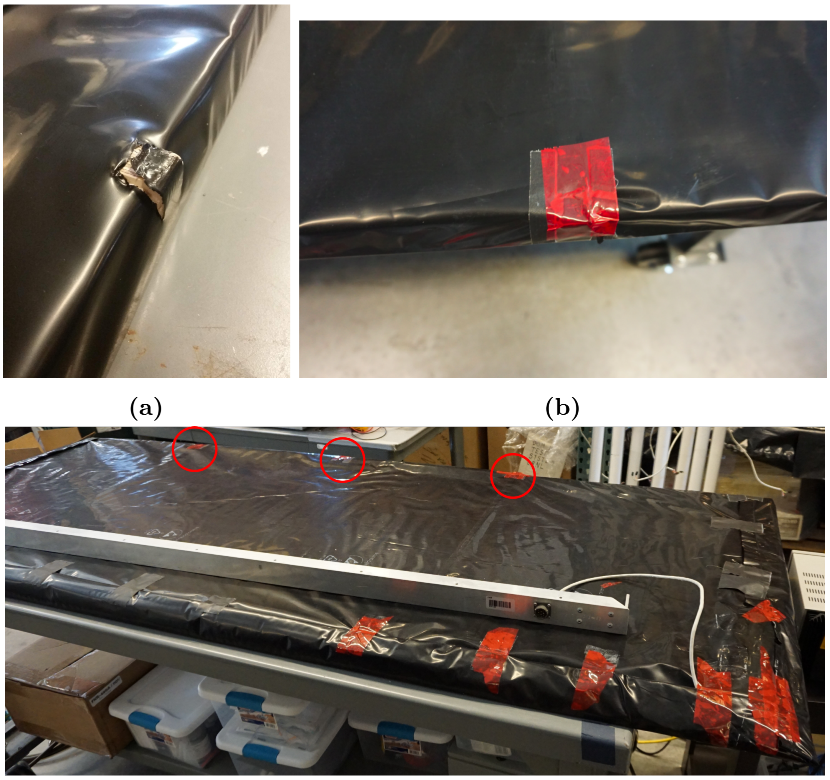

(a) (b)

(c)

Figure 7.7: A hole in the black foil is visible in a). The hole was probably torn by pushing the detector into the housing. To make the detector light-tight again, first some black foil was put into the hole and then everything was taped, first with a black tape and then additionally with a cold-resistant tape, see b). The fully fixed, light-tight detector is shown in c). The red circles mark the fixed holes. The connector with the white inner cable is on the opposite long side. Picture credit: a) photo by Matt Kauer, c) photo by Michael Riegel.

and the way the inner part of the detector is put into the housing were adapted.

Other possible causes of the drifting baselines were checked, which are described in the following, to avoid overlooking issues in the SAE prototype. External and hardware-related parameters were checked. No correlation between the baseline drifts and the temperature could be observed, neither the temperature measured by the temperature sensor close to the SiPM nor the temperature of the atmosphere measured by the meteorological station at the South Pole. The peaks in the baselines do not appear at the same time, so the drifts are not due to some machinery, which is turned on or off. The scintillation detectors are only configured once and the rest of the day only the commands to measure data, stop measuring data and send the data to the central DAQ are sent to MicroDAQ in a loop. So the baseline drifts are also not caused by configuring the scintillation detector, because then the baseline would be stable until the next reconfiguration. Since the measurements were always measured with the same SiPM supply voltage, the baseline drift is

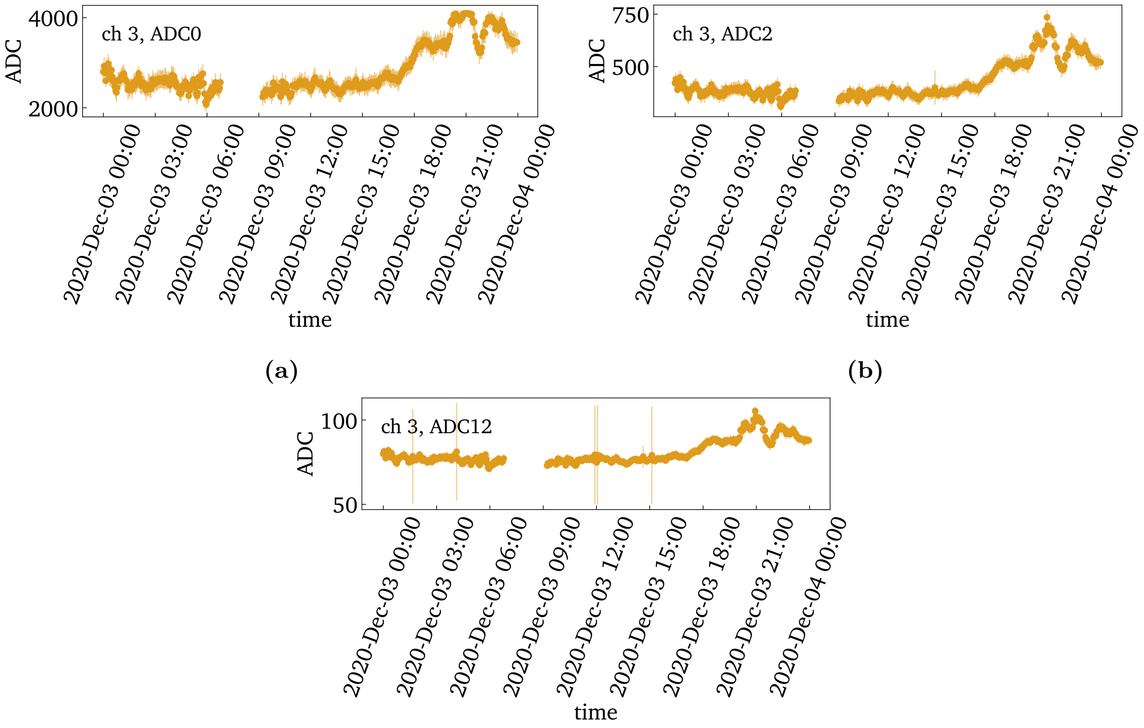

(a) **(b)**

(c)

Figure 7.8: The baselines of the three amplifications high a), medium b) and low c), show the same drifts. For ADC0, the baseline is so high that the 12-bit ADC is saturated. The gap around 6 a m is due to the histogram measurements. All amplifications respond together in lockstep. Therefore the drifts in the baseline is not due to ADC chips going bad, since each would deteriorate differently and therefore they would not show the same behavior.

not caused by a change in the SiPM supply voltage. Another theory was that the ADC chips deteriorate, which read out the charge of the hits. However, the baseline drifts can be observed in all three amplification channels and the drifts look identical considering the different amplification factors, see figure 7.8. Since not all ADC chips would get corrupted in exactly the same way, this theory could be negated.

Two other possible sources for the baseline drifts were an oscillation instability involving the discriminator and possible current leakage paths from the SiPM supply voltage into the front-end electronics of MicroDAQ. In case of the oscillation instability of the discriminator, the baseline drift would be independent of the SiPM supply voltage, but the hit rate plotted versus the threshold would show strange effects. If a current leakage from the SiPM supply voltage would cause the baseline drifts, the drifts would still be visible at a reduced SiPM supply voltage, although with a smaller amplitude, and only vanish for zero SiPM supply voltage. Therefore, to test both possibilities, threshold scans with different SiPM supply voltages were performed. The results for the threshold scan using the usual SiPM supply voltage of AUXDAC 2650 is shown in figure 7.9, using channel 3 as an example, because it showed the highest baseline drifts. The results for the threshold scan of channel 3 with half of the usual SiPM supply voltage and zero supply voltage can be found in figure 7.10. The results for all channels look as expected. No oscillation instability involving the discriminator could be observed; all jumps in the hit rate can be explained by the threshold being in or slightly above the baseline, leading to a very high hit rate. There is also no evidence for a conductive leakage, because the baselines were stable for both, AUXDAC 1350 and AUXDAC 0, and no baseline drifts could be observed. It can therefore be concluded that the baseline drifts were not caused by MicroDAQ.

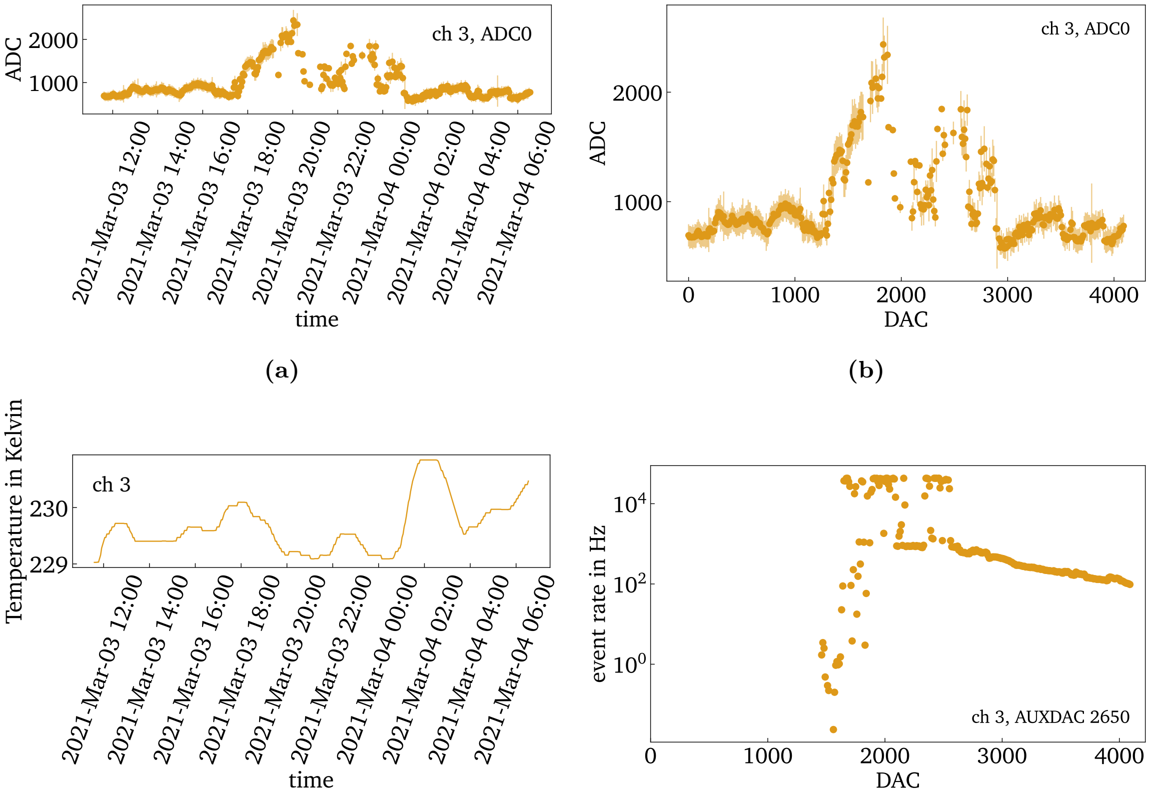

(a) **(b)**

(c) **(d)**

Figure 7.9: Results of the threshold scans for the usual SiPM supply voltage, AUXDAC 2650. AUXDAC 2650 is the voltage normally used for measurements. Channel 3 is plotted as an example, because it showed the highest baseline drifts. Since the threshold DAC was increased with time during the threshold scan, a) and b) show the same shape. Comparing a) and c) shows no correlation with temperature, especially since the temperature was very stable during the threshold scan. The hit rate in d) is evaluated from the hitbuffer files and looks as expected: When the threshold is below the baseline, the signals do not cross the baseline, therefore no hits are measured. When the threshold is in or slightly above the baseline, the readout is almost constantly triggered, leading to a very high hit rate, see e. g. DAC ≈ 1900. For very high thresholds, the hit rate shows the expected decrease.

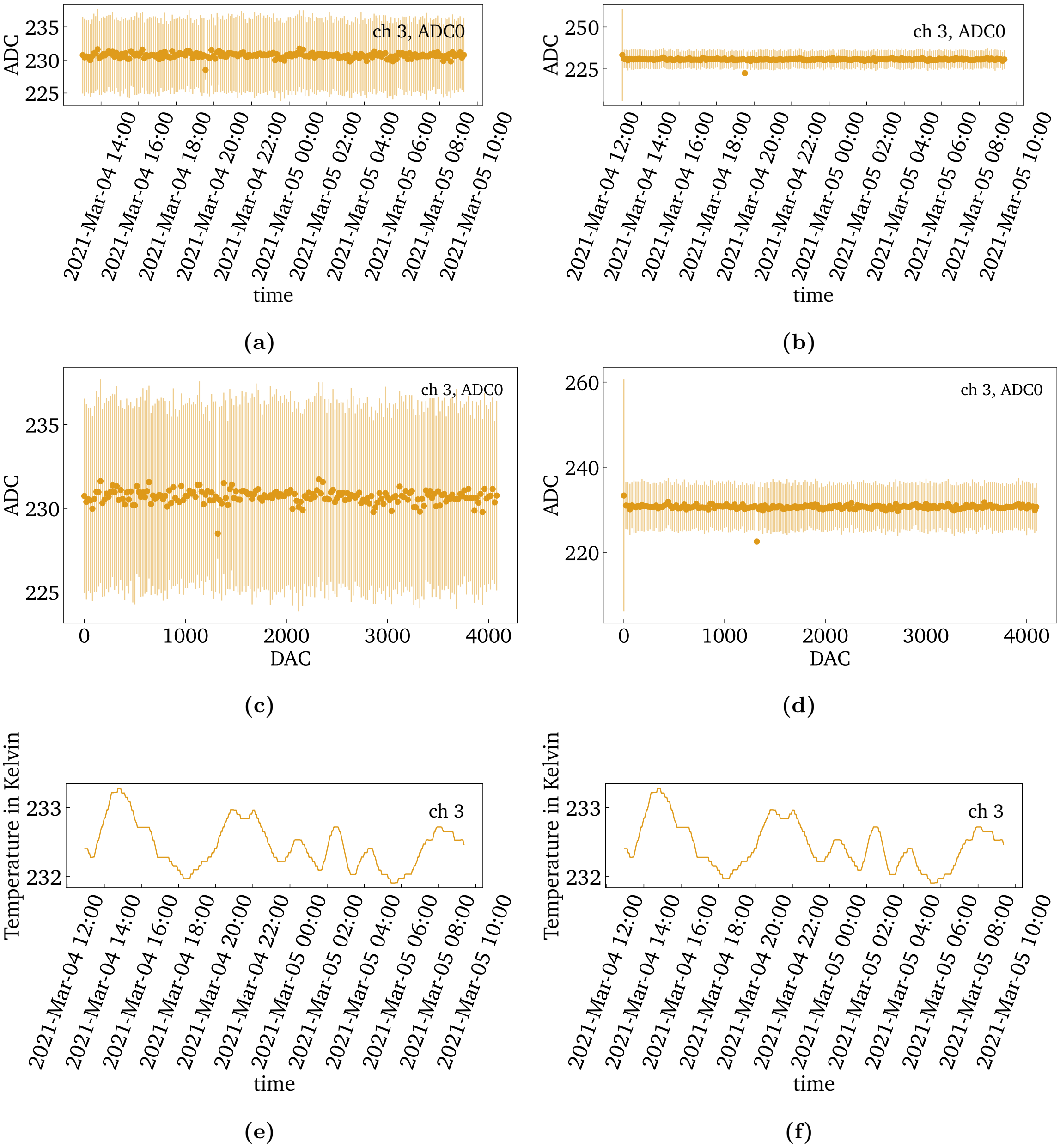

Figure 7.10: Results of the threshold scans for half and zero SiPM supply voltage. The results for half of the usual voltage, AUXDAC 1350, are shown in a), c) and e) and the results for zero voltage, AUXDAC 0, in b), d), f). The baselines do not show the drifts observed for the normal SiPM supply voltage and are almost constant. Also, they look the same for half and zero voltage. Therefore the drifts are not caused by a current leakage from the SiPM supply voltage into the front end electronics, because then the drifts would still be visible at a reduced level for AUXDAC 1350.

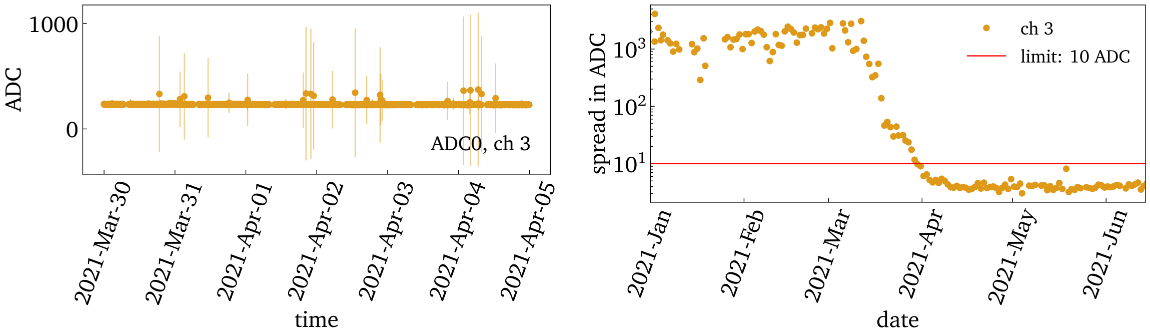

Figure 7.11: Baseline of channel 3 during austral winter and spread of the baseline over time. As can be seen in a), the baselines are stable during austral winter. The outliers towards higher ADC units are caused when by chance a MIP hits the detector while the baseline is being measured. The spread of the baseline is defined as the difference of the 95th percentile and the minimum. It is visible in b) that the spread decreases with the daylight. When the spread decreases below 10 ADC units, the measurements are defined as taken in the dark.

7.1.4 Baseline stability during the austral winter

With fading sunlight, the baseline drifts decreased, until they were stable in the darkness of the austral winter. The stability of the baseline is important, because the threshold can be set to a reasonable value. This improves the quality of the data.

The mean of the CPU-triggered hits of a single measurement is taken as its baseline. An example for a baseline in austral winter is shown in figure 7.11a) for channel 3, which had the highest baseline drifts during austral summer. The mean of the CPU-triggered hits is plotted as the marker and the standard deviation as the error bar for each run. The outliers towards higher ADC are caused by MIPs crossing the detector during the measurement of the baseline by chance.

To exclude the MIP-caused outliers, only the 95th percentile of each day is considered. The spread of the baseline on this day is defined as the difference between the minimum and maximum of this subset. As can be seen in figure 7.11b), the spread drops significantly with the decreasing light. When the spread drops below 10 ADC units, the measurement is defined as measured in darkness. Channel 3 was the last to drop below this limit on March 30, 2021, see figure 7.11b). Therefore all physics-related analyses are done with data after March 30, 2021 to avoid data corruption due to the light leaks.

7.1.5 Timing of the scintillation detectors

The timing of the scintillation detectors is important for air-shower analyses, because the direction of the shower is calculated from the timestamps. Therefore, if the timing is not correct, the wrong direction is reconstructed. The timing is distributed from the central DAQ to the scintillation detectors. Due to the propagation of the signal in the cables, a delay is added and the exact cable delay is unknown. If the delay by the cables is not identical for all scintillation detectors, the timing of the detectors would be asynchronous, which would impair the reconstruction.

To determine the cable delays, air-showers are used, which fulfill the following criteria:

- The air-shower was measured by all eight scintillation detectors within 1 µs.
- The charge measured by each scintillation detector is above 1 MIP.
- The air-shower was measured by IceTop.
- The reconstructed zenith angle θ from the IceTop reconstruction, called Laputop, is below 15°, so only vertical showers.
- The distance between core position determined by Laputop and the center of the SAE prototype is below 100 m.

This gives a total of 804 events. Since IceTop is a well studied and calibrated detector [Abb+13], it is taken as reference to calculate the expected timestamps for the scintillation detectors, using a plane front approximation. Ideally, the differences between the expected and the measured timestamps are only due to the curvature of the shower front, which can be described by

$$\Delta t = ar^2 + b \tag{7.1}$$

according to the studies in [Les21]. In case of a cable delay relative to the other detectors, the mean of the residuals for all events for this scintillation detector is approximately the cable delay. Therefore, the cable delay can be determined iteratively by fitting the shower front with equation 7.1 and calculating the mean of the residuals. The value of the mean of the residuals is subtracted from the Δt for each detector and then the process is repeated until it converges. The obtained cable delays can be found in appendix D. All data shown in this thesis is corrected with these cable delays.

To check the distribution of the timing to the eight scintillation detectors, the time difference between the neighboring panels is evaluated. For this, only air-shower data measured in the dark was used and only when all 8 scintillation detectors recorded a hit within 1 µs. The result is shown in figure 7.12. As expected, the mean time difference between neighboring scintillation detectors is negligible, considering the time resolution of the scintillation detectors. The standard deviation of ≈ 20 ns is expected due to the layout of the station, in which the centers of the scintillation detectors are ≈ 5 m apart and due to propagation effects in the scintillation detectors [Ice19a]. This information and other checks show that the timing distribution to the scintillation detectors works.

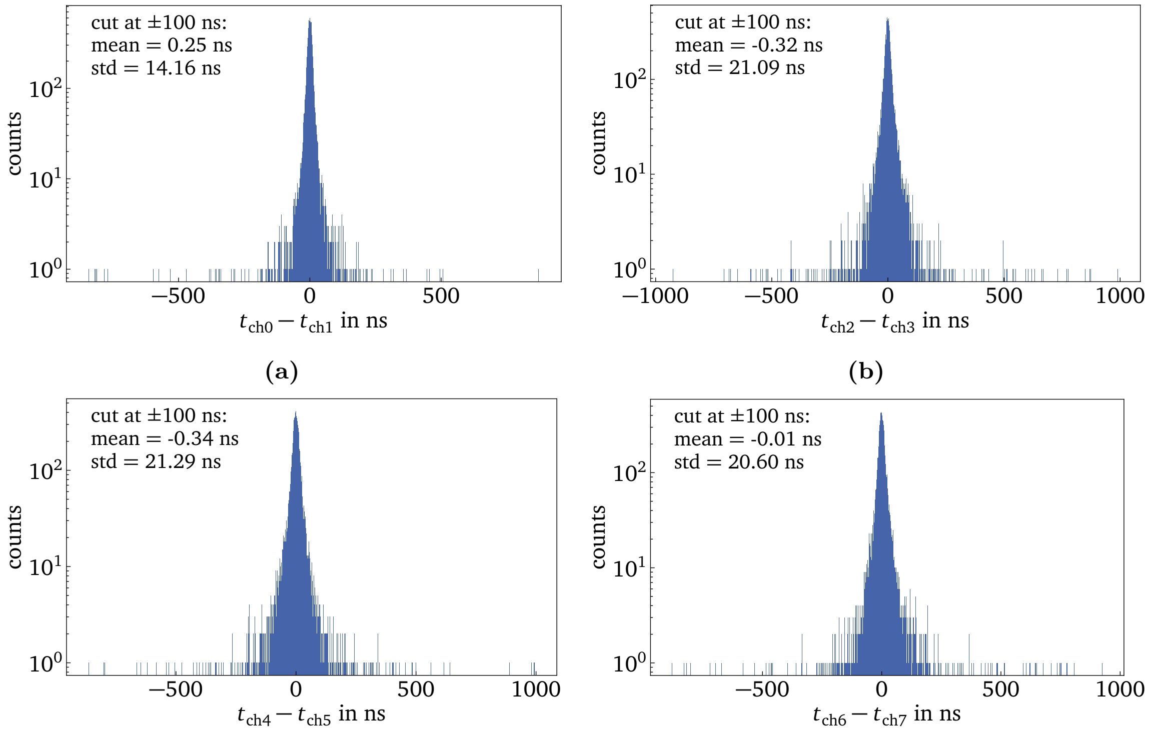

(a) **(b)**

(c) **(d)**

Figure 7.12: Time difference between the hits in neighboring panels. Only events with 8 coincident hits in the scintillation detectors with a threshold of ≈ 0.5 MIP in the dark, so between June 15, 2021 and July 28, 2021, were used. The standard deviation in the interval $-100\,\text{ns}$ to $100\,\text{ns}$ is $\approx 20\,\text{ns}$. This deviation is expected, since centers of the panels are $\approx 5\,\text{m}$ apart and the panels are at 90° to each other and uncorrelated noise can trigger single detectors at this threshold.

7.1.6 Determination of the dead time

In order to measure air showers and to serve successfully as a veto for the in-ice detector, the dead time of the scintillation detectors needs to be evaluated. For the veto, the dead time should be as small as possible to minimize the number of missed events. For air-shower measurements, for example the systematic uncertainty of measured event rates increases with the dead time of the detectors.

To check the internal dead time of MicroDAQ, the time differences between consecutive events is evaluated. A histogram of the time differences for channel 0 for one day is shown in figure 7.13. In figure 7.13a) all recorded time differences are shown. The expected exponential decay for larger time differences is visible. A zoom-in on the small time differences can be seen in b), with a clearly visible cut-off at $\approx$ 22.6 µs. This cut-off is constant for most days, as can be seen in c). Some outliers towards smaller time differences are visible. All outliers have been checked and all are caused by a single hit with a smaller time difference to the next hit. An example for this is shown in d). These are probably caused by glitches in the timestamp. Since these glitches in the timestamps occur very rarely, in average less than once a month, they are not taken into account in the further analyses.

To crosscheck this, the dead time is also evaluated from the hit rate. When the threshold is in the baseline, the hit rate is mainly limited by the dead time of the scintillation detector. In the threshold scan on March 24, 2021 is the maximum hit rate for channel 0 is $\approx 3.7 \times 10^4$ Hz, so in average every 27 µs an hit is measured. This is consistent with a dead time of 22.6 µs.

The dead time of 22.6 µs is composed as follows: $\approx$ 12 µs are needed to transfer the data from the ADC chips into the microprocessor and $\approx$ 10 µs are necessary for processing the data after it is received in the microprocessor and to reset the trigger. Since for the measurements analyzed in this thesis only three ADCs were used, a new MicroDAQ firmware could be written that is optimized to read out only these ADCs in parallel. That could reduce the time to transfer the data from the ADC chips to the microprocessor from $\approx$ 12 µs to $\approx$ 3 µs [Wen]. However, such a firmware would restrict the capabilities of MicroDAQ and studies of the arrival time profile and sampling delay times above 100 ns would not be possible.

An air-shower has a thickness of $\mathcal{O}(10\,\mathrm{ns})$ [KW12]. Therefore, with a dead time of 22.6 µs, an air shower is measured once. With the rate measured in the threshold scan of 1 kHz, cf. chapter 7.1.2, the dead time probability of a scintillation detector is 2.26 %. This dead time probability is comparable to that of a single IceTop tank, referred to as SLC mode [Abb+13].

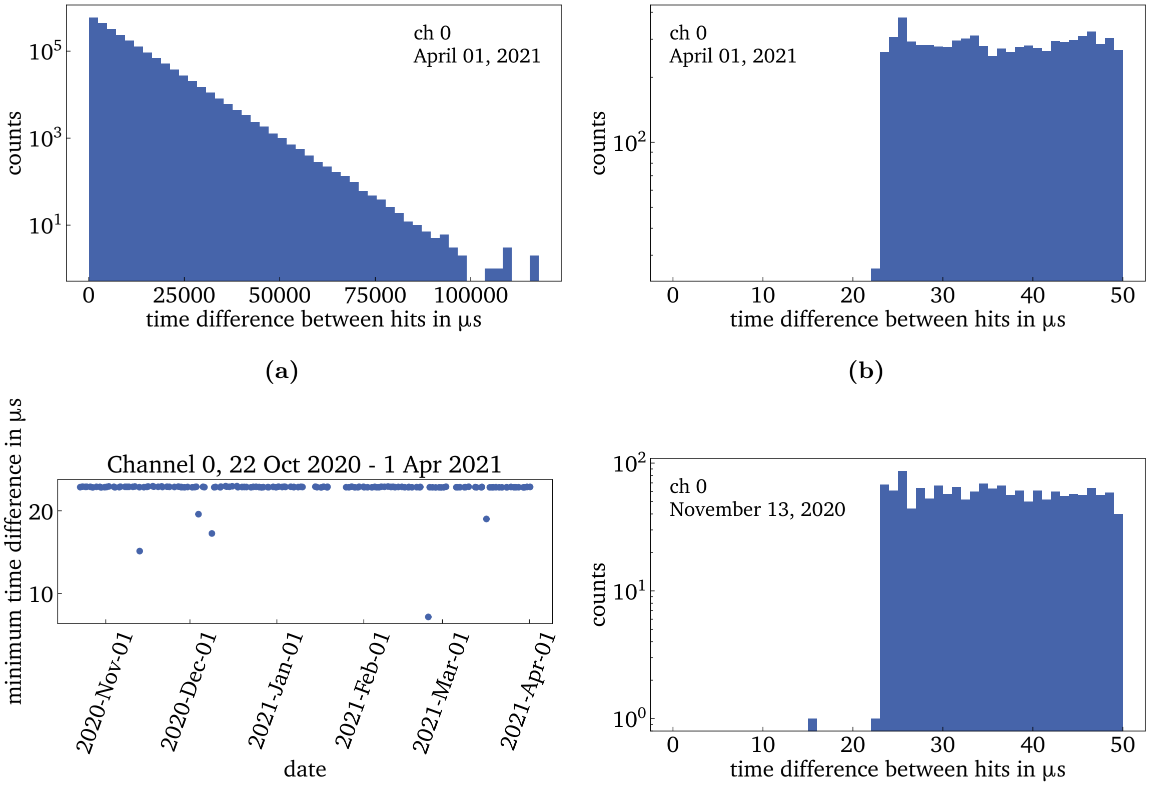

(a)

(b)

(c)

(d)

Figure 7.13: Determination of the dead time of MicroDAQ. In (a) the histogram of the time difference between consecutive hits is plotted on the example of the day April 1, 2021. (b) shows the same for small time differences only. The cut-off at $\approx 22.6\,\mu s$ is visible. The minimum time difference per channel and day is shown in (c), on the example of channel 0. Usually, it is at $\approx 22.6\,\mu s$. The minimum time difference is lower for single days. These lower values always correspond to one single hit, as can be seen in (d), which is probably caused by a glitch in the timestamp.

7.1.7 Gain and MIP light yield from charge histograms

The evaluation of the MIP light yield is important, because one of the reference units used in air-shower physics is MIP and the reconstruction algorithms used in chapter 8 use number of MIPs as the input parameters. The position of a single MIP in a measured charge spectrum depends on SiPM characteristics. Since the gain of the SiPM is temperature dependent, the position of the MIP shifts accordingly. This effect needs to be corrected for. Therefore, the gain of the SiPM and the MIP light yield is evaluated.

To get both, the SiPM gain and the MIP light yield, measured charge histograms are used. An example is shown in figure 7.14 for all amplifications. The baseline of the SiPM is recorded via software-triggered readouts once per second. This is visible as the peak at very low ADC units, called the pedestal. To determine the position of the pedestal, it is fit with a Gaussian.

Directly above the pedestal, no hits are recorded, because the threshold is set slightly above the baseline to reduce the measured noise, cf. chapter 7.1.2. Then, at low ADC units, the exponential dark noise component is visible. For the high amplification, the single Photo Electron Equivalent (P.E.) peaks on top of the dark noise component can be discerned. Then a valley is visible at $\approx 850\,\text{ADC}$ units and the MIP peak at $\approx 1600\,\text{ADC}$ units in a). The pedestal, the exponential dark noise, the valley and the MIP peak are visible for all amplifications, with the positions shifted according to the lower amplification. According to [Hub21], the optimal fit function for the whole spectrum is a Landau+exp()+exp() function. However, this was numerically not stable enough for the analyses in this thesis. Therefore the position of the MIP peak is evaluated by fitting a Gaussian function, as is described in [Ice19c].

The gain of the SiPM can be measured with MicroDAQ in-situ at South Pole using the high amplification channel of MicroDAQ. The single P.E. peaks in the histogram of the high amplification correspond to a certain number of fired SiPM pixels, so if a single P.E. peak corresponds n detected photons, the next one corresponds to $n + 1$ detected photons and so on. If the threshold is set at n single P.E., MicroDAQ will measure a charge spectrum including all P.E. peaks $\geq n$. For high numbers of detected photons, the peaks smear out due to statistical fluctuations and noise [Gar20]. Therefore, the threshold is set low enough that the single P.E. peaks are measured. From the distance between the single P.E. peaks in the charge histogram, the SiPM gain is evaluated.

To determine the gain, two methods are used:

a) The positions of the single P.E. peaks are evaluated by fitting a Gaussian to each peak. The distance between these peaks, and thus the SiPM gain, was calculated from the difference of the mean μ of the Gaussians, see figure 7.15a).

b) The distance between the single P.E. peaks is evaluated from the Fast Fourier Transform (FFT) of the part of the charge histogram containing the single P.E. peaks, as described in [Ice19c]. The charge spectrum with the single P.E. peaks

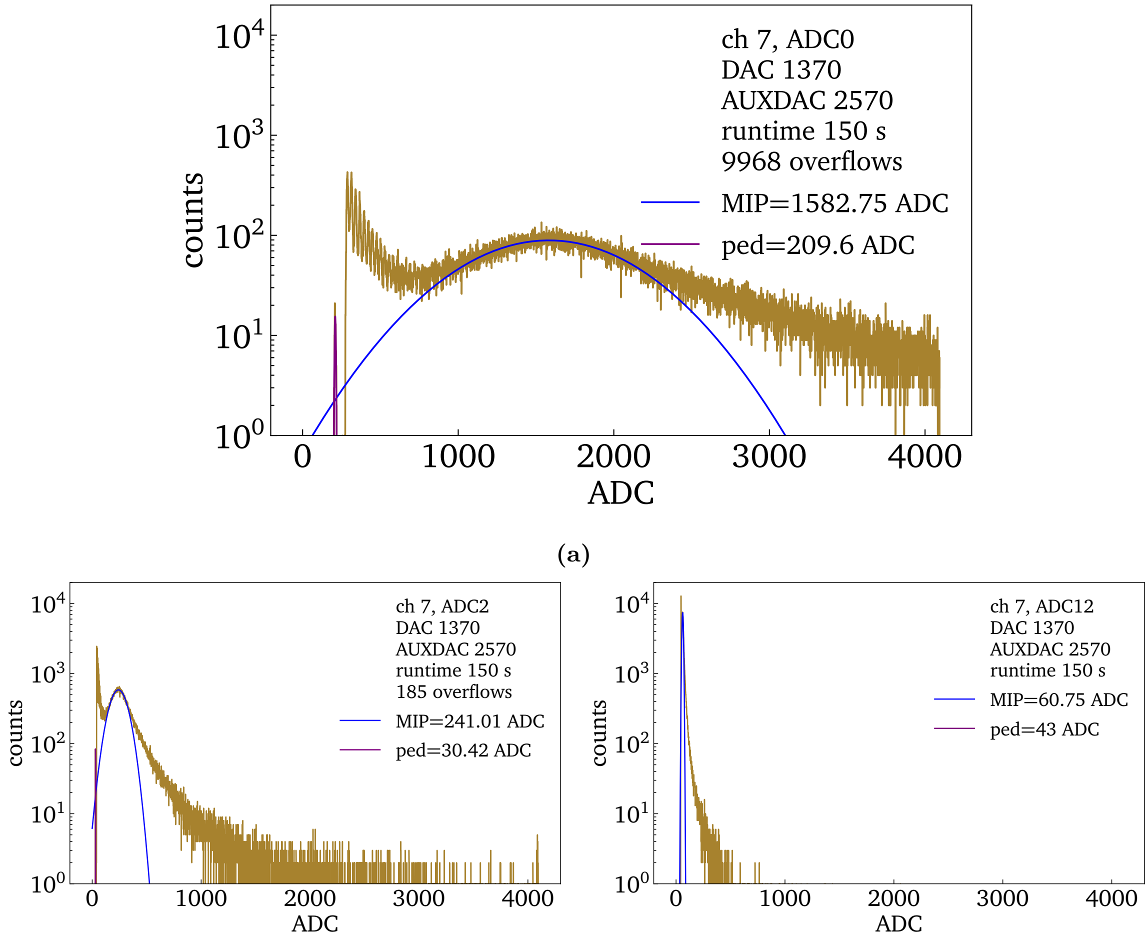

(a)

(b)

(c)

Figure 7.14: Charge histogram of channel 7 for high a), medium b) and low amplification c). The peak at low ADC values from the baseline and called the pedestal. The exponential dark noise component and the single p.e. peaks are visible until ≈ 650 ADC units in a). The peak at ≈ 1600 ADC units in a) is the MIP peak. The positions of the pedestal and the MIP peak are determined by Gaussian fits for all amplifications.

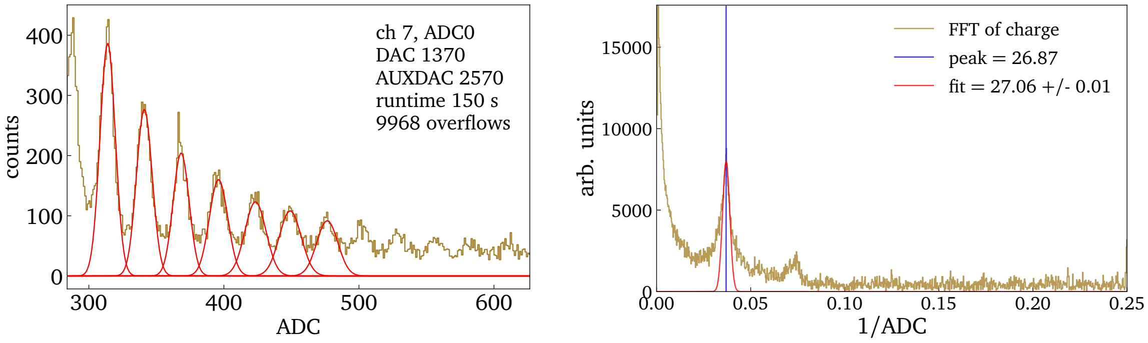

(a) **(b)**

Figure 7.15: Evaluation of the gain from Gaussian fits to the single p.e. peaks in a) and using the FFT of the left side of the histogram in b). A Gaussian is fitted to the peak in the FFT.

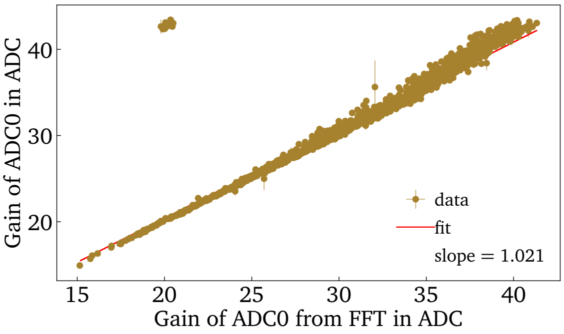

Figure 7.16: Comparison of the gain evaluated from fits to the single p.e. peaks and evaluated from the FFT. The outliers at $\approx 20\,\mathrm{ADC}$ for the gain from FFT are caused when the FFT fits the first harmonic instead of the fundamental peak, The results of both methods agree reasonably well. The linear regression has a slope of 1.021, so the methods only differ on the 2 % level.

corresponds to a sine wave in frequency space. After fitting the peak in the Fourier transform, see figure 7.15b), it is transformed back.

Both methods work and give almost the same result. The results differ on a 2 % level, see figure 7.16. However, method b) sometimes fits the first harmonic instead of the fundamental, which leads to the visible outliers. Therefore, the gain evaluated with method a) is used in this thesis.

To characterize the scintillation detectors and the incorporated SiPMs, the histogram measurements are repeated every day at the South Pole with several SiPM supply voltages (AUXDAC 2550 - 2750). Since the temperature changes during the year, a characterization for the full temperature range at South Pole is done. The SiPM gain is obtained as a function of the SiPM supply voltage and the temperature, see figure 7.17. Since the breakdown voltage of the SiPM decreases approximately linearly with the temperature, the gain increases linearly with temperature and overvoltage [Ott+17;

Gar20]. Therefore, a plane fit is performed. As can be seen from the distribution of the residuals in figure 7.17c), the fit describes the data well. The characterization of the SiPM gain as a function of bias voltage and temperature can be used to adjust the bias voltage of the SiPM according to the observed temperature changes, in order to keep the gain constant, see chapter 7.1.8.

The light yield, so the MIP in P.E., is evaluated from the measured histograms. The pedestal is subtracted from the position of the MIP peak in ADC units and divided by the gain,

$$\alpha = \frac{\mathrm{MIP} - \mathrm{pedestal}}{\mathrm{gain}}. \tag{7.2}$$

When plotting the MIP in P.E. as a function of the SiPM supply voltage and the temperature, another linear dependence is observed, see figure 7.17b). The linear dependence is probably due to the approximation of the gain as linear, since the breakdown voltage does not decrease linearly for large temperature ranges and the photon detection efficiency of the SiPM as a function of overvoltage is not linear [Col+11; CS66; Oeh18]. Another plane fit is done for the MIP in P.E. as a function of the SiPM supply voltage and the temperature. As can be seen from the residuals in figure 7.17d), the plane fit describes the data well.

All hits used in the analyses in this thesis are recorded in parallel with three different amplifications, so the same hits are contained in the histograms of the three amplifications. Since the gain can only be evaluated for the high amplification, the scaling factors between the three different amplifications are needed to convert the data to MIP, where MIP is the number of minimum ionizing particles. The scaling factors are determined from comparing the pedestal-corrected position of the MIP peak. A histogram of all obtained scaling factors is shown in figure 7.18. The inverse scaling factors relative to the high amplification are determined by Gaussian fits to the histogram.

With this information, all measured hits can be converted from ADC units to MIP. The temperature is taken from the monitoring files of the scintillation detectors. The SiPM supply voltage is taken from the log files. For the hitbuffer measurements analyzed in this thesis, the voltage is always AUXDAC 2650. With this, the gain and the number of P.E. per MIP α are obtained from the plane fits, see figure 7.17. For histogram measurements the baseline of the measurement is evaluated from the position of the pedestal, while for hitbuffer measurements the baseline is evaluated from the mean of the CPU-triggered hits. Then the conversion to units of MIP is done as follows for the high amplification,

$$\text{hit in MIP} = \frac{\text{hit in ADC} - \text{pedestal in ADC}}{\alpha \cdot \mathrm{gain}}. \tag{7.3}$$

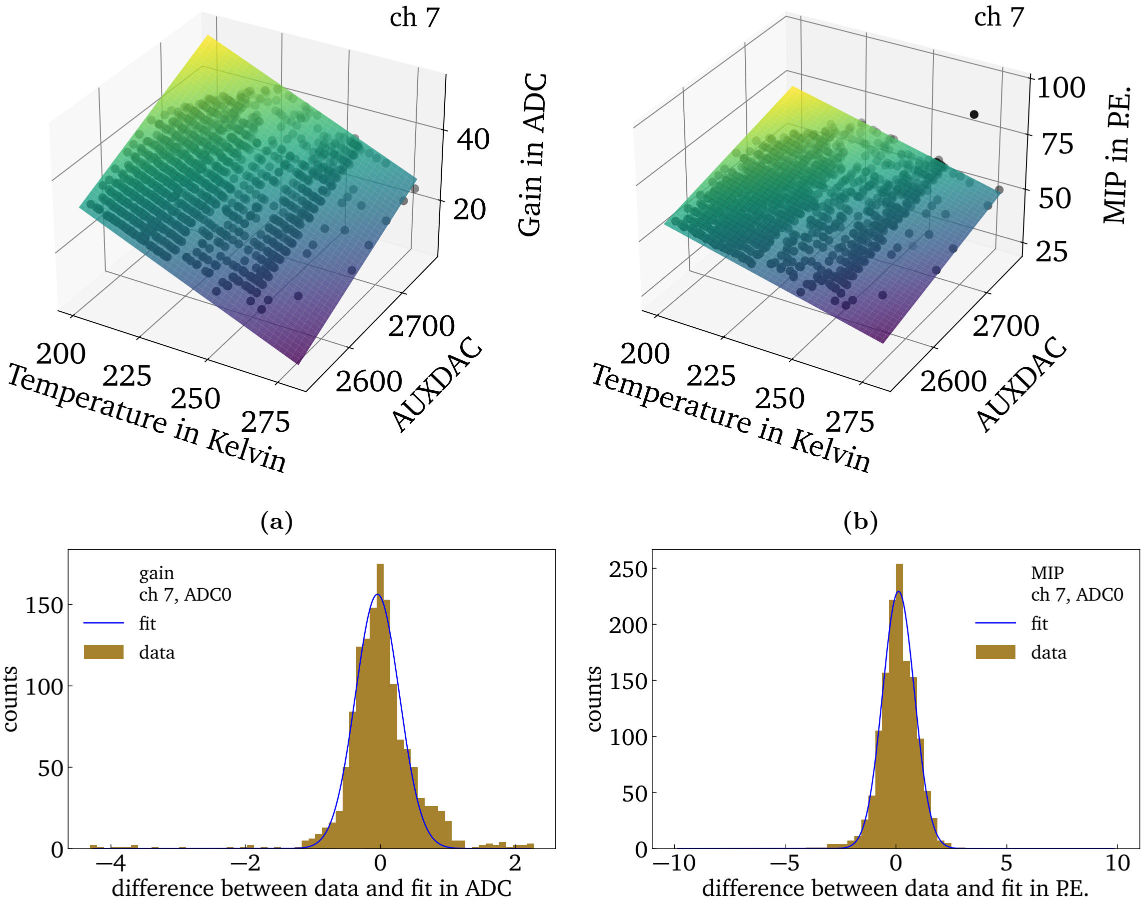

(a) **(b)**

(c) **(d)**

Figure 7.17: The gain and MIP dependence on the SiPM supply voltage and the temperature is shown in a) and b), respectively. A plane fit was applied to both. As can be seen from the histograms of the residuals in c) and d), this describes the data sufficiently well for the analyses performed in this thesis. A Gaussian is fitted to the residuals and the obtained variance is taken as the uncertainty of the gain and MIP, respectively.

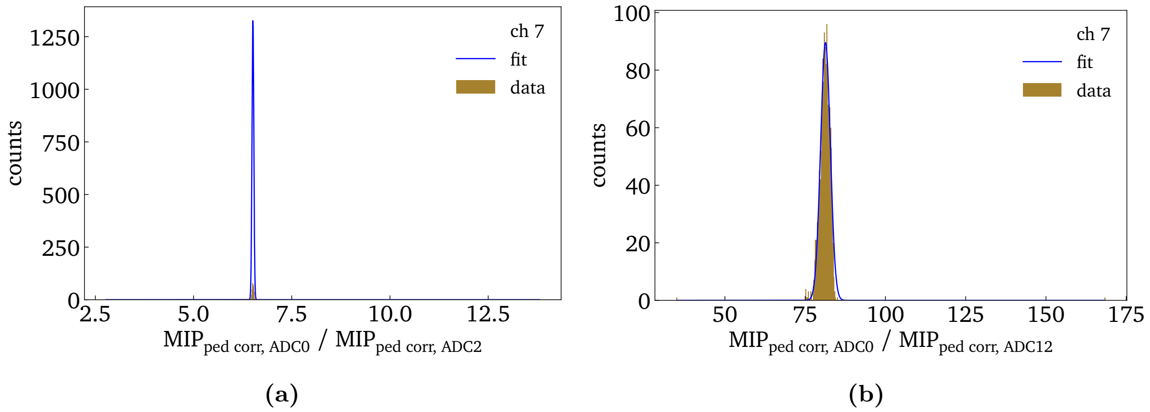

(a) (b)

Figure 7.18: The ratio of the amplifications is determined from the relative positon of the MIP peaks of the high and medium amplification channel a) and the high and low amplification channel b). The Gaussian fits lead to the inverse scaling factors relative to ADC0 of $A_{\mathrm{F,\ ADC2}} = 6.51 \pm 0.02$ for ADC2 and $A_{\mathrm{F,\ ADC12}} = 81.13 \pm 1.52$ for ADC12.

For the other amplfications, the inverse scaling factor has to be included, leading to

$$\text{hit in MIP} = \frac{\text{hit in ADC} - \text{pedestal in ADC}}{\alpha \cdot \text{gain} \cdot {}^{1}/_{\text{inverse scaling factor}}}. \qquad (7.4)$$

7.1.8 Temperature compensation

To mitigate temperature effects of the SiPM, it is planned to keep the SiPM gain constant. For this, the SiPM supply voltage is adjusted according to the temperature of the SiPM, using the plane fit in figure 7.17. This temperature compensation will be done internally on MicroDAQ, so without intervention of the central DAQ.

This is not implemented yet. For all hitbuffer measurements analyzed in this thesis, the SiPM supply voltage was constant and set to AUXDAC 2650. Therefore, the correction for the temperature effects is done in the data analysis, when the hits are converted from ADC units to MIP as described above. Since the SiPM gain and thus also the position of the MIP are not stabilized, the stability of these parameters over time cannot be checked.

7.1.9 Saturation

To increase the dynamic range, MicroDAQ has three amplifications: high, medium and low. The higher the amplification, the better the resolution due to the finer binning in MIP units. However, with increasing energy, events will first saturate the ADC reading out the high amplification, then the one for the medium amplification and finally the one for the low amplification. When the ADC is saturated, just a lower limit for the deposited charge in the detector can be given from this readout.

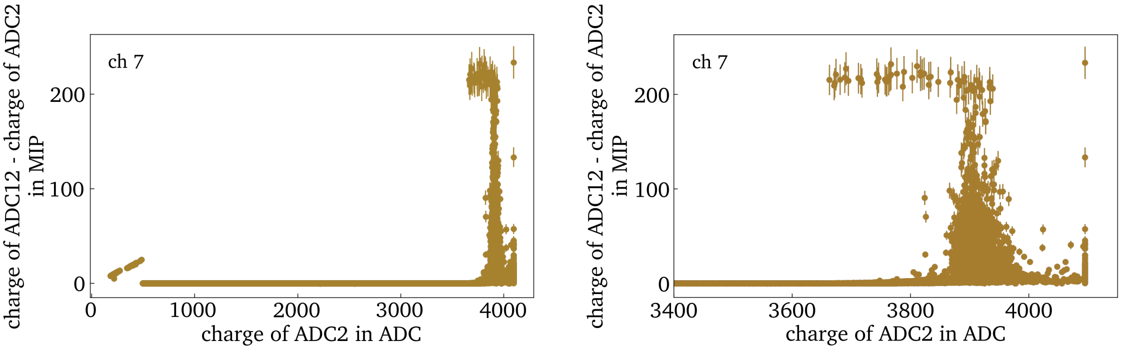

(a) **(b)**

Figure 7.19: Difference of the charge in units of MIP between low and medium amplification as a function of the charge in ADC units for the medium amplification. In a) the entire range is plotted. For almost the entire range, the difference between the charge measured by the amplifications is negligible. At around 3600 ADC units, the charge in MIP diverges. This is due to the saturation of the ADC.

Therefore, if an ADC has a value in the saturation range, the less amplified signal should be used for the evaluation. So if an event saturates the ADC reading out the high amplification, the medium amplification should be checked for saturation. If the ADC reading out the medium amplification is not saturated, this value is taken for the conversion to units of MIP. If it is also saturated, the low amplification is checked for saturation. For events that saturate the ADCs of all three amplifications, a flag that the detector was saturated, is added in the files containing the events in units of MIP.

According to the characteristics, the range of saturation of the ADC is not only the last ADC bin, but is an extended range of the last ADC units. In order to convert to units of MIP correctly, it is necessary to determine this saturated range. To obtain this range, the measured charges of all amplifications are converted to units of MIP and are compared. For the not-saturated range, the charges show only a negligible difference due to the different resolutions of the three amplifications. If an ADC is saturated, however, the charges deviate a lot. The difference of the measured charges in units of MIP between the medium and the low amplification are shown in figure 7.19. As expected, almost no deviation between the charges is visible for most ADC bins. The small deviations at very low ADC units are caused by statistical fluctuations of the baseline. A deviation is clearly visible for the high ADC bins, starting at ≈ 3600 ADC units. This is the range of saturation of the ADC. The same result is obtained when comparing the charges in units of MIP between the high and the medium amplification. This is expected, since identical ADCs are used for the readout of all amplifications. Therefore the saturated range encompasses the ADC bins 3600 to 4095. The limit, when the charge evaluated from a lower amplification is used, is set to 3600 ADC units.

To check, if the scintillation detectors measure events which saturate all amplifications, the measured events are plotted in a histogram. In case of saturation, a pileup in the

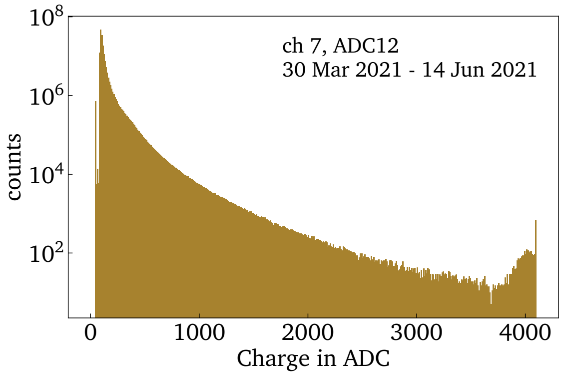

Figure 7.20: Histogram of the charge for low amplification from the hitbuffer measurements between March 30, 2021 and June 14, 2021. Above ≈ 3500 ADC units a pileup is visible. This indicates a saturation of the electronics for very high energy air-showers.

range of the high ADC units for the low amplification is expected. The histogram is shown in figure 7.20. A pileup above 3600 ADC units is clearly visible, indicating a not negligible amount of saturated events. The same behavior is observed for all scintillation detectors.

The number of MIPs, which can be measured with a scintillation detector without saturation depends on the temperature and the SiPM supply voltage. As a rough estimate, using the measured histograms with the current settings, a linear extrapolation is done. For the low amplification, the position of the pedestal is subtracted from the position of the MIP peak in ADC units, resulting in a mean of ≈ 19 ADC units per MIP. The position of the baseline is ≈ 200 ADC units. Since the used 12-bit ADCs have 4096 ADC bins, this results in a limit in the order of 200 MIP.

This linear extrapolation is only valid, if the SiPM is still in the linear regime for measuring the number of photons. Therefore, a rough estimate on the upper limit of the measured photons is done. The number of detected photons per MIP is below 75, cf. figure 7.17b). The ADCs saturate at ≈ 200 MIP for the low amplification. That leads to an upper limit on the number of detected photons of 15 000 photons. According to [Bre+17], this is still in the linear regime of the SiPM. This also means that no saturation effects of the SiPM occur and that only the electronics saturate.

Therefore, to increase the amount of MIP a scintillation detector can detect without saturation, the amplification of the SiPM signals can be reduced. This will extend the range measurable with the low amplification of MicroDAQ and allow to measure higher deposited charges. A reduction in the amplification by a factor of ≈ 3 could be achieved for future scintillation detectors by adjusting resistors [Wen].

7.2 Radio electronics

For the interpretation of the measured radio waveforms, the frequencies of the signals are very important. Therefore, all components used in the electronics chain for recording the radio signals are calibrated in the laboratory. The gain as a function of the frequency is shown in figure 7.21. It is visible that the gains of the LNA, the cable and the radioTad are approximately constant over frequency range of interest from 70 MHz to 350 MHz, as desired. The TAXI board shows a suppression of the higher frequencies of interest. The total gain behavior of the system is taken into account in the analyses of the radio signals [Ice21d; IC21].

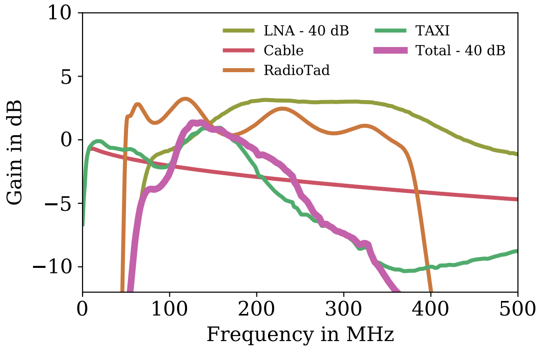

Figure 7.21: Measurement of the electronic gain as a function of frequency. For the sake of visibility, the total gain and gain of the LNA are subtracted by 40 dB. The range of interest from 70 MHz to 350 MHz is covered. The loss of the gain for higher frequencies is accounted for in the analysis of the radio signals. Picture credit: Hrvoje Dujmović.

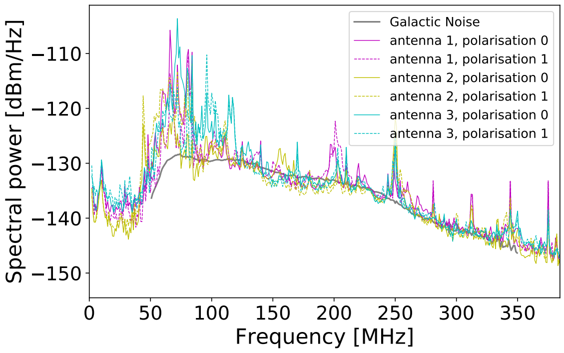

Figure 7.22: Median background spectrum for each antenna and polarization, evaluated from measurements of the SAE prototype on April 17, 2021. The black line shows the expected galactic noise and a thermal noise of 40 K, convoluted with the electronic chain and fits well to the data. Therefore the noise floor is dominated by the galactic noise, as intended. Picture credit: Roxanne Turcotte-Tardif.

Ideally, the background of radio measurements consists only of the thermal and galactic noise. To check how well this is achieved for measurements at the South Pole, software-triggered background measurements are performed with the deployed SAE prototype. These measurements are compared with the expected background, consisting of the Cane model and the predicted thermal noise of the LNA of 40 K [LA+15b], convoluted with the electronic chain. The result is shown in figure 7.22. The measurements with all antennas and polarizations look very similar. The small differences between model and data for medium frequencies could be due either to the not ideal calibration of the SAE prototype or due to additional noise in this range. However, the measured data and the expected background fit well. Therefore the noise floor is mainly the thermal and galactic noise, as intended [Ice21c; IC21].

8

Results of first air-shower data analysis

The basic characteristics of a cosmic-ray air-shower are its arrival direction, the location of the shower axis core and the shower size, see chapter 2.2 [Gri10; Gru20; GER16]. This information can be used for astrophysical studies like anisotropy and multi-messenger searches [Aab+17; Sch19a]. In this thesis, the analysis of these characteristics is used to check if the SAE prototype and the reconstruction of the data work or if improvements are necessary before deploying the entire array.

First, the event rate as a function of the multiplicity of the scintillation detectors is evaluated in chapter 8.1. The effects of the atmospheric temperature and the pressure on the single panel hit rate are shown in chapter 8.2. In chapter 8.3 the timing difference between the scintillation detectors and IceTop are obtained. A comparison of data measured with the SAE prototype and simulations can be found in chapter 8.4. The results of the reconstruction of the air-shower from the data of the scintillation detectors are shown in chapter 8.5. Triple coincidences are events measured in coincidence with the scintillation detectors, the radio antennas and IceTop. The data of each of these detector types is reconstructed individually and the results are compared in 8.6.

Due to the light leaks described in chapter 7.1.3, only data measured in darkness is used for the presented analysis. Two data sets with different measurement settings are used:

- Between March 30, 2021 and June 14, 2021, the highest possible trigger threshold is used, DAC 4095. The SiPM supply voltage is constantly set to AUXDAC 2650. The advantage of the high threshold is a lower firm- and software-induced dead time (cf. chapter 6.2.1). Additionally, a high trigger threshold of the scintillation detectors is advantageous for the triggering of the radio antennas, because of the higher energy threshold of the radio antennas.
- Between June 16, 2021 and July 28, 2021 the trigger threshold of the scintillation detectors is $\approx 0.5\,\mathrm{MIP}$. In order not to miss any low-energy air-showers, the threshold of the scintillation detectors should be as low as possible. However, there is an exponentially decreasing noise component, so if the threshold is too low, mainly noise events are recorded. As a compromise, a threshold of $\approx 0.5\,\mathrm{MIP}$ is used. The threshold is calculated and set for each scintillation detector individually based on the characterization described in chapter 7.

The scintillator data analyzed in this chapter is first converted to units of MIP, as described in chapter 7.1.7. So temperature effects of the detectors are calibrated out. If at least three scintillation detectors recorded a hit within 1 µs, these hits are merged to a scintillator event.

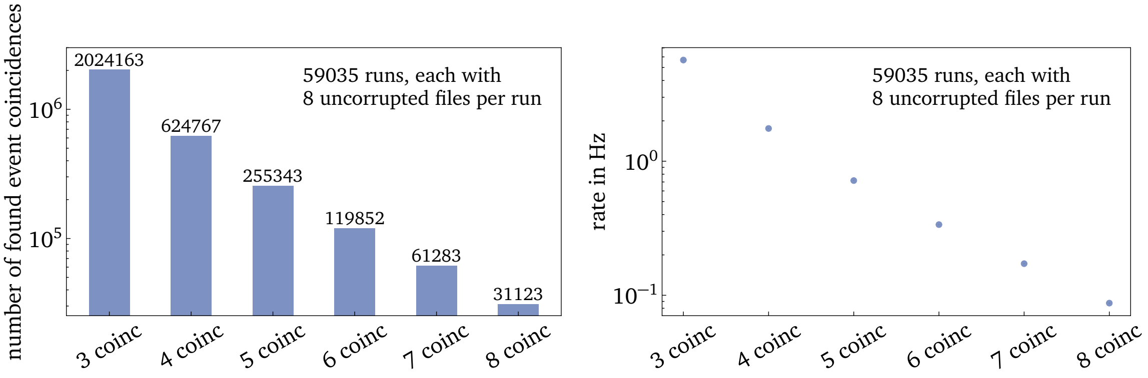

(a) **(b)**

Figure 8.1: The number of coincident events for eight simultaneously measuring detectors is shown in a). The events were measured between June 16, 2021 and July 28, 2021 with a threshold of approximately 0.5 MIP. The expected exponential decrease for larger multiplicities is visible. b) shows the event rate over the multiplicity of the scintillator coincidences. It is evaluated from data with 8 scintillation detectors measuring simultaneously and the total uptime is ≈ 356 088 s.

8.1 Event rate as a function of multiplicity

To verify that the trigger rate is realistic for the future Surface Array Enhancement, the event rate of the scintillation detectors of the SAE prototype must be evaluated. With a threshold of ≈ 0.5 MIP, the single panel hit rate evaluated form the hitbuffer files is ≈ 1 kHz. This is consistent with the results from the threshold scans presented in chapter 7.1.2. Since the single-panel rate is in the same order of magnitude as the single-tank rate of IceTop [Abb+13], the trigger rate for a threshold of 0.5 MIP is not unrealistic for the future array.

To reconstruct air-showers, several detectors need to be triggered within a coincidence time window. A coincidence time window of 1 µs was chosen, because the size of the station is ≈ 135 m, which leads to ≈ 0.5 µs for horizontal showers to cross the station at the speed of light. A factor of 2 was applied, not only considering delayed particles of the air-shower, but also to take into account electronic delays. To do a directional reconstruction, at least 3 scintillation detectors need to be triggered. So only events with at least 3 detectors are evaluated.

The number of coincident events as a function of triggered detectors (multiplicity) within 1 µs is shown in figure 8.1a) and the event rate in 8.1b). The expected exponential decrease with the multiplicity is clearly visible. Due to the low threshold, uncorrelated noise can trigger the readout of the detectors. Therefore, the rate for low multiplicities is slightly higher than expected from a single power law.

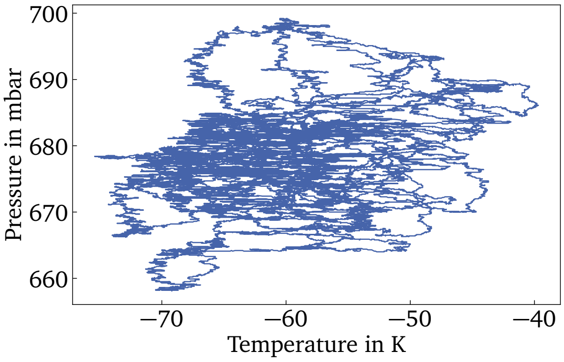

Figure 8.2: The pressure and the temperature of the atmosphere are plotted against each other. No correlation is visible. Original plot by Martin Pittermann, modified.

The readout of the radio antennas is triggered, if at least six scintillation detectors record a hit within 1 µs. This gives a readout rate of ≈ 0.59 Hz, which is reasonable.

8.2 Environmental effects on the single detector hit rate

Seasonal variation are expected, i. e. effects due to the atmospheric temperature and pressure. To check for these variations, the hit rate of the single detectors is evaluated. The plots in this chapter are based on the work of Martin Pittermann.

The weather data is measured by a nearby station and is accessible here [NON]. The pressure of the atmosphere is plotted over its temperature in figure 8.2. No correlation between the pressure and the temperature of the atmosphere is visible.

The data with the high threshold, DAC 4095, has better statistics due to the higher uptime, as well as negligible noise. For that reason it is used in this study. Since the hardware threshold in this data set does not include temperature corrections, a cut on the data excludes all hits below 4 MIP. All detectors show the same behavior. The results of channel 7 are shown in figure 8.3. The plots for all other channels can be found in the attachment, see appendix E.

In the calibration process, the MIP is calculated as a function of the SiPM supply voltage and temperature. Therefore, the data used in this analysis is already temperature compensated and no correlation with the temperature is expected. This is confirmed by measurements, see figure 8.3a).

With increasing atmospheric pressure, more sencondary particles are absorbed by the atmosphere. This leads to a decrease in the hit rate [Gri10]. This expectation is confirmed, see figure 8.3b). A decrease of 0.6 % per mbar is found.

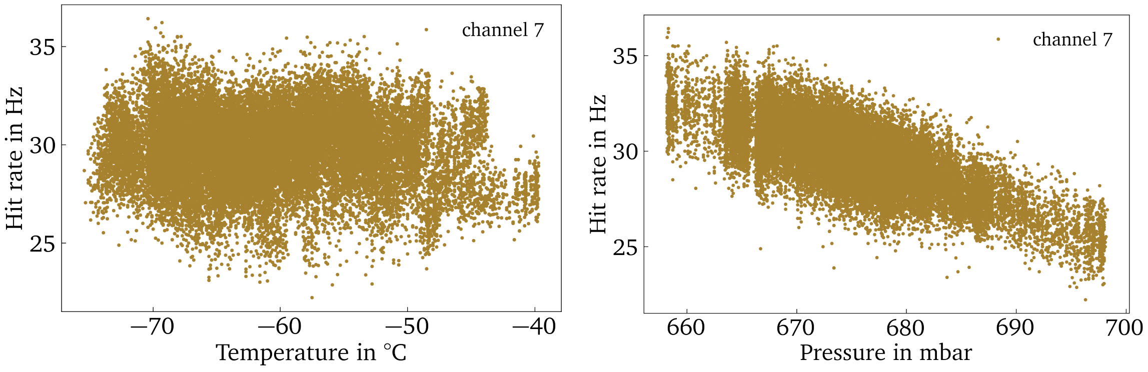

(a) **(b)**

Figure 8.3: Hit rate of channel 7 as a function of the temperature and pressure. A cut on the data excludes hits below 4 MIP for a) and b). Due to the cut, which is based on the calibration described in chapter 7.1.7, no dependence on the temperature is observed in a). As expected, a decrease of the hit rate with the atmospheric pressure can be seen in b). Original plots by Martin Pittermann, modified.

8.3 Timing difference between scintillation detectors, IceTop and radio antennas

The events of the scintillation detectors, radio antennas and IceTop are merged according to timestamps. The timing difference between the scintillation detectors, radio antennas and IceTop is evaluated to check if both, the timing and the merging of the events work.

The merging, written by Hrvoje Dujmović, is done as follows: If at least three scintillation detectors record a hit within 1 µs, these hits are merged into a scintillator event and the timestamp of the first scintillator hit is taken as reference. The radio trigger time is corrected with a constant offset of +899 998 909 ns and merged with the scintillator events using a 10 µs window. For coincident scintillator and radio events, the scintillator reference time is taken as start time of this event. If the start time is in the interval between the start and stop time of an IceCube event, the events are merged with the IceCube event. Typically, the duration of an IceCube event is 20 µs with the trigger centered in this interval [Aar+17c].

To check if the timing of the scintillation detectors, radio antennas and IceTop match, the core times of coincident events are compared. Scintillator events are reconstructed with the reconstruction described in chapter 8.5 and the reconstructed core time is taken as reference. For radio the trigger time is used. IceTop events are reconstructed with the IceCube reconstruction software Laputop and the core time is taken. The result is shown in figure 8.4. The timing of most events matches. Therefore the timing of the events works.

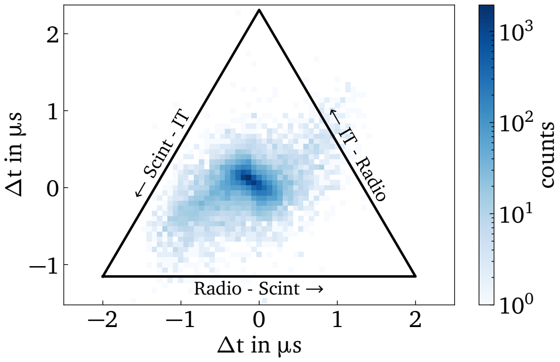

Figure 8.4: Time difference between the reconstructed core time of the scintillation detectors, the reconstructed core time of IceTop (IT) and the radio trigger times. For most events, the timing matches very well.

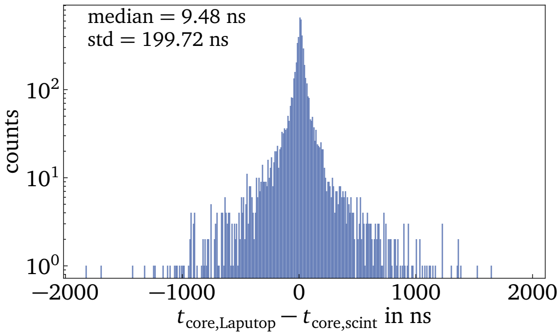

Figure 8.5: Time difference between the core times evaluated by Laputop and the scintillator reconstruction. Only events with 8 coincident scintillator hits within 1 µs and with an coincident IceTop event are evaluated. The timing differences due to the difference in the position of the core is corrected. This value of standard deviation is compatible with the expected performance of the reconstruction from simulations.

In figure 8.5 the differences between the core times of IceTop and the scintillation detectors are shown for scintillator events with a multiplicity of eight and a corresponding IceTop event. Since the Laputop and scintillator reconstruction can yield different core positions, the core times are shifted accordingly. This effect is corrected for in figure 8.5. The median is a constant offset and can be corrected. The standard deviation of 200 ppb is in the range expected from the reconstruction algorithms and is not critical for the merging of the events.

8.4 Comparison with simulations

To check if the measured detector behavior is understood the measured data is compared to simulations. The reconstruction used in chapter 8.5 was developed based on simulations. Therefore, it is necessary to check if data and simulations agree to verify that the scintillator reconstruction can be used. Since the simulations use a detector threshold of 0.5 MIP, the data set measured between June 16, 2021 and July 28, 2021 is taken.

For the comparison, the distributions of the arrival directions, the core positions and the energies of the air showers need to match between data and simulations. To get this information, all air-shower events which were measured in coincidence with IceTop are taken and the reconstruction of IceTop is taken as reference. This is possible, because IceTop is a well studied and calibrated detector [Abb+13]. The distributions reconstructed from IceTop are shown in figure 8.6 and are taken as input for the simulations.

The simulations were done by Agnieszka Leszczyńska. Air showers induced by proton and iron primaries are simulated with CORSIKA [Hec+98], with zenith angles up to 71.6° in steps of $\sin^2(\theta) = 0.1$. The energy of the air showers is between $\log(E/\mathrm{eV}) = 13.0$ and $\log(E/\mathrm{eV}) = 16.8$ in steps of $\log(E/\mathrm{eV}) = 0.1$, so mainly low-energy air-showers. The core of the simulated air-showers is within a 500 m radius from the center of the SAE prototype. The layout of the scintillation detectors is based on the GPS survey (see figure 5.2) and the model of the scintillation detector behavior is taken from [Les21]. 100 air showers are simulated per energy and zenith angle bin and each air shower is resampled 5 times. The weighting of the air-showers is done by energy according to the H4a model [Gai12] to represent a realistic flux.

The distribution of the simulations can be found in the appendix F. It is visible that the distributions of the simulations and of the events measured in coincidence with IceTop match. The multiplicity of the triggered detectors per event for data and simulations is shown in figure 8.7. The cut excluding multiplicities below 3 is also applied to the simulations. Due to uncorrelated noise hits, more hits with low multiplicities are measured in data. Overall, the distribution of the multiplicities

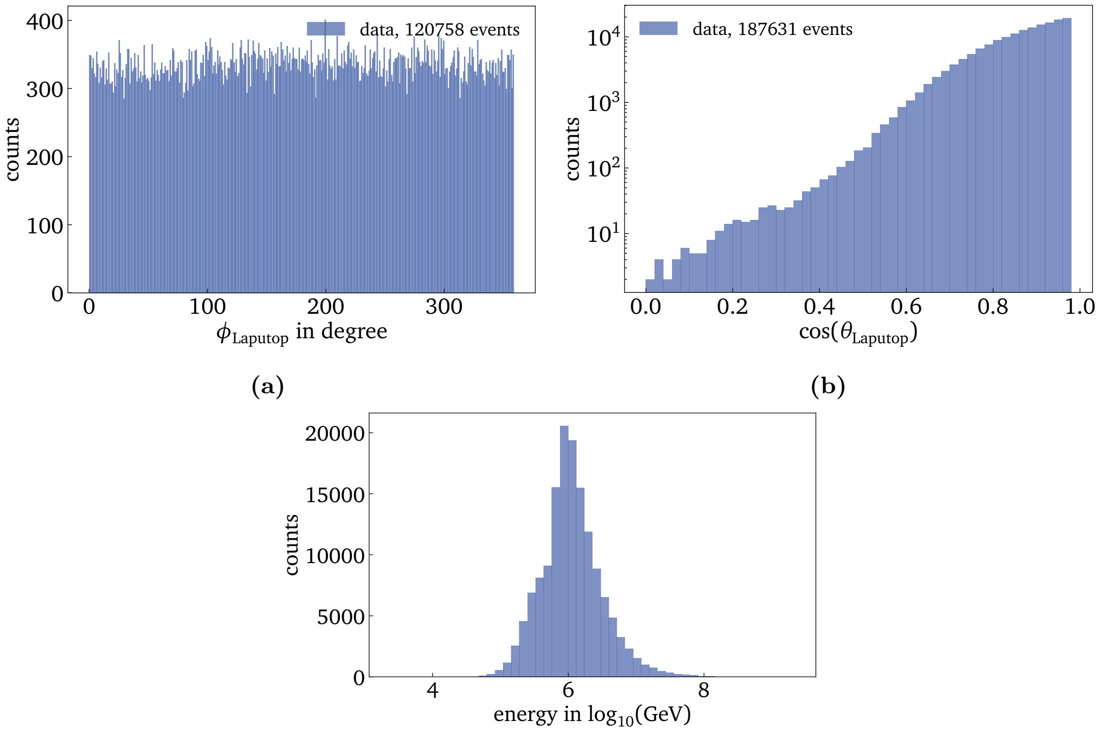

(a) **(b)**

(c)

Figure 8.6: Distribution of the azimuth (a) and zenith angles (b), and the energy (c) reconstructed with Laputop from June 16, 2021 until July 28, 2021. Only events with a scintillator coincidence of ≥ 3 within 1 µs and with a corresponding IceTop event are evaluated. The energy reconstruction from IceTop has not been validated for the data from 2021 and can be inaccurate due to snow attenuation effects. As expected, the distribution of the reconstructed azimuth angle is very uniform and the number of events decreases for high zenith angles. Mainly air-showers in the PeV range are measured due to the steeply falling cosmic-ray spectrum. Since the scintillator station has a lower energy threshold than IceTop, more low-energy air-showers will be detected with the scintillation detectors only.

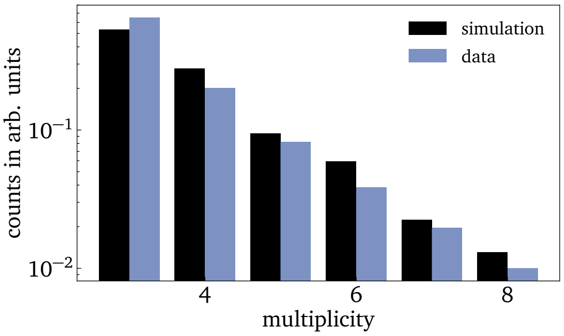

Figure 8.7: Comparison of the multiplicity between simulations and data. Uncorrelated noise hits increase the low multiplicities in the data. Overall, the multiplicities of simulations and data are compatible.

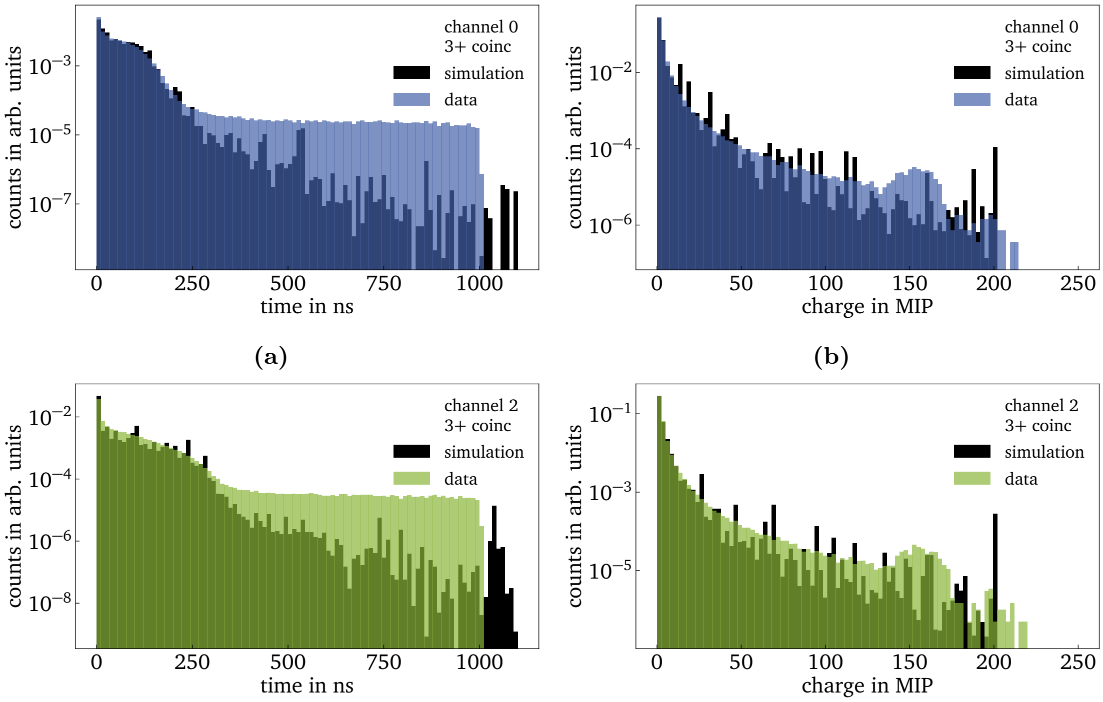

(a) **(b)**

(c) **(d)**

Figure 8.8: Distribution of the timestamps (a), c)) and of the charge (b), d)) for simulations and data. The distributions are plotted exemplary for one of the central scintillation detectors (channel 0) and one outer scintillation detector (channel 2). In a) and c) the timestamps of the events relative to the first timestamp of the scintillation detectors of the event are plotted. Since the first timestamp of each event is set to zero, a pileup in the first bin is visible. In the data, single uncorrelated muons and noise contribute to the tail for large times. The cut at 1 µs is due to definition of the coincidence time window. Overall, data and simulations agree. In b) and d) the measured charge is shown. The behavior of simulations and data is similar. The saturation of the detectors in the data leads to the pileup at around 150 MIP. In the simulations a hard value of 200 MIP is used as a saturation level.

between data and simulation are compatible.

The distribution of the timestamps and the charges for single detectors are shown in figure 8.8 for two detectors. All simulations are used and are weighted with the H4a flux. To simulate the saturation of the detectors all charges above 200 MIP are assumed to be saturated and therefore their signal value is fixed to 200 MIP. A cut excludes all charges below 0.5 MIP and all multiplicities below 3 for both, simulations and data. Channel 0 is one of the central scintillation detectors and channel 2 is one of the outer detectors. The plots for the other detectors look similarly. The timestamps are relative to the first scintillator timestamp of the event. In the data, likely uncorrelated muons and noise contribute to the constant tail on the percent level for large times. The saturation of the scintillation detectors (cf. chapter 7.1.9) is clearly visible in the data as an excess at around 160 MIP. The spikes in the simulations are due to the

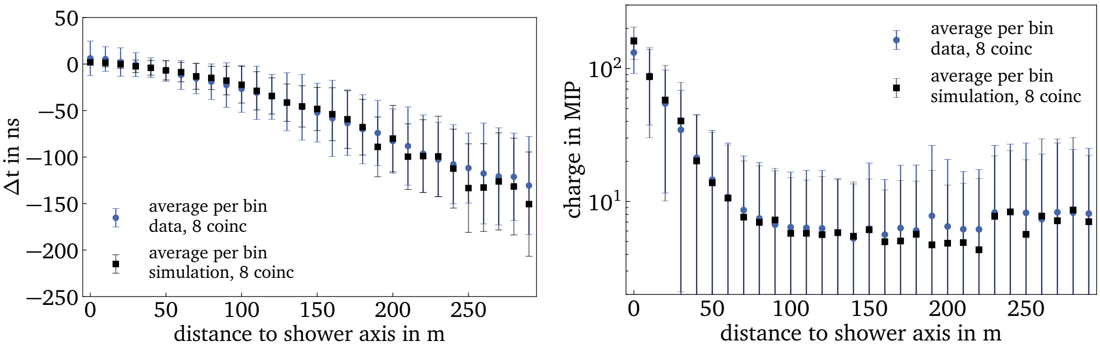

(a) **(b)**

Figure 8.9: Average curvature of the air-shower front a) and LDF b) for simulations and data. In a) the time delay with respect to the plane front approximation Δt is plotted as a function of the distance to the shower axis. To maximize the information per event, only events with a multiplicity of eight are included. The average is calculated per bin, including weighting for the simulations. The error bars indicate the weighted standard deviation per bin. The constant offset between the simulations and data is corrected to simplify the comparison of the shape. Misreconstructed core positions in combination with low statistics lead to the fluctuations for large distances. The average curvature of the air-shower front agree for simulations and data. The lateral distribution is shown in b). The weighted average and standard deviation is calculated per bin. The fluctuations for large lateral distances are due to misreconstructed core positions and low statistics. Simulations and data agree.

weighting and the low statistics. The behavior of both, timestamps and charges, agree for simulation and data.

The average curvature of the air-shower front is shown in figure 8.9a). The time delay is calculated with respect to the plane front approximation from the scintillator reconstruction. Also the lateral distance is calculated with respect to the scintillator reconstruction. The constant time offset is corrected in the data. For lateral distances above 200 m, the statistics are low for simulations. Fluctuations are visible for large lateral distances. This can be explained by misreconstructed core positions in combination with lower statistics: If the core position is misreconstructed, the calculated lateral distance will change accordingly. Thus, the smaller time delay for small lateral distances will be put erroneously into the bin for larger lateral distances, leading to a smaller average time delay for this bin. The opposite, so if the core position is misreconstructed in a way leading to an erroneously small lateral distance, the effect on the average time delay of the bin is negligible due to larger statistics for small lateral distances.

The average lateral distribution is visible in figure 8.9b). The lateral distance is calculated with respect to the scintillator reconstruction. For simulations, all charges above 200 MIP are set to 200 MIP in this plot, to mimic the saturation of the detectors. The average charge is calculated per bin. In the data, temperature changes affect

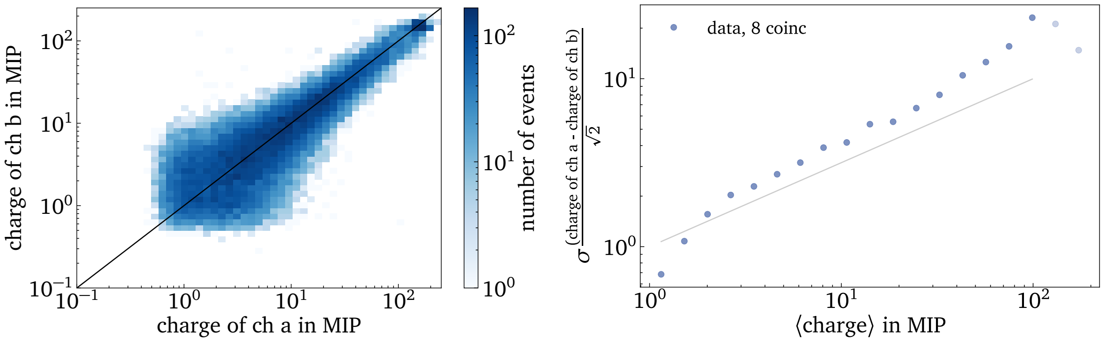

(a) (b)

Figure 8.10: The comparison of the charge of the neighboring scintillation detectors is plotted in a). To increase statistics, all four detector pairs are taken into account. Channel a is the sum of all detectors with even channel numbers and channel b with odd channel numbers. It is assumed that the 5 m distance between the neighboring detectors are negligible compared to the size of the air-shower footprint. Therefore, both detectors measure at similar lateral distances and the expectation value for the signals is similar. This is visible in a). In b) the signal spread is shown. For high charges the signal spread drops due to saturation effects of the scintillation detectors and for low charges due to threshold effects. The grey line corresponds to fluctuations according to Poisson statistics. The results are consistent with the simulations done in [Les21].

the saturation threshold of the scintillation detectors, lowering it below 200 MIP for low temperatures. This leads to the small difference for small lateral distances. The fluctuations for large lateral distances are due to misreconstructed core positions.

The layout of the SAE prototype has four pairs of scintillation detectors, with only 5 m distance between the neighboring detectors. Compared to the footprint of an air-shower, this distance should be negligible. Therefore, the expectation value of the measured charge for both detectors is nearly the same. This is visible in figure 8.10a). The signal spread, so the accuracy of the signal, is shown in figure 8.10b). The method is based on [Ave+07; Les21]. The signal spread is due to the differences in the air-shower development and fluctuations in the detector response. The decrease at high charges is caused by the saturation of the scintillation detectors. For low charges, threshold effects decrease the spread. Since the fluctuations in the air-shower development and the detector response are stochastic, the spread is expected to be proportional to Poisson statistics. In the plot this expectation corresponds to the square root of the charge and is plotted in grey. However, the data does not follow Poisson statistics. This could originate from the wrong assumption that the distance between the neighboring scintillation detectors is negligible in the steeply falling lateral distributions close to the core. The correction for the lateral distribution function (LDF) should be applied in the future to validate this. Further investigations are necessary to clarify the reason for this non-Poissonian behavior. However, the comparison of the charges of neighboring detectors as well as the signal spread is consistent with the simulations performed in [Les21].

8.5 Reconstruction of air showers

The measurement of the cosmic rays using air-showers is indirect. Therefore, the properties of the primary particle have to be reconstructed from the distribution of the signals and timestamps recorded by the array [Gri10]. Based on simulations, a reconstruction algorithm was developed to obtain, among others, the direction of the primary particle. Since simulations and data match (cf. chapter 8.4), the reconstruction can be tested on data of the SAE prototype. The analysis of the reconstructions presented in this chapter is thus a check of both, if the reconstruction algorithm succeeds to reconstruct data and if the SAE prototype works as a cosmic-ray air-shower detector station.

8.5.1 Reconstruction of scintillator hitbuffer data

The reconstruction for the scintillation detectors used in this thesis was written by Agnieszka Leszczyńska using the *RockBottom* framework [Les21]. The basic idea is to fit the lateral distribution of the signals and the trigger times of the scintillation detectors for each event. These fits are done by iteratively minimizing the negative log-likelihood functions [Les21].

The scintillator reconstruction procedure is described in the following. As a first estimate for the core position, the mean of the scintillator positions (r_i) weighted with the signal (S_i, charge in MIP) is calculated,

$$\mathbf{r} = \frac{\sum_i r_i S_i}{\sum_i S_i} \quad . \tag{8.1}$$

The first estimate for the direction of the air shower is taken from the plane front approximation. In this approximation, the direction of the primary particle $\mathbf{n}$ and the core time t_0 are obtained by minimizing

$$\chi^2 = \sum_i \frac{\left(t_i - t_0 + {}^{n_x x_i}/_{c} + {}^{n_y y_i}/_{c}\right)^2}{\sigma_i^2} \tag{8.2}$$

with the timestamp of each detector t_i, its position (x_i, y_i) and $\sigma_i = 5\,\text{ns}$. Since the relative heights of the scintillation detectors are approximately the same, the z-components are neglected. These first estimates are used as the initial parameters in the following steps.

To obtain the core position (x, y), the core time (t_0), the direction (θ, ϕ) and the shower size $(S_\text{ref} = S(R_\text{ref}))$, the lateral distribution and the shower front curvatures are fit. The shower front curvature is fit with a parabola,

$$\Delta t(r) = ar^2 + b \tag{8.3}$$

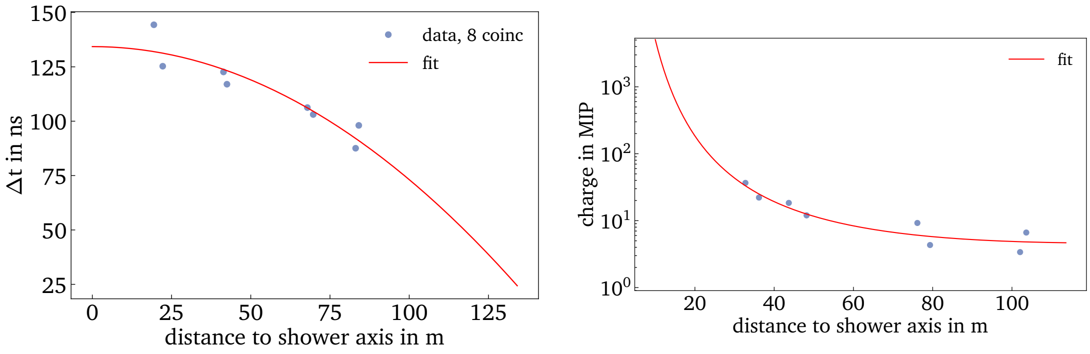

(a) **(b)**

Figure 8.11: Fit of the curvature of the air-shower front a) and LDF fit b) to single events. Only events with a scintillator coincidence of 8 are used to have as many data points per event as possible. A parabola is fit to the time delays with respect to the plane front from the Laputop reconstruction in a). From the mean of the obtained fit parameters, a and b in equation 8.3 are fixed. In b) a LDF is fit to obtain κ and β.

with the lateral distance r, by minimizing the negative timing log-likelihood

$$\ln \mathcal{L}_t = -\sum_i \sqrt{S_i}\left(\frac{1}{2}\cdot\left(\frac{\Delta t_i}{\sigma_{t_i}}\right)^2 + \ln\left(\sqrt{2\pi\sigma_{t_i}^2}\right)\right) \quad . \tag{8.4}$$

The double logarithmic paraboloid function is used to fit the lateral distribution of the detector signals,

$$S(r) = S_{\mathrm{ref}} \cdot \left(\frac{r}{R_{\mathrm{ref}}}\right)^{-\beta-\kappa\log_{10}\left(\frac{r}{R_{\mathrm{ref}}}\right)} \quad . \tag{8.5}$$

This is done by minimizing the sum of the negative log-likelihoods for the triggered detectors $\mathcal{L}_{\mathrm{tr}}$, the saturated detectors $\mathcal{L}_{\mathrm{sat}}$ and the silent detectors $\mathcal{L}_{\mathrm{sil}}$,

$$\ln \mathcal{L} = \ln \mathcal{L}_{\mathrm{tr}} + \ln \mathcal{L}_{\mathrm{sat}} + \ln \mathcal{L}_{\mathrm{sil}} \quad . \tag{8.6}$$

In the first step, the core position and S_{ref} are fit, while fixing all other parameters. In the second step, the direction, the core time and S_{ref} are fit, while keeping the core position fixed. In a third step, the core position and S_{ref} are fit again. Further details on the reconstruction procedure can be found in [Les21]. To obtain stable reconstruction results, at least five scintillation detectors must record a hit. For all events with a lower multiplicity only the plane front approximation and the first estimate of the core position are performed.

For the reconstruction of the data of the SAE prototype, all parameters which are not fit for each event must be fixed based on fits to simulations. To maximize the number of sampled points per event, only events with a multiplicity of eight are used.

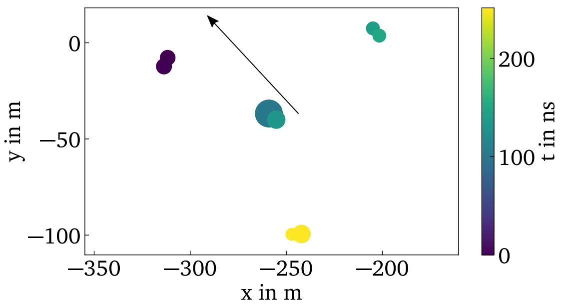

Figure 8.12: 8 coincidence in scintillator data. The circles show the position of the scintillation detectors in IceCube coordinates. The size of the circles is proportional to the charge measured by the scintillation detectors and the color indicates the time relative to the first scintillator timestamp of this coincidence. The arrow starts at the reconstructed core position and points towards the reconstructed direction: $\theta \approx 42.3°$ and $\phi \approx 41.5°$.

- κ, β from equation 8.5: κ and β are defined by performing fits to single events, see figure 8.11b). Bad fit results are rejected. The approximate mean of the fit results is taken, $\kappa = 0.6$ and $\beta = 2.7$.
- R_{ref}: The reference distance R_{ref} is obtained by taking the average of $\log_{10}(r)$ [Kis12]. This results in a reference distance of ≈ 140 m, so roughly the size of the SAE prototype. The reference distance of IceTop is 125 m. Since the obtained 140 m are close to the IceTop reference distance, R_{ref} is set to 125 m for the following reconstructions. This enables better comparisons with the signal strength of IceTop at the same lateral distance.
- a, b from equation 8.3: Single data events are fit with equation 8.3 as shown in figure 8.11a). The mean of the obtained fit parameters is taken, leading to $a = -0.00183$ and $b = 0$.

For measured data, the true direction and core position of the primary particle is unknown. Therefore, the accuracy of the reconstruction is evaluated from the simulations. The true and the reconstructed values are compared. The resolution of the reconstruction is derived from Gaussian fits to the histogram of the difference between true and reconstructed values. For a multiplicity of eight and true energies up to $\log(E/\text{eV}) = 15.7$, the resolution of the zenith angle θ is 2.61° and of the azimuth angle ϕ 3.97°. One sigma corresponds approximately to the 68.27th percentile and will hereafter be referred to as 68th percentile. The 68th percentile on the angular distance between true and reconstructed direction is 7.49°. The 68.27th percentile on the distance between the true and reconstructed core position leads to a core resolution of ≈ 103.9 m.

With the described reconstruction method all measured scintillator events are reconstructed. The reconstruction results look promising. An example event is shown in

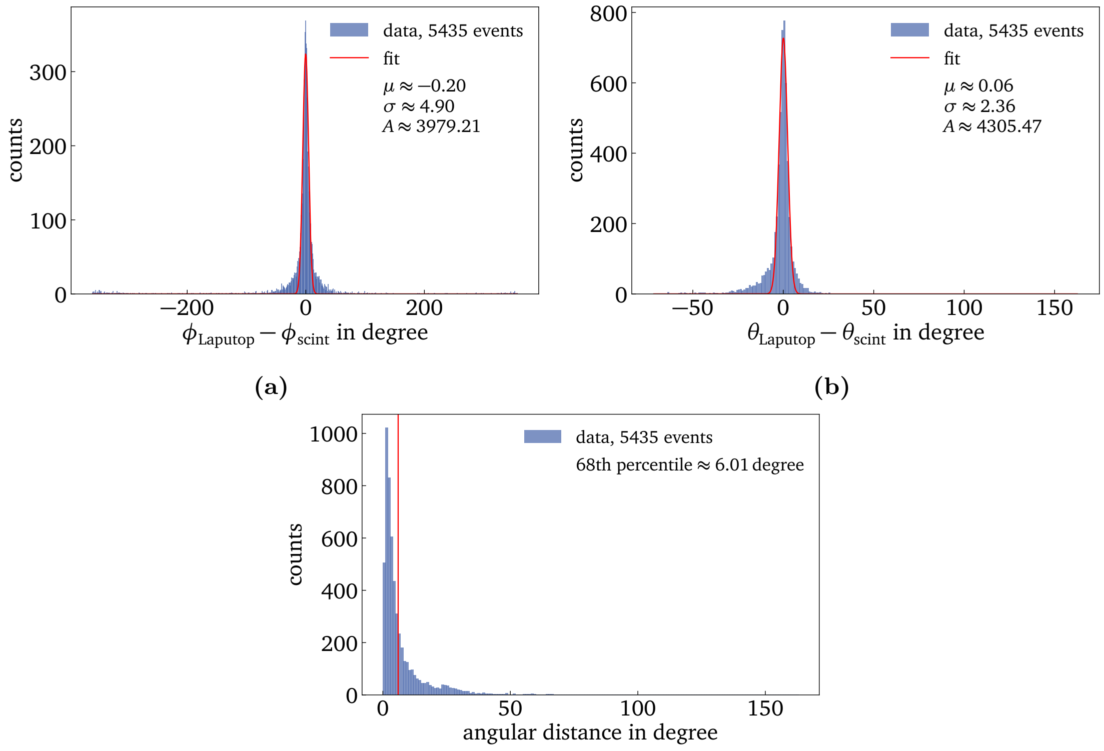

(a) **(b)**

(c)

Figure 8.13: Difference between the azimuth (a) and zenith angles (b) reconstructed with the scintillator reconstruction and reconstructed with Laputop. Only events with a coincidence of 8 scintillator hits within 1 µs and with a corresponding IceTop event are evaluated. With a 68th percentile of the angular distance of 6.01°, the reconstructions show good agreement.

figure 8.12. The comparison of the reconstruction results with IceTop are shown in the next chapter.

8.5.2 Comparison of the reconstruction results of scintillators and IceTop

To assess how good the scintillator reconstruction results are, they are compared to IceTop. IceTop is a well calibrated detector [Abb+13] and can be taken as reference. Only events which were measured in coincidence by both, scintillation detectors and IceTop are taken for this comparison. The reconstruction of the IceTop data is done with Laputop, while the scintillator data is reconstructed with the scintillator reconstruction described in chapter 8.5.1.

The difference for the reconstructed azimuth and zenith angles are shown in figure 8.13. Especially for almost vertical showers, a small difference in the direction can lead to a big difference in the azimuth. This leads to larger differences in the azimuth angles than for the zenith angles. With an angular resolution of 6.01° for a scintillator multiplicity of eight, the reconstructions show good agreement. The results

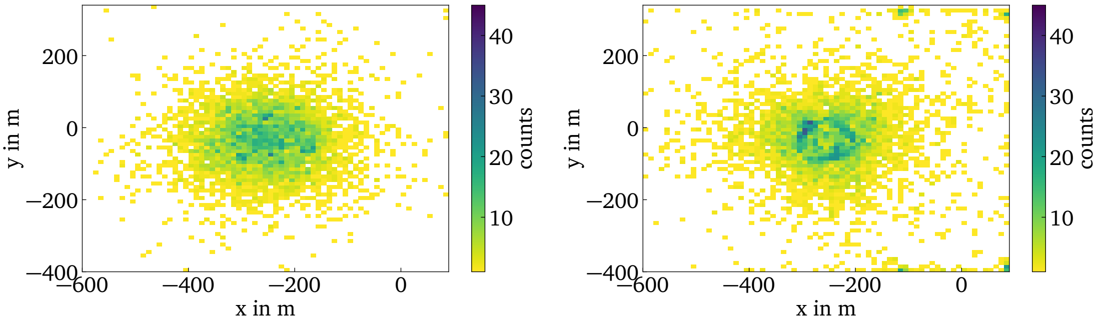

(a) (b)

Figure 8.14: Distribution of the core position reconstructed with Laputop a) and with the scintillator reconstruction b). Only events with a coincidence of 8 scintillator hits within 1 µs and with a corresponding IceTop event are evaluated. Overall, the distributions of the core positions agree.

for lower multiplicities can be found in appendix G.1.

The reconstructed core positions from Laputop and the scintillator reconstruction are shown in figure 8.14. The scintillator reconstruction has a small bias towards the positions of the scintillation detectors. The overall distributions of the core positions agree. The 68th percentile on the distance between the core positions reconstructed with Laputop and the scintillator reconstruction is 70.34 m.

It is worth noting that not only the uncertainty from the scintillator reconstruction but also the uncertainty from Laputop influences the results. For 1 PeV the angular resolution is $\approx 1°$ and the core resolution is $\approx 20\,\mathrm{m}$ [Abb+13; Ice16]. For lower energy and for inclined events the resolution gets worse. Thus, the results of the scintillator reconstruction are competitive to Laputop.

8.6 Triple Coincidences

With the SAE prototype events can be measured in coincidence with the scintillation detectors and the radio antennas of the SAE prototype as well as IceTop (triple coincidence). Each of these detector types can reconstruct the same air shower individually. This provides an opportunity to crosscheck the results from all three detector types.

The data from the scintillation detectors is reconstructed by the scintillator reconstruction and for IceTop data the Laputop reconstruction is used. The data processing and reconstruction of the radio data is developed by Hrvoje Dujmović et al. The radio data, which is measured in coincidence with IceTop, is reconstructed in the following way: An cut in energy is applied by requiring that S_{ref} of Laputop is above $\log_{10}(S_{\mathrm{ref}}) > 0.5$. A background-weighted frequency filter is applied to suppress frequencies with known RFI [Ice21d; IC21]. Then the traces of both polarisations

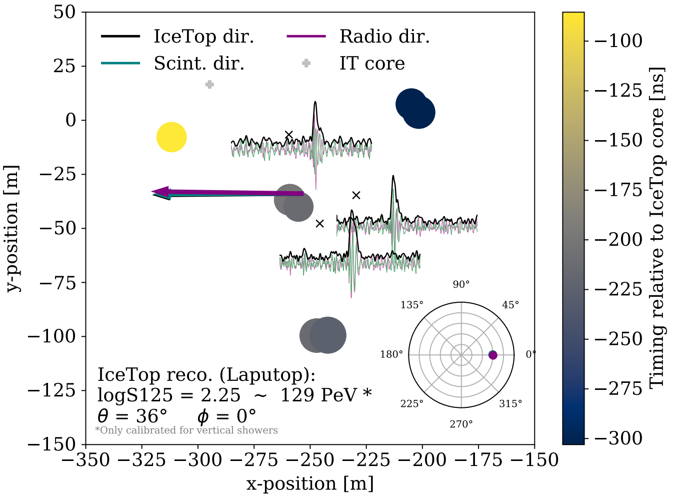

Figure 8.15: Example of a triple coincidence event. The air shower was measured by the scintillation detectors, the radio antennas and IceTop. The circles show the position of the scintillation detectors, the size of the circles is proportional to the charge measured by the scintillation detectors and the color indicates the time relative to the IceTop core time. The positions of the antennas is marked with black crosses. The measured waveforms of the two directions of each antenna are plotted close to the corresponding antenna as well as the envelope. For each of these detector types, the air shower can be reconstructed. The core position reconstructed by Laputop is marked by the grey cross. The reconstructed direction is indicated by the colored arrows for each detector type respectively. The length of the arrow is proportional to $\sin(\theta)$. The reconstructions for all detector types agree. Picture credit: Hrvoje Dujmović.

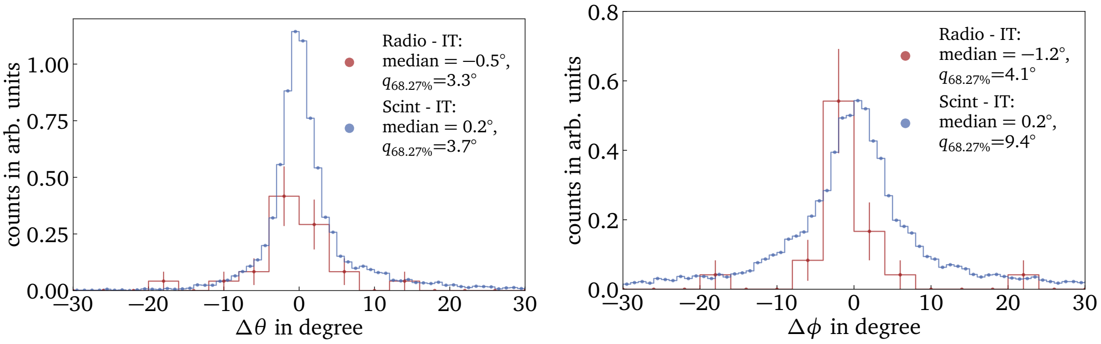

(a)

(b)

Figure 8.16: Difference between the zenith (a) and azimuth angles (b) between the three detector types scintillation detectors (scint), radio antennas (radio) and IceTop (IT). The error bars are the statistical uncertainties. The median and the 68th percentile ($q_{68\%}$) are calculated. The reconstructions show good agreement.

are added per antenna and the envelope is calculated using a Hilbert transformation. Then, the highest peak in the envelope is found. A cut is applied to exclude all events with a signal-to-noise ratio above 7 for all antennas, where the signal-to-noise ratio is calculated as the amplitude of the highest peak divided by the median amplitude of the trace. Additionally, all events are cut where the highest peak occurs at exactly the same time, since these peaks are noise from the TAXI board. Afterwards, the cable delays are corrected and the plane front is reconstructed from the time of the highest peaks [Ice21d].

An example of a triple coincidence event is shown in figure 8.15. The comparison of the reconstructed directions of all three detector types can be found in figure 8.16. All scintillator events with a multiplicity of eight and a corresponding IceTop event as well as selected radio events are compared. Due to the higher energy threshold of the radio antennas more scintillator events are found. The reconstructions of all detectors agree within 4° for the zenith and 10° for the azimuth angle. The 68th percentiles of the radio reconstructions are smaller because the shown radio data are from the high quality sample. Thus, the crosscheck of all three detector types is successful and no game-stoppers have been found so far.

9

SUMMARY AND OUTLOOK

The surface component of the IceCube Neutrino Observatory, IceTop, is used to study cosmic-ray air-showers and as a veto for the in-ice detector. However, due to snow accumulation the systematic uncertainties as well as the energy threshold of IceTop increase. To mitigate and calibrate the effect of the snow accumulation, to lower the energy threshold and to improve cosmic-ray measurements, a Surface Array Enhancement is planned.

The Surface Array Enhancement will consist of 32 hybrid stations, which will be installed in the next years. Each station encompasses eight scintillation detectors and three radio antennas, which are connected to a central DAQ. Two previous prototype stations have been deployed at the South Pole in 2018 to 2019. In the frame of this thesis, the designs of the previous stations have been merged to a new optimized design, combining the advantages of both systems. While the previous stations were used as R&D for the SAE, this station is the test of the actual design which will be used in the enhancement. In the new design, the scintillation detectors are read out by a Silicon Photomultiplier (SiPM) and the SiPM signals are integrated and digitized inside the detectors. The digitized data is then sent to the central DAQ. Additionally, the scintillation detectors send signals to the central DAQ to trigger the readout of the radio antennas. The focus of this thesis is on the scintillation detectors. The signals of the analog radio antennas are sampled and digitized inside the central DAQ.

A prototype station was built, shipped to the South Pole and deployed. Since the commissioning, the station is constantly running and delivers data. A daily run procedure is developed which collects both, data for the calibration of the detectors and air-shower data.

The scintillation detectors are characterized and calibrated. The detectors show a high MIP light yield, which enables a low energy threshold. The temperature effects of the SiPM are compensated in the data analysis. Light leaks have been found in some of the scintillation detectors. Thus, the design of the housing of the scintillation detectors has been adjusted to prevent leaks in future detectors. The stability of the baseline is good in the austral winter, which ensures good data quality.

The first analyses of the cosmic-ray air-shower data of the prototype station are presented. A method to combine the individual scintillation detector measurements to air-shower events is developed. The measured events of the scintillation detectors are compared with the simulations of the IceCube collaboration and show good agreement. This does not only imply that the simulations are correct, but also that our understanding of the scintillation detector effects is correct. The scintillator reconstruction is applied for the first time to measured air-shower data. Previously, the scintillator reconstruction has been developed for the full array [Les21]. In this thesis, the reconstruction has been optimized for a single station. The reconstruction results show the expected air-shower distributions and performance of the detectors.

Events were measured in coincidence with the scintillation detectors and IceTop. A comparison of the reconstruction results shows good agreement with an angular resolution of $\approx 6°$ for events with hits from eight coincident scintillation detectors. The angular resolution is competitive to the IceTop reconstruction. Triple coincidences, i. e. events measured in coincidence with the scintillation detectors, the radio antennas and IceTop are found. Each detector type is reconstructed individually and the results agree with each other.

In the future, a new firm- and software will increase the uptime of the prototype station. This will improve the statistics of the analyses and enable further studies. Since the prototype station shows good results, it is used as the baseline design for the future surface air-shower array of IceCube-Gen2. Also, the experimental verification of the simulations confirms the basis for the IceCube-Gen2 simulations of the surface array which are currently being developed. As soon as additional stations will be deployed, the reconstruction of air-showers can be further improved, leading among others to a better directional resolution and core position as well as enabling studies of the primary particles mass. This will be further improved by combining the reconstructions of the scintillation detector, the radio antennas, IceTop and IceCubes in-ice detector, turning it into an composite hybrid detector array. Thus, the prototype station paves the path to gain knowledge and make new discoveries in astroparticle physics.

APPENDIX

A Supplementary material about MicroDAQ

A.1 Shaping network

The shaping network is a linear RLC network. Its output is proportional to the number of single P.E.s. The network has a linear response, so if for example the amount of the P.E. is doubled in the input, V_{out} is doubled, etc. It is optimized for SiPM signals, so other waveforms will lead to different results.

The basic idea of the RLC network is to approximate a square wave by a Fourier series. Therefore, the linear network has a ringing behaviour. Like a lot of small resonating circuits behind each other, it responds with "wiggles" on different time scales. These different contributions add up to a "square wave" with an amplitude proportional to the number of P.E.s. After some time ($\approx 100\,\mathrm{ns}$), V_{out} decreases to the baseline [Wen].

A.2 Sampling delay times above 100 ns

MicroDAQ has 2 ADCs for the high amplification and 4 ADCs for the medium and low amplification respectively. The sampling delay times of the ADCs of an amplification channel can be set to different values. The sampling delay times of the different amplification channels are linked, however. Finding reasonable settings is not trivial, so contact Chris Wendt to crosscheck the settings before starting the measurements. This can be used for

- creating an arrival time profile. When sampling at the time $t_{\mathrm{i}} < 100\,\mathrm{ns}$, it measures integral number of photons up to this time $\int_0^{t_{\mathrm{i}}} \frac{\mathrm{d}N}{\mathrm{d}t}\mathrm{d}t$. For $t_{\mathrm{i}} > 100\,\mathrm{ns}$ further studies are required to get proper results, see next item.
- making studies about how "earlier MIPs" influence V_{out} for sampling delay times above 100 ns. So e. g. if you have one MIP, usually V_{out} has dropped to 30 percent of the original V_{out} value after x ns etc. With studies like this, it is possible to increase the sampling delay time of some ADCs to capture more delayed particles [Wen].

A.3 Improvement of the timing accuracy by using the delay lines of MicroDAQ

The time counter capture registers on MicroDAQ run with 180 MHz. So after $\approx 5.5\,\mathrm{ns}$, the counter is increased by 1. The signal of the discriminator is fed into eight subsequent 1 ns delays. The output of a delay line is connected to the input of the next delay line, so each input sees the edge $\approx 1\,\mathrm{ns}$ later than the one before. For each of these delayed signals, the counter capture registers record the value of the counter at the moment of the edge of the signal, see figure A.1. By averaging the captured time values, an accuracy of $\approx 1\,\mathrm{ns}$ is achieved.

The delays are not identical and the delay times can differ up to $\approx 50\,\%$. Additionally, the paths inside the microprocessor are also not completely identical. So to improve the accuracy further, the delays have to be calibrated. The basic idea of this calibration is to take data and plot the captured time values in the registers as a histogram. If the delays are all identical, the bins in the histogram all have the same height. If the delay times are not identical, the ones with bigger delays will cause higher bins in the histogram. To calibrate the delays, the delay times are "shifted" until the histogram has even-height bins. This is not implemented yet. If you want to do this, please contact Chris Wendt for further information [Wen].

A.4 List of firmwares for MicroDAQ used in this thesis

- udaq-beacon-aug_6_2019.bin: for testing receiving messages on TAXI, raw-ascii.
- udaq-echo-aug_6_2019.bin: for testing sending and receiving messages, raw-ascii, no fast timeouts.
- uDAQv4.0-chw-trigout1Hz-20190821.bin: for testing receiving triggers on TAXI.
- CLOCK_INTERNAL_NO_PPS_udaq-raw-ascii-with_echo_apr_2_2020.bin: raw-ascii, using internal substitution for PPS signal from WR.
- AUX_UART_udaq-raw-ascii-apr_3_2020.bin: raw-ascii, communicating via the debug pins.
- AUX_UART_NO_PPS_udaq-raw-ascii-apr_3_2020.bin: raw-ascii communicating via the debug pins, using internal substitution for PPS signal from WR.
- udaq-raw-ascii-sept_11_2019.bin: raw-ascii.
- udaq-raw-ascii-with_echo_mar_24_2020.bin: raw-ascii, everything MicroDAQ receives or sends is also output on the debug pins to crosscheck the communication between TAXI and MicroDAQ.
- uDAQv4.0-chw-20190715.bin: legacy COBS encoded, fast timeouts.
- uDAQv4.0-chw-tjb-3sec-to-20200508.bin: legacy COBS encoded, should be identical to uDAQv4.0-chw-20190715.bin except for more friendly timeouts. This is the firmware used for measuring the data in this thesis.

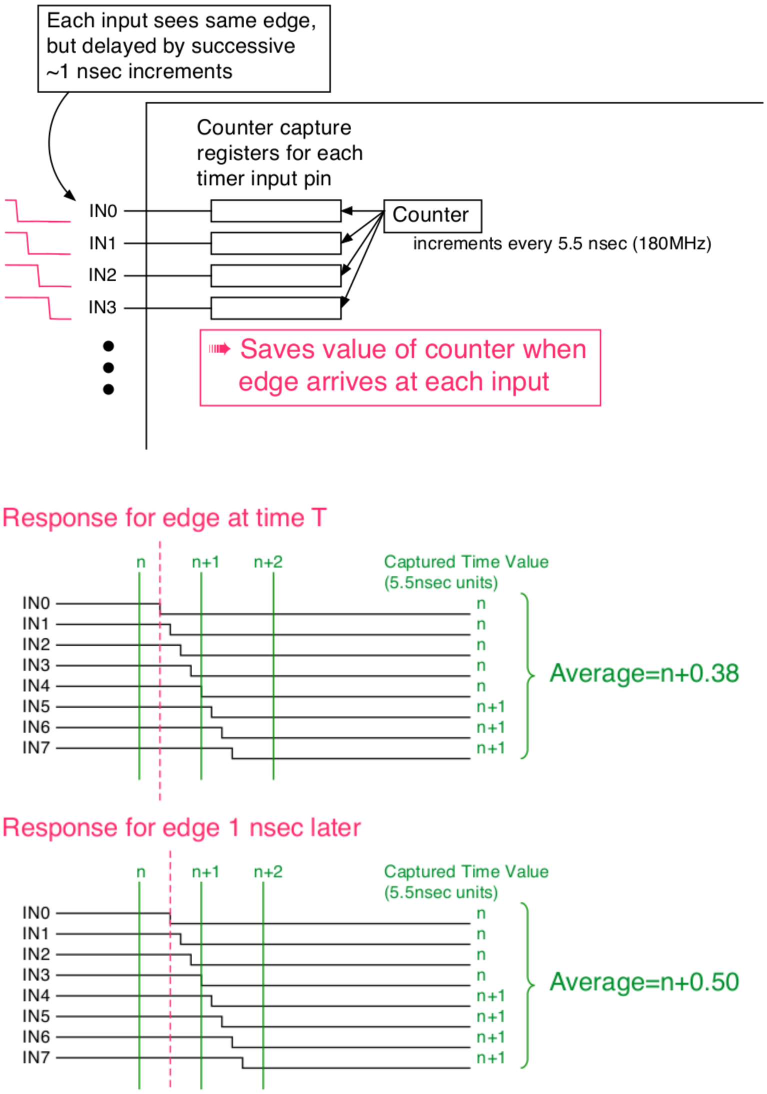

Figure A.1: Achieving ≈ 1 ns accuracy by using the delay lines of MicroDAQ. The discriminator signal is fed into 8 subsequent delays and each time the counter is read out. Then the average of the captured time values is calculated. Possible values are n, $n + 0.13$, $n + 0.25$, $n + 0.38$, $n + 0.50$, $n + 0.63$, $n + 0.75$ and $n + 0.88$, resulting in an improved accuracy of the timing [Wen17].

B Grounding of the SAE prototype

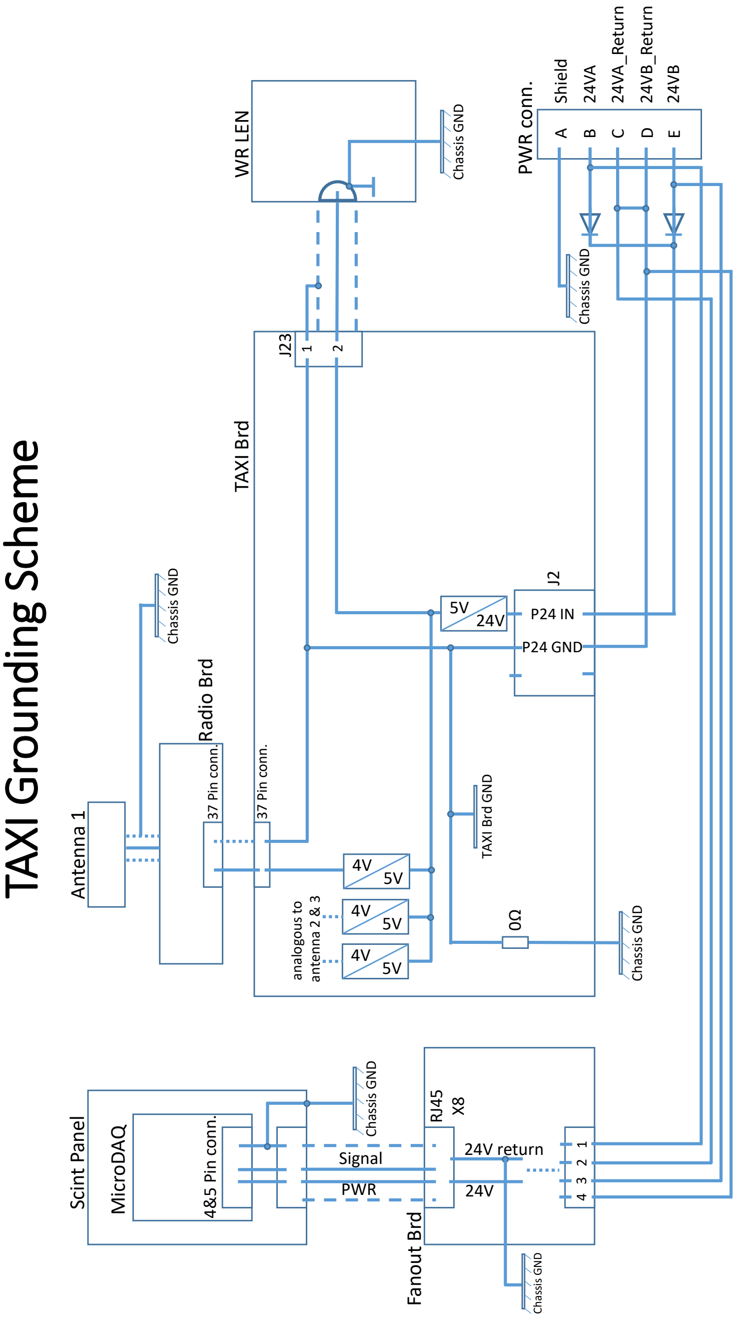

Figure B.1: Sketch of the grounding of the SAE prototype. Modified by Andreas Weindl.

C Direction of the sunlight for peaks in baseline

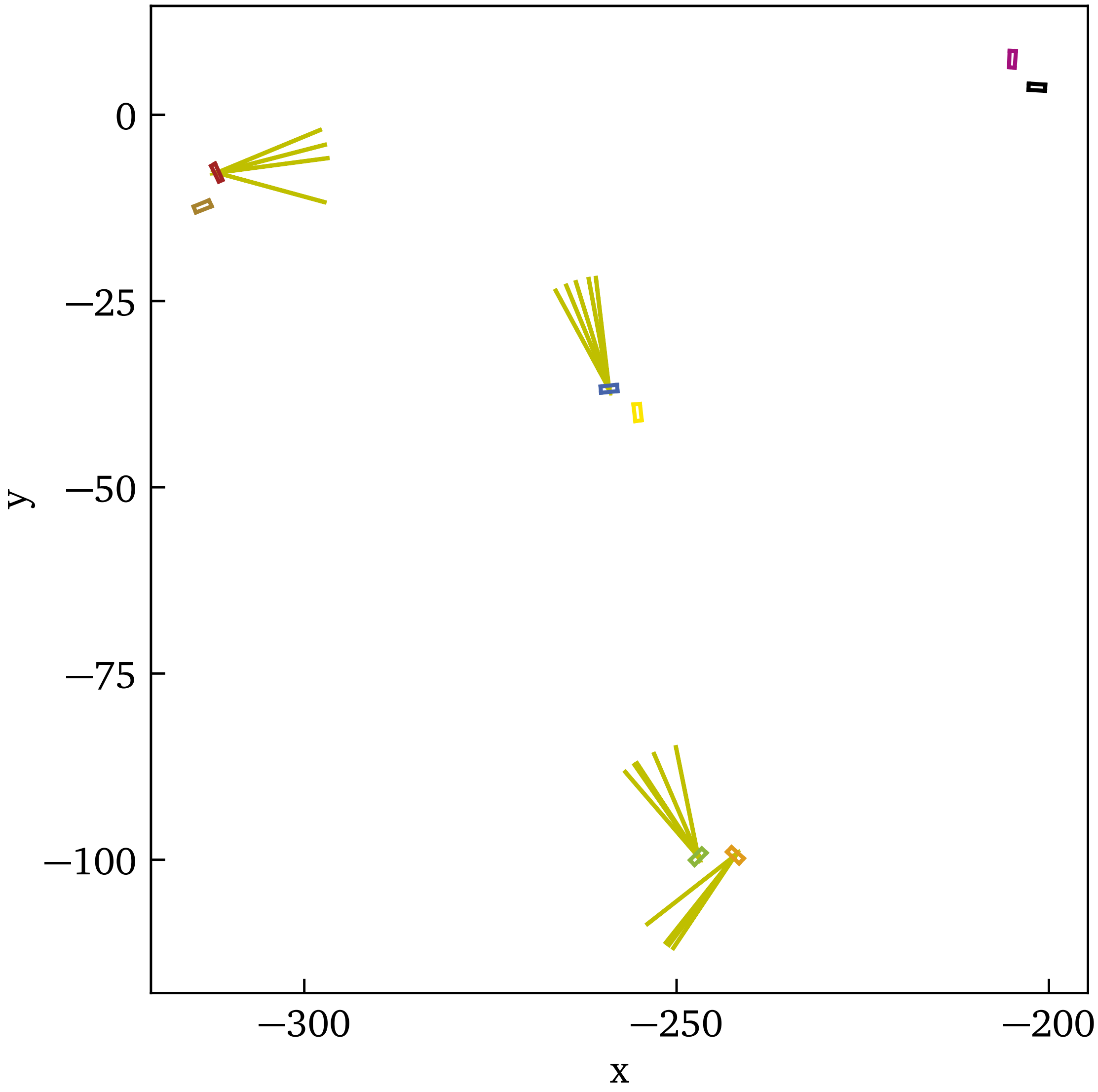

Figure C.1: Direction of the sunlight for peaks in baseline for the entire SAE prototype. Only channels 0, 2, 3 and 6 have peaks distinct enough to do this study. It is visible that the peaks always occur, when the sunlight hits the long detector side opposite to the connector.

D Cable delays of the SAE prototype

Table D.1: Relative cable delays of the scintillation detectors. The method to obtain the cable delays is described in chapter 7.1.5.

channel	cable delay in ns
0	-0.4
1	-4.4
2	0.0
3	-0.9
4	1.9
5	0.1
6	4.1
7	-0.4

E Environmental effects on the single panel hit rate

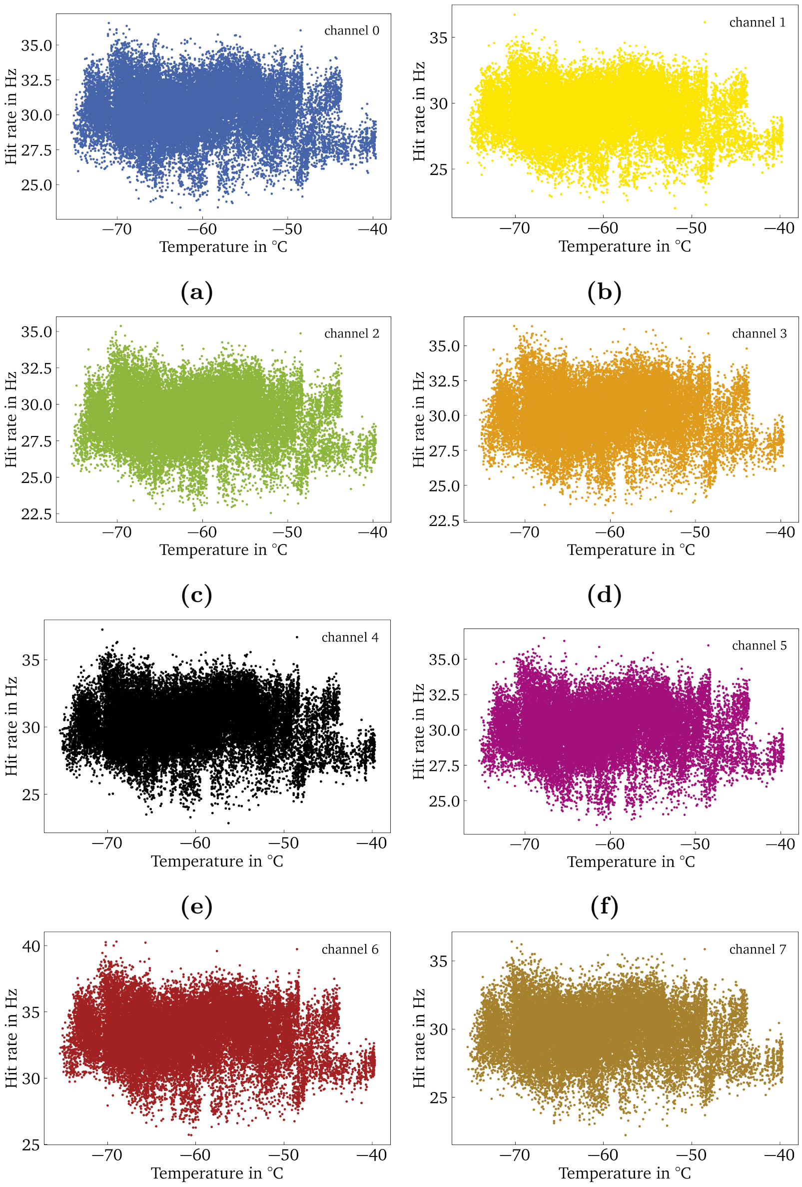

(a) **(b)**

(c) **(d)**

(e) **(f)**

(g) **(h)**

Figure E.1: Single panel hit rate as a function of the temperature. Hits below 4 MIP are excluded in these plots. Due to the calibration, no dependence on the temperature is observed. The same behavior is observed for all channels. Original plots by Martin Pittermann, modified.

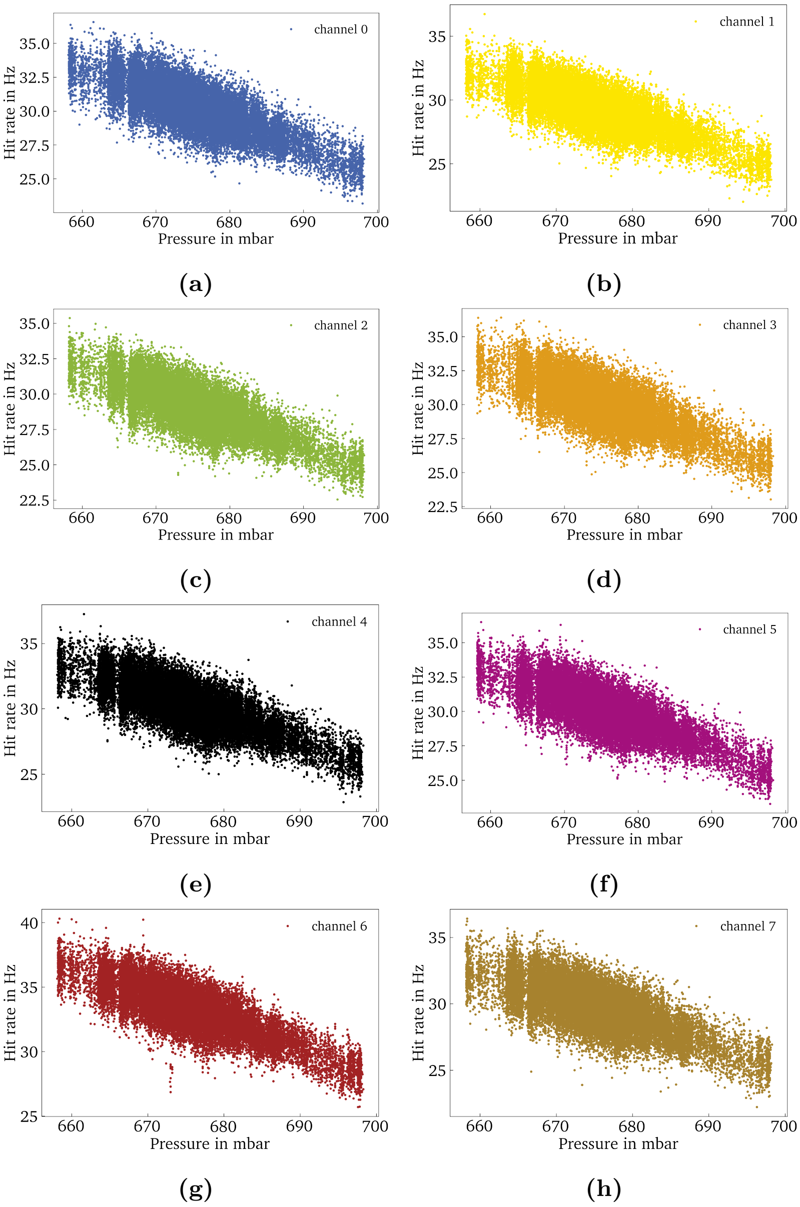

Figure E.2: Single panel hit rate as a function of the pressure. Hits below 4 MIP are excluded in these plots. A decrease of the hit rate with the atmospheric pressure is visible. The same behavior is observed for all channels. Original plots by Martin Pittermann, modified.

F Distribution of the simulated air-showers

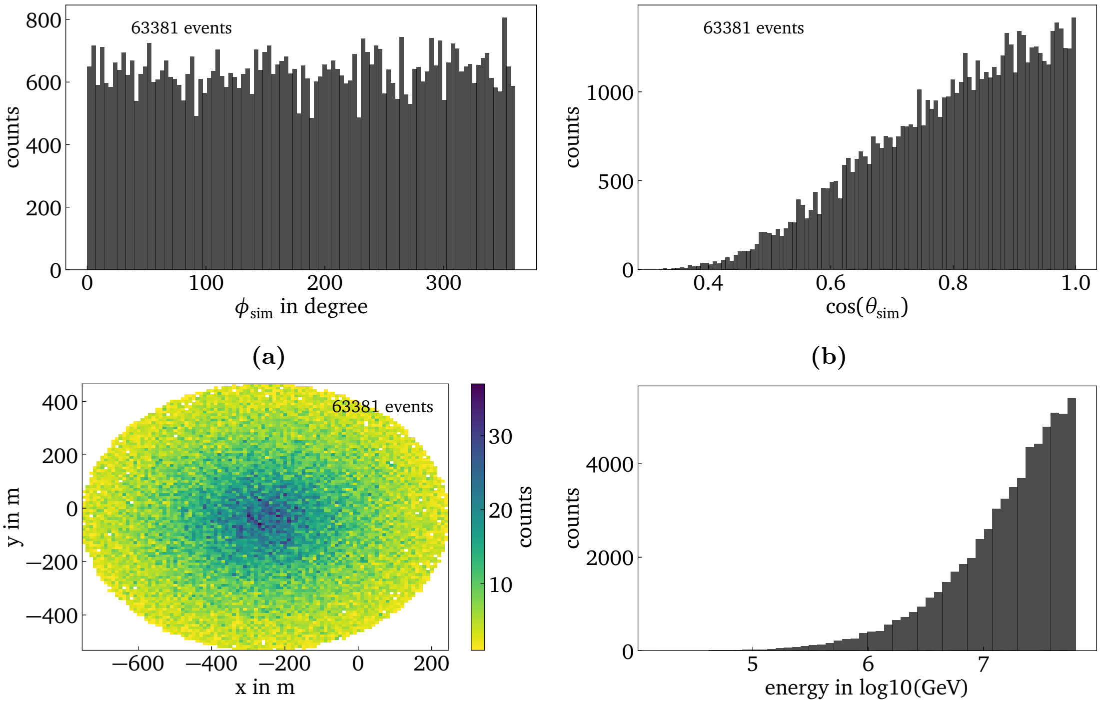

(a) **(b)**

(c) **(d)**

Figure F.1: Distribution of the true azimuth a) and zenith b) angles, the core position c) and the energy d) of the simulations. The distribution of the simulations matches the distribution of the coincident IceTop events.

G Difference between the results of the scintillator reconstruction and Laputop

Table G.1: Difference between the azimuth (ϕ) and zenith (θ) angles, the angluar distance and the core positions reconstructed with the scintillator reconstruction and reconstructed with Laputop for the multiplicities 5-8. The given standard deviations are obtained by fitting a Gaussian. The 68th percentiles ($q_{68\%}$) are obtained from the data without histogramming.

min multiplicity	σ_θ in degree	σ_ϕ in degree	$q_{68\%}$ angular distance in degree	$q_{68\%}$ core distance in meter
5	4.31	8.36	12.13	142.47
6	3.54	6.99	9.64	112.84
7	2.89	5.76	7.47	88.66
8	2.36	4.90	6.01	70.34

H Further photos of the deployment at South Pole

(a) (b) (c) (d) (e) (f) (g) (h)

Figure H.1: Further photos of the deployment at South Pole. Picture credit: Yuya Makino, IceCube/NSF and Marie Oehler, IceCube/NSF.

ACRONYMS

APD	Avalanche Photodiode
API	Application Programming Interface
ARM	ARM MCU (*Stamp9G45*)
AUXDAC	Command for setting the supply voltage of the SiPM, see figure 7.2
cf.	confer
CMB	Cosmic Microwave Background
COBS	Consistent Overhead Byte Stuffing
DAC	Threshold for signal-over-threshold of the MicroDAQ, see figure 7.3
DAQ	Data Acquisition System
DESY	Deutsches Elektronen-Synchrotron
DOM	Digital Optical Module
DRS4	Domino Ring Sampler 4
e. g.	exempli gratia / for example
FIFO	First In, First Out
FFT	Fast Fourier transform
GZK	Greisen-Zatsepin-Kuzmin
HLC	Hard Local Coincidence
I2C	Inter-Integrated Circuit
ICL	IceCube Lab
i. e.	id est / that is
IV-curve	Current-Voltage-Curve
KIT	Karlsruhe Institute of Technology
Laputop	Reconstruction tool for IceTop
LDF	Lateral Distribution Function
LED	Light-Emitting Diode

LNA	Low-Noise Amplifier
LPDA	Log-Periodic Dipole Array
MicroDAQ	Scintillator MicroDAQ v4.1
MIP	Minimum Ionizing Particle
PCB	Printed Circuit Board
PDE	Photon Detection Efficiency
P.E.	Photo Electron Equivalent
$\boldsymbol{\phi}$	Azimuth angle
PMT	Photomultiplier Tube
ppb	Parts Per Billion
PPS	Pulse Per Second
RFI	Radio-Frequency Interference
SAE	Surface Array Enhancement
SerDes	Serializer Deserializer
SiPM	Silicon Photomultiplier
SLC	Soft Local Coincidence
SPOCK	Single Photon Calibration Stand at KIT
TAXI	Transportable Array for eXtremelylarge area Instrumentation studies
$\boldsymbol{\theta}$	Zenith angle
UV	Ultraviolet
WR	White Rabbit
WR-LEN	White Rabbit Lite Embedded Node

List of Figures

Figure 2.1 Energy spectrum of cosmic rays. 4
Figure 2.2 Composition of the all particle flux. 6
Figure 2.3 Schematic of the components of an air shower. 7
Figure 2.4 Schematic of an air shower with its basic parameters for description and reconstruction. 8
Figure 2.5 Air-shower detection techniques. 10
Figure 3.1 The IceCube Neutrino Observatory. 14
Figure 3.2 Shape of neutrino signals in the in-ice detector. 15
Figure 3.3 The surface array IceTop. 16
Figure 3.4 The layout of the Surface Array Enhancement. 18
Figure 3.5 The planned IceCube-Gen2. 20
Figure 4.1 Overview of the DAQ. 22
Figure 4.2 Inside view of the scintillation detectors. 23
Figure 4.3 Outside view of the scintillation detectors. 24
Figure 4.4 The Scintillator MicroDAQ v4.1. 25
Figure 4.5 Layout of MicroDAQ. 26
Figure 4.6 Schematic of the pulses. 27
Figure 4.7 Simplified blockdiagram of the electronics of the SAE prototype. 29
Figure 4.8 The inside of TAXI v3 no. 04 fully assembled. 30
Figure 4.9 The TAXI v3 board. 31
Figure 4.10 The TAXI v3 with fanout board. 32
Figure 4.11 RadioTad. 33
Figure 4.12 Schematic of the TAXI software. 34
Figure 5.1 Example of a charge histogram after refurbishing the detector. 38
Figure 5.2 Map of the SAE prototype. 40
Figure 5.3 Layout of the prototype station. 41
Figure 5.4 Photo of the center of the SAE prototype. 41
Figure 5.5 Deployment of the FieldHub and the central DAQ. 42
Figure 5.6 Deployment of the scintillation detectors. 44
Figure 5.7 Deployment of the radio antennas. 45
Figure 6.1 Fraction of corrupted files per channel from October 22, 2020 until July 12, 2021. 49
Figure 7.1 Calibration of the temperature sensor. 54
Figure 7.2 Mapping of the AUXDAC command to the SiPM supply voltage. 55
Figure 7.3 Mapping of the DAC command to the threshold. 56
Figure 7.4 Hit rate as a function of the threshold. 57

Figure 7.5 Baselines of scintillation detectors from January 6, 2021 until January 10, 2021. 59
Figure 7.6 Comparison of the baselines of channel 2 and 3. 60
Figure 7.7 A hole in the black foil. 61
Figure 7.8 Baselines of the three amplifications. 62
Figure 7.9 Results of the threshold scans. 64
Figure 7.10 Results of the threshold scans for half and zero SiPM supply voltage. 65
Figure 7.11 Baseline of channel 3 during austral winter and spread of the baseline over time. 66
Figure 7.12 Time difference between the hits in neighboring panels. 68
Figure 7.13 Determination of the dead time of MicroDAQ. 70
Figure 7.14 Charge histogram of channel 7. 72
Figure 7.15 Evaluation of the gain. 73
Figure 7.16 Comparison of the gain evaluated from fits to the single p.e. peaks and evaluated from the FFT. 73
Figure 7.17 Gain and MIP dependence on the SiPM supply voltage and the temperature. 75
Figure 7.18 Ratio of the amplifications. 76
Figure 7.19 Difference of the charge in units of MIP between low and medium amplification. 77
Figure 7.20 Histogram of the charge for low amplification. 78
Figure 7.21 Measurement of the electronic gain as a function of frequency. 79
Figure 7.22 Median background spectrum. 79
Figure 8.1 The number of coincident events for eight simultaneously measuring detectors. 82
Figure 8.2 Pressure and temperature of the atmosphere. 83
Figure 8.3 Hit rate of channel 7 as a function of the temperature and pressure. 84
Figure 8.4 Time difference between the reconstructed core time of the scintillation detectors, the reconstructed core time of IceTop and the radio trigger times. 85
Figure 8.5 Time difference between the core times evaluated by Laputop and the scintillator reconstruction. 85
Figure 8.6 Distribution of the azimuth and zenith angles and the energy reconstructed with Laputop. 87
Figure 8.7 Comparison of the multiplicity between simulations and data. 87
Figure 8.8 Distribution of the timestamps and of the charge for simulations and data. 88
Figure 8.9 Average curvature of the air-shower front and LDF for simulations and data. 89
Figure 8.10 Comparison of the charge of neighboring scintillation detectors. 90

Figure 8.11 Fit of the curvature of the air-shower front and LDF fit to single events. 92
Figure 8.12 8 coincidence in scintillator data. 93
Figure 8.13 Difference between the azimuth and zenith angles reconstructed with the scintillator reconstruction and reconstructed with Laputop. 94
Figure 8.14 Distribution of the core position reconstructed with Laputop and with the scintillator reconstruction. 95
Figure 8.15 Example of a triple coincidence event. 96
Figure 8.16 Difference between the zenith and azimuth angles between the three detector types. 96

BIBLIOGRAPHY

[AHH18] M. Ahlers, K. Helbing, and C. P. de los Heros. “Probing particle physics with IceCube.” In: *The European Physical Journal C* 78.11 (2018), pp. 1–51.

[Aab+16] M. Aaboud et al. “Search for new phenomena in final states with an energetic jet and large missing transverse momentum in p p collisions at s= 13 TeV using the ATLAS detector.” In: *Physical Review D* 94.3 (2016), p. 032005.

[Aab+17] A. Aab et al. “Observation of a large-scale anisotropy in the arrival directions of cosmic rays above 8×10^{18} eV.” In: *Science* 357.6357 (2017), pp. 1266–1270. DOI: `10.1126/science.aan4338`.

[Aar+13a] M. G. Aartsen et al. “First observation of PeV-energy neutrinos with IceCube.” In: *Phys. Rev. Lett.* 111 (2013), p. 021103. DOI: `10.1103/PhysRevLett.111.021103`.

[Aar+13b] M. G. Aartsen et al. “Measurement of the cosmic ray energy spectrum with IceTop-73.” In: *Phys. Rev.* D88.4 (2013), p. 042004. DOI: `10.1103/PhysRevD.88.042004`.

[Aar+17a] M. G. Aartsen et al. “IceCube-Gen2: A Vision for the Future of Neutrino Astronomy in Antarctica.” In: *PoS* FRAPWS2016 (2017), p. 004. arXiv: `1412.5106 [astro-ph.HE]`.

[Aar+17b] M. Aartsen et al. “The contribution of FERMI-2LAC blazars to diffuse TeV–PeV neutrino flux.” In: *The Astrophysical Journal* 835.1 (2017), p. 45.

[Aar+17c] M. G. Aartsen et al. “The IceCube Neutrino Observatory: instrumentation and online systems.” In: *Journal of Instrumentation* 12.03 (2017), P03012.

[Aar+18a] M. G. Aartsen et al. “Measurement of Atmospheric Neutrino Oscillations at 6–56 GeV with IceCube DeepCore.” In: *Phys. Rev. Lett.* 120 (7 2018), p. 071801. DOI: `10.1103/PhysRevLett.120.071801`.

[Aar+18b] M. Aartsen et al. “Astrophysical neutrinos and cosmic rays observed by IceCube.” In: *Advances in Space Research* 62.10 (2018), pp. 2902–2930. DOI: `https://doi.org/10.1016/j.asr.2017.05.030`.

[Aar+18c] M. Aartsen et al. “Multimessenger observations of a flaring blazar coincident with high-energy neutrino IceCube-170922A.” In: *Science* 361.6398 (2018). DOI: `10.1126/science.aat1378`.

[Aar+18d] M. Aartsen et al. “Neutrino emission from the direction of the blazar TXS 0506+056 prior to the IceCube-170922A alert.” In: *Science* 361.6398 (2018), pp. 147–151. DOI: `10.1126/science.aat2890`.

[Aar+19] M. G. Aartsen et al. “Cosmic ray spectrum and composition from PeV to EeV using 3 years of data from IceTop and IceCube.” In: *Physical Review D* 100.8 (2019), p. 082002.

[Aar+21] M. Aartsen et al. “IceCube-Gen2: the window to the extreme universe.” In: *Journal of Physics G: Nuclear and Particle Physics* 48.6 (2021), p. 060501.

[Abb+12] R. Abbasi et al. “The design and performance of IceCube DeepCore.” In: *Astroparticle Physics* 35.10 (2012), pp. 615–624. DOI: `https://doi.org/10.1016/j.astropartphys.2012.01.004`.

[Abb+13] R. Abbasi et al. “IceTop: The surface component of IceCube.” In: *Nuclear Instruments and Methods in Physics Research Section A: Accelerators, Spectrometers, Detectors and Associated Equipment* 700 (2013), pp. 188–220. DOI: `https://doi.org/10.1016/j.nima.2012.10.067`.

[Ach+06] A. Achterberg et al. “First year performance of the IceCube neutrino telescope.” In: *Astroparticle Physics* 26.3 (2006), pp. 155 –173. DOI: `https://doi.org/10.1016/j.astropartphys.2006.06.007`.

[Ack+13] M. Ackermann et al. “Detection of the characteristic pion-decay signature in supernova remnants.” In: *Science* 339.6121 (2013), pp. 807–811. DOI: `10.1126/science.1231160`.

[Ahr+01] J. Ahrens et al. “IceCube Preliminary Design Document.” 2001. URL: `http://icecube.wisc.edu/icecube/static/reports/IceCubeDesignDoc.pdf`.

[Ahr+03] J. Ahrens et al. “Icecube - the next generation neutrino telescope at the south pole.” In: *Nucl. Phys. Proc. Suppl.* 118 (2003), pp. 388–395. DOI: `10.1016/S0920-5632(03)01337-9`.

[And33] C. D. Anderson. “The Positive Electron.” In: *Phys. Rev.* 43 (6 1933), pp. 491–494. DOI: `10.1103/PhysRev.43.491`.

[Ant+05] T. Antoni et al. “KASCADE measurements of energy spectra for elemental groups of cosmic rays: Results and open problems.” In: *Astroparticle Physics* 24.1 (2005), pp. 1–25. DOI: `https://doi.org/10.1016/j.astropartphys.2005.04.001`.

[Ask62] G. Askaryan. “Excess negative charge of an electron–photon shower and its coherent radio emission.” In: *Sov. Phys. JETP* 14 (1962), p. 441.

[Ave+07] M. Ave et al. “The accuracy of signal measurement with the water Cherenkov detectors of the Pierre Auger Observatory.” In: *Nuclear Instruments and Methods in Physics Research Section A: Accelerators, Spectrometers, Detectors and Associated Equipment* 578.1 (2007), pp. 180–184. DOI: `https://doi.org/10.1016/j.nima.2007.05.150`.

[BEH09] J. Blümer, R. Engel, and J. R. Hörandel. “Cosmic rays from the knee to the highest energies.” In: *Progress in Particle and Nuclear Physics* 63.2 (2009), pp. 293–338.

[BGG06] V. Berezinsky, A. Gazizov, and S. Grigorieva. “On astrophysical solution to ultrahigh energy cosmic rays.” In: *Physical Review D* 74.4 (2006), p. 043005.

[Bal19] A. Balagopal V. “A Quest for PeVatrons Employing Radio Detection of Extensive Air Showers.” PhD thesis. Karlsruhe Institute for Technology (KIT), 2019. 129 pp. DOI: `10.5445/IR/1000091377`.

[Ben21] T. Bendfelt. “Surface Station DAQ Software.” In: *IceCube Collaboration Meeting.* 2021.

[Bez+04] D. Beznosko et al. “FNAL-NICADD extruded scintillator.” In: *IEEE Symposium Conference Record Nuclear Science 2004.* Vol. 2. 2004, 790–793 Vol. 2. DOI: `10.1109/NSSMIC.2004.1462328`.

[Bre+17] T. Bretz et al. “SiPMs A revolution for high dynamic range applications.” In: *PoS* ICRC2017 (2017), p. 472. DOI: `10.22323/1.301.0472`.

[CB99] S. Cheshire and M. Baker. “Consistent overhead byte stuffing.” In: *IEEE/ACM Transactions on Networking* 7.2 (1999), pp. 159–172. DOI: `10.1109/90.769765`.

[CS66] C. Crowell and S. Sze. “Temperature dependence of avalanche multiplication in semiconductors.” In: *Applied Physics Letters* 9.6 (1966), pp. 242–244.

[Col+11] G. Collazuol et al. “Studies of silicon photomultipliers at cryogenic temperatures.” In: *Nuclear Instruments and Methods in Physics Research Section A: Accelerators, Spectrometers, Detectors and Associated Equipment* 628.1 (2011), pp. 389–392. DOI: `https://doi.org/10.1016/j.nima.2010.07.008`.

[Cor20] N. D. Corporation. “Product Data Sheet P-212 WHT Glass Cloth Tape.” `https://www.nitto.com/eu/en/others/products/file/datasheet/PDS_NA_Glass_Cloth_Tape_P-212WHT_012020_EN.pdf`. 2020.

[Dem+17] H. Dembinski et al. “Data-driven model of the cosmic-ray flux and mass composition from 10 GeV to $10^1$1 GeV.” In: *PoS* ICRC2017 (2017), p. 533. DOI: `10.22323/1.301.0533`.

[Des06] P. Desiati. “IceCube: Toward a km3 Neutrino Telescope.” In: *proceeding of ECRS 2006* (2006). URL: `arXiv:astro-ph/0611603`.

[EHP11] R. Engel, D. Heck, and T. Pierog. “Extensive air showers and hadronic interactions at high energy.” In: *Annual review of nuclear and particle science* 61 (2011), pp. 467–489. DOI: `10.1146/annurev.nucl.012809.104544`.

[Fle82] J. Fletcher. “An Arithmetic Checksum for Serial Transmissions.” In: *IEEE Transactions on Communications* 30.1 (1982), pp. 247–252. DOI: `10.1109/TCOM.1982.1095369`.

[GER16] T. K. Gaisser, R. Engel, and E. Resconi. “Cosmic rays and particle physics.” Second edition. Cambridge: Cambridge University Press, 2016.

[Gai12] T. K. Gaisser. “Spectrum of cosmic-ray nucleons, kaon production, and the atmospheric muon charge ratio.” In: *Astroparticle Physics* 35.12 (2012), pp. 801–806. DOI: `https://doi.org/10.1016/j.astropartphys.2012.02.010`.

[Gar20] E. Garutti. “Silicon Photomultipliers.” In: *Handbook of Particle Detection and Imaging*. Ed. by I. Fleck et al. Cham: Springer International Publishing, 2020, pp. 1–21. DOI: `10.1007/978-3-319-47999-6_48-1`.

[Gri10] P. K. Grieder. “Extensive air showers.” 2. ed. Berlin: Springer, 2010.

[Gru20] C. Grupen. “Astroparticle physics.” Second edition. Berlin, Heidelberg: Springer Nature Switzerland, 2020.

[HK10] F. Halzen and S. R. Klein. “IceCube: An Instrument for Neutrino Astronomy.” In: *Rev. Sci. Instrum.* 81 (2010), p. 081101. DOI: `10.1063/1.3480478`.

[HPDG16] Hamamatsu Photonics Deutschland GmbH. “MPPC S13360 series.” `https://www.hamamatsu.com/resources/pdf/ssd/s13360_series_kapd1052e.pdf`. 2016.

[HSH19] E. M. Holt, F. G. Schröder, and A. Haungs. “Enhancing the cosmic-ray mass sensitivity of air-shower arrays by combining radio and muon detectors.” In: *The European Physical Journal C* 79.5 (2019), pp. 1–12.

[Hau15] A. Haungs. “Cosmic Rays from the Knee to the Ankle.” In: *Physics Procedia* 61 (2015), pp. 425–434.

[Hau+19] A. Haungs et al. “A Scintillator and Radio Enhancement of the IceCube Surface Detector Array.” In: *EPJ Web of Conferences*. Vol. 210. EDP Sciences. 2019, p. 06009.

[Hec+98] D. Heck et al. *CORSIKA: A Monte Carlo code to simulate extensive air showers.* Tech. rep. 1998. DOI: `10.5445/IR/270043064`.

[Hei44] W. Heitler. “Quantum Theory of Radiation.” 2. ed. Oxford University Press, 1944.

[Hil84] A. M. Hillas. “The origin of ultra-high-energy cosmic rays.” In: *Annual review of astronomy and astrophysics* 22 (1984), pp. 425–444.

[Hub+17] T. Huber et al. “The IceTop Scintillator Upgrade.” In: *PoS* ICRC2017 (2017), p. 401. DOI: `10.22323/1.301.0401`.

[Hub21] T. Huber. “IceScint: A Scintillation Detector Array for the IceCube Surface Enhancement.” Dissertation. Karlsruhe Institute of Technology, 2021. URL: `https://doi.org/10.5445/IR/1000131545`.

[IC21] IceCube Collaboration and A. Coleman. “Simulation Study of the Observed Radio Emission of Air Showers by the IceTop Surface Extension.” In: ICRC 2021. Vol. 317. Proceedings of Science. 2021.

[IR19] IceCube Collaboration and M. Renschler. “First measurements with prototype radio antennas for the IceTop detector array.” In: ICRC 2019. Vol. 401. Proceedings of Science. 2019.

[IS21] IceCube Collaboration and K.-H. Sulanke. “Design and performance of the multi-PMT optical module for IceCube Upgrade.” In: ICRC 2021. Vol. 1070. Proceedings of Science. 2021.

[Ice13] IceCube Collaboration. “Evidence for high-energy extraterrestrial neutrinos at the IceCube detector.” In: *Science* 342.6161 (2013), p. 1242856.

[Ice16] IceCube Collaboration. “Cosmic ray spectrum and composition from three years of IceTop and IceCube.” In: *Journal of Physics: Conference Series*. Vol. 718. 5. IOP Publishing. 2016, p. 052033.

[Ice19a] IceCube Collaboration. “Simulation and Reconstruction Study of a Future Surface Scintillator Array at the IceCube Neutrino Observatory.” In: *PoS* ICRC2019 (2019), p. 332. DOI: `10.22323/1.358.0332`.

[Ice19b] IceCube Collaboration. “The IceCube upgrade - Design and science goals.” In: *PoS (ICRC2019)* 1031 (2019).

[Ice19c] IceCube Collaboration. “The Scintillator Upgrade of IceTop: Performance of the prototype array.” In: ICRC 2019. Vol. 309. Proceedings of Science. 2019.

[Ice21a] IceCube Collaboration. “Deployment of the IceCube Upgrade Camera System in the SPICEcore hole.” In: ICRC 2021. Vol. 1047. Proceedings of Science. 2021.

[Ice21b] IceCube Collaboration. "Detection of a particle shower at the Glashow resonance with IceCube." In: *Nature* 591.7849 (2021), pp. 220–224.

[Ice21c] IceCube Collaboration. "Development of a scintillation and radio hybrid detector array at the South Pole." In: ICRC 2021. Vol. 225. Proceedings of Science. 2021.

[Ice21d] IceCube Collaboration. "First air-shower measurements with the prototype station of the IceCube surface enhancement." In: ICRC 2021. Vol. 314. Proceedings of Science. 2021.

[Ice21e] IceCube Collaboration. "Performance of the D-Egg Optical Sensor for the IceCube Upgrade." In: ICRC 2021. Vol. 1042. Proceedings of Science. 2021.

[Ice21f] IceCube Collaboration. "The Acoustic Module for the IceCube Upgrade." In: ICRC 2021. Vol. 1059. Proceedings of Science. 2021.

[JPW13] P. P. M. Jansweijer, H. Z. Peek, and E. de Wolf. "White Rabbit: Sub-nanosecond timing over Ethernet." In: *Nuclear Instruments and Methods in Physics Research Section A: Accelerators, Spectrometers, Detectors and Associated Equipment* 725 (2013), pp. 187–190. DOI: `10.1016/j.nima.2012.12.096`.

[KC] L. Kuraray Co. "Plastic Scintillating Fibers." `http://kuraraypsf.jp/pdf/all.pdf`. Accessed: 2021-06-26.

[KL66] F. D. Kahn and I Lerche. "Radiation from cosmic ray air showers." In: *Proceedings of the Royal Society of London. Series A. Mathematical and Physical Sciences* 289.1417 (1966), pp. 206–213.

[KU12] K.-H. Kampert and M. Unger. "Measurements of the cosmic ray composition with air shower experiments." In: *Astroparticle Physics* 35.10 (2012), pp. 660–678.

[KW12] K.-H. Kampert and A. A. Watson. "Extensive air showers and ultra high-energy cosmic rays: a historical review." In: *The European Physical Journal H* 37.3 (2012), pp. 359–412.

[Kar+14] T. Karg et al. "Introducing TAXI: a Transportable Array for eXtremely large area Instrumentation studies." 2014. arXiv: `1410.4685`.

[Kis12] F. Kislat. "Measurement of the energy spectrum of cosmic rays with the 26 station configuration of the IceTop detector." Dissertation. Humboldt-Universität zu Berlin, Mathematisch-Naturwissenschaftliche Fakultät I, 2012. DOI: `http://dx.doi.org/10.18452/16443`.

[Kno00] G. F. Knoll. "Radiation detection and measurement." 3. ed. New York, NY: Wiley, 2000.

[Kow15] M. Kowalski. "Status of high-energy neutrino astronomy." In: *Journal of Physics: Conference Series*. Vol. 632. 1. IOP Publishing. 2015, p. 012039.

[LA+15a] E. de Lera Acedo et al. "Evolution of SKALA (SKALA-2), the log-periodic array antenna for the SKA-low instrument." In: *2015 International Conference on Electromagnetics in Advanced Applications (ICEAA)*. 2015, pp. 839–843. DOI: `10.1109/ICEAA.2015.7297231`.

[LA+15b] E de Lera Acedo et al. "SKALA, a log-periodic array antenna for the SKA-low instrument: design, simulations, tests and system considerations." In: *Experimental Astronomy* 39.3 (2015), pp. 567–594.

[LAFV16] E. de Lera Acedo, A. Faulkner, and J. Bij de Vaate. "SKA low frequency aperture array." In: *2016 United States National Committee of URSI National Radio Science Meeting (USNC-URSI NRSM)*. 2016, pp. 1–2. DOI: `10.1109/USNC-URSI-NRSM.2016.7436228`.

[Les19] A. Leszczyńska. "Simulation study for the IceCube IceTop enhancement with a scintillator array." In: *Journal of Physics: Conference Series* 1181 (2019), p. 012076. DOI: `10.1088/1742-6596/1181/1/012076`.

[Les21] A. S. Leszczyńska. "Potential of the IceTop Enhancement with a Scintillation Detector Array." Dissertation. Karlsruhe Institute of Technology, 2021. DOI: `10.5445/IR/1000131245`.

[Lip14] P. Lipari. "Cosmic rays and hadronic interactions." In: *Comptes Rendus Physique* 15.4 (2014), pp. 357–366. DOI: `https://doi.org/10.1016/j.crhy.2014.02.012`.

[Mat05] J. Matthews. "A Heitler model of extensive air showers." In: *Astroparticle Physics* 22.5 (2005), pp. 387–397. DOI: `https://doi.org/10.1016/j.astropartphys.2004.09.003`.

[NON] National Oceanic and A. A. G. M. L. (NOAA/OAR/GML). "Data measured by the station South Pole, Antarctica." `https://gml.noaa.gov/aftp/data/radiation/baseline/spo/2021/`. Accessed on 2021-09-01.

[Nuh21] Ö. Nuhoğlu. "Characterisation of the Data Acquisition System of the IceCube Surface Detector Enhancement." BA thesis. Karlsruhe Institute of Technology, 2021.

[Oeh18] M. Oehler. "Characterization of SiPMs for the Surface Array Enhancement of IceCube." MA thesis. Karlsruhe Institute of Technology, 2018.

[Ott+17] A. N. Otte et al. "Characterization of three high efficiency and blue sensitive silicon photomultipliers." In: *Nuclear Instruments and Methods in Physics Research Section A: Accelerators, Spectrometers, Detectors and Associated Equipment* 846 (2017), pp. 106–125. DOI: `https://doi.org/10.1016/j.nima.2016.09.053`.

[PDBR03] A. Pla-Dalmau, A. Bross, and V. Rykalin. "Extruding plastic scintillator at Fermilab." In: *2003 IEEE Nuclear Science Symposium. Conference Record (IEEE Cat. No.03CH37515)*. Vol. 1. 2003, 102–104 Vol.1. DOI: `10.1109/NSSMIC.2003.1352007`.

[Par+20] Particle Data Group et al. "Review of particle physics." In: *Progress of Theoretical and Experimental Physics* 2020.8 (2020), pp. 1–2093.

[Pau16] Paul Scherrer Institute. "DRS4 datasheet rev. 0.9." `https://www.psi.ch/sites/default/files/2020-08/DRS4_rev09_2.pdf`. 2016.

[Pet61] B Peters. "Primary cosmic radiation and extensive air showers." In: *Il Nuovo Cimento (1955-1965)* 22.4 (1961), pp. 800–819. DOI: `10.1007/BF02783106`.

[Rad] RadioReference.com LLC. "Antarctica." `https://wiki.radioreference.com/index.php/Antarctica`. Accessed: 2021-06-23.

[Raw16] K. Rawlins. "A Function to Describe Attenuation of Cosmic Ray Air Shower Particles in Snow." In: *PoS* ICRC2015 (2016), p. 628. DOI: `10.22323/1.236.0628`.

[Ren20] M. Renschler. “A prototype radio detector for the IceCube surface enhancement.” Dissertation. Karlsruhe Institute of Technology, 2020. URL: `http://dx.doi.org/10.5445/IR/1000104529`.

[SS37] J. C. Street and E. C. Stevenson. “New Evidence for the Existence of a Particle of Mass Intermediate Between the Proton and Electron.” In: *Phys. Rev.* 52 (9 1937), pp. 1003–1004. DOI: `10.1103/PhysRev.52.1003`.

[SSB18] M. Spurio, Spurio, and Bellantone. “Probes of Multimessenger Astrophysics.” Springer, 2018.

[San18] J. van Santen. “IceCube-Gen2: the next-generation neutrino observatory for the South Pole.” In: *PoS* ICRC2017 (2018), p. 991. DOI: `10.22323/1.301.0991`.

[Sch17] F. G. Schröder. “Radio detection of cosmic-ray air showers and high-energy neutrinos.” In: *Progress in Particle and Nuclear Physics* 93 (2017), pp. 1–68. DOI: `https://doi.org/10.1016/j.ppnp.2016.12.002`.

[Sch19a] F. G. Schröder. “News from cosmic ray air showers (Cosmic ray indirect - CRI Rapporteur).” In: *PoS* ICRC2019 (2019), p. 030. DOI: `10.22323/1.358.0030`.

[Sch19b] F. G. Schröder. “Science Case of a Scintillator and Radio Surface Array at IceCube.” In: *PoS* ICRC2019 (2019), p. 418. DOI: `10.22323/1.358.0418`.

[Spa19] R. Sparvoli. “Cosmic Ray Direct Observations.” In: *PoS* ICRC2019 (2019), p. 032. URL: `https://www.icrc2019.org/uploads/1/1/9/0/119067782/sparvoli_rapporteur_crd.pdf`.

[TIA98] *Electrical Characteristics of Generators and Receivers for Use in Balanced Digital Multipoint Systems.* Standard TIA/EIA-485-A-98. Telecommunications Industry Association, 1998.

[TP19] D. Tosi and H. Pandya. “IceTop as veto for IceCube: results.” In: *PoS* ICRC2019 (2019), p. 445. DOI: `10.22323/1.358.0445`.

[Tex13] Texas Instruments Incorporated. “LM94021/LM94021Q Multi-Gain Analog Temperature Sensor.” `https://www.ti.com/lit/ds/symlink/lm94021.pdf`. 2013.

[Tho+16] S. Thoudam et al. “Cosmic-ray energy spectrum and composition up to the ankle: the case for a second Galactic component.” In: *Astronomy & Astrophysics* 595 (2016), A33. DOI: `10.1051/0004-6361/201628894`.

[Til20] S. Tilav. “2020-Scintillator Array first triggers coincident with IceTop.” In: *Scintillator Call 2020-07-09.* 2020.

[Uni] United States Antarctic Program. “Attachment A, Comms Forms.” `https://www.nsf.gov/geo/opp/antarct/treaty/pdf/plans0708/attacha_08.pdf`. Accessed: 2021-06-23.

[Wen] C. Wendt. “Private communication.” URL: `chwendt@icecube.wisc.edu`.

[Wen17] C. Wendt. “MicroDAQ System for IceTop Scintillators.” In: *Scintillator Workshop 2017-04-29.* 2017.

[XIL11] XILINX Co Ltd. “Spartan-6 Family Overview.” `https://www.xilinx.com/support/documentation/data_sheets/ds160.pdf`. 2011.

[tas11] taskit GmbH. “Stamp9G45 Technical Reference.” `https://www.taskit.de/media/pdf/eb/49/03/premium_starterkit_stamp9g45_128f128r_technical_reference_4260578791205.pdf`. 2011.

Acknowledgements

Thank you, ...

... Prof. Dr. Ralph Engel for giving me the great chance to do my thesis in the very interesting field of astroparticle physics, for discussing the current status on a regular basis and for your hints on solutions for open questions.

... Prof. Dr. Marc Weber for the support and the "go" for the production of the electronics.

... Dr. Andreas Haungs, for your guidance, never-ending optimism and the many possibilities to participate in conferences and meetings all around the world.

... KSETA, for the financial support of my research, the topical courses to deepen and expand my knowledge and providing multiple opportunities to interact with other fellows.

... Sabine and Anna, for helping me with every administrative problem I ever had at IAP and making the many appointments.

... Hrvoje, for the joint TAXI testing, the selected radio events and the productive discussions of the many plots.

... Agnieszka, for all the simulations, your help with the scintillator reconstruction and our jovial chats.

... Andreas W., for all the TAXI software and for making me aware of the benefits of instant soups and using exercise balls instead of chairs.

... Bernd, for solving practically every technical problem, the ton of soldering work you did and your friendly explanations.

... Tom, for your pragmatism in overcoming challenges, the funny pictures and for your never-ending source of humor.

... Max, for your friendly explanations on radio issues and handing down the design of the previous prototype.

... Aswathi, Shefali, Fiona, and Sally, for the warm and friendly atmosphere in our office as well as sharing our experiences and sweets.

... Frank, for hand-carrying the other TAXI and the time at the Pole.

... Doris, for your patient computer-related support.

... Ömer, Daniel and Abdul, who gave me the chance to improve my supervising skills.

... Markus Imm, for your support with the FPGA firmware, especially before going to Madison for rebuilding the detectors and around the time going to Pole.

... Roxanne, for the fruitful scint-radio cooperation.

... Martin for the single-panel hit-rate plots, which you programmed in record time.

... Karl-Heinz Sulanke, Timo Karg and Marko Kossatz for your TAXI-expertise.

... Alexander Menshikov for modifying the TAXI board.

... Uwe Baur and Alexander Bacher, for populating all the boards.

... Frederico, Paras and Noah, for your cordial company while I make the 100th cup of tea.
... Michael, for the time at PSL refurbishing the detectors.
... Harald, for your meticulous planning of the trip to the meeting in Japan.
... the lunch-group Katrin, Donghwa, Vova, Ewa, David, Fabio, Tim, Julian and Frank for the enjoyable diversion and company.
... Anja, Heike and Will, for all the cheerful conversations in the lab and at WAB.
... the whole IAP/ETP staff for the warm and friendly welcome and the on- and off-topic discussions.
... Matt, for the great time at Pole and all fast answers to my questions.
... Chris, for your patient and detailed explanations about MicroDAQ and for designing the boards.
... Tim, for your help in all MicroDAQ software things.
... John K., for your advice with the WR-LEN.
... Delia, for your questions, which helped improving the system.
... Yuya and John H., for the enjoyable time at Pole and all the inspiration you gave me.
... everyone, who helped with the outstanding trip to the South Pole.
... the members of IceCube@KIT group, scint group, cosmic ray group and IceCube collaboration for the fruitful discussions and scientific aspiration.
... to all the hardworking helpers behind the scenes, who are not mentioned by name.
... Ina, Kristina, Lilly, Eva, Henni and Jara, for the lively and relaxing conversations that brought a breath of fresh air.
... my parents and my brother, for the loving encouragement and the great support in all situations in my life.
... Manuel, for always being there, making me smile and the many hot chocolates, cookies and cups of tea.